DYNAMIC FRICTIONAL SLIDING ALONG AN INTERFACE BETWEEN TWO HOMOGENEOUS BLOCKS

By

ERIKA ENNIS NICHOLS

Bachelor of Science in Mechanical Engineering

Oklahoma State University

Stillwater, Oklahoma

2006

Submitted to the Faculty of the
Graduate College of the
Oklahoma State University
in partial fulfillment of
the requirements for
the Degree of
MASTER OF SCIENCE
May, 2008

DYNAMIC FRICTIONAL SLIDING ALONG AN INTERFACE BETWEEN TWO HOMOGENEOUS BLOCKS

Thesis Approved:

Dr. D. Coker
Thesis Adviser

Dr. H. Lu

Dr. J.K. Good

Dr. A.Gordon Emslie
Dean of the Graduate College

ACKNOWLEDGEMENTS

I would like to express my appreciation to my advisor, Dr. Coker. Without his assistance, I would not have been able to complete this research. I would also like to extend my gratitude and appreciation toward the other members of my thesis committee, Dr. Lu and Dr. Good, whose suggestions, wisdom, and guidance were invaluable throughout this study. I would also like to extend a special thanks to Dr. Arena who was always willing to help and encourage me throughout this process.

I would like to thank the Department of Mechanical and Aerospace Engineering for their support and encouragement. I would also like to thank Charles O'Neill for diagnosing and fixing my computer that stopped working but still had all of my research data on it. Also, I would like to thank Nic Moffitt for always being there to help and talk about any problems that I was having with my research. And I would like to give special thanks to Nathan Lunsford and Michael Bolitho for always being available to help or discuss anything at any time.

I would like to thank my parents, Steve and Kathy Ennis, for instilling in me the values and strength that were necessary for me to complete my thesis work. I would also like to thank my husband, Rodney, for his support, encouragement, and understanding throughout these last two years. Also, thank you to all of my family and friends who were always there to support and encourage me along the way. Finally, I would like to thank my Lord and Savior Jesus Christ. Without Him, I would not be the person that I am today.

TABLE OF CONTENTS

Chapter Page

LIST OF TABLES

Table Page

LIST OF FIGURES

Figure Page

Figure Page

Figure Page

CHAPTER 1

INTRODUCTION

1.1. Background

Friction is an essential part of each and every day. Imagine a world without friction…a man would not be able to simply walk down the road because without friction, he would fall! With the importance of friction it is amazing how little is actually known about it. In undergraduate physics, Coulomb's law of friction is taught as $F=\mu N$, where F is the frictional force, μ is the coefficient of friction, and N is the normal force. However, this equation leaves out some very important details.

It is already known that when the speed of an object increases, its coefficient of friction decreases. However, rock experiments conducted by geophysicists showed that when an object's speed is suddenly increased, the coefficient of friction first increases and then exponentially decreases until it reaches its limiting value. This exponential decrease is referred to as the transient effect. Coulomb's Law has a different coefficient of friction for static and dynamic friction. It does not explain transition, effect of hold time, and how it changes with speed as demonstrated in the experimental data from Marone (1998) shown in Figure 1.1.

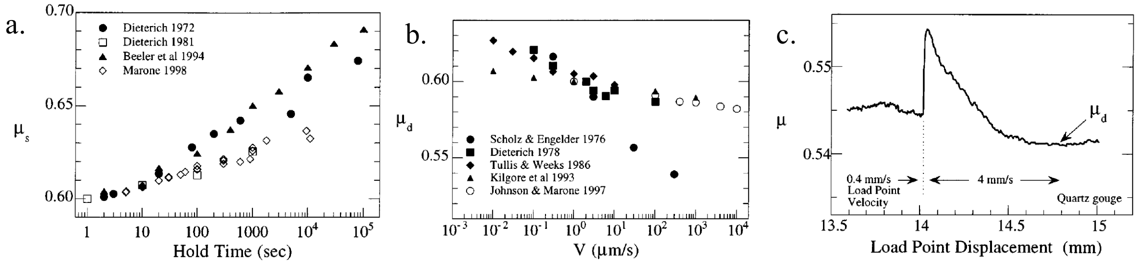

Figure 1.1: Coefficient of Friction Experimental Results (Marone 1998) (a) effect of hold time on μ_s, (b) effect of sliding velocity on μ_d, (c) transient effect on μ_d due to a instantaneous change in sliding velocity

Figure 1.1a shows the effect of the static coefficient of friction over time. Coulomb's Law indicates that the static coefficient should be constant over time but experimental results have shown that instead of remaining constant over time, the static coefficient of friction actually increases logarithmically with time. Figure 1.1b shows the dynamic coefficient of friction plotted against sliding velocity. As the velocity increases, the dynamic coefficient of friction actually decreases over time. This is not what we would expect from Coulomb's Law which leaves the dynamic coefficient of friction constant as velocity increases. The third area where Coulomb's Law does not accurately explain experimental results is the effect of the coefficient of friction with a change in the velocity during sliding. Figure 1.1c shows that for a velocity of 0.4 mm/s the coefficient of friction remains fairly constant around 0.545, but when the velocity is suddenly increased to 4 m/s the coefficient of friction decreases over time and distance. The interesting note here is that when the velocity is increased suddenly, there is an instantaneous jump in the coefficient of friction to a higher coefficient of friction before it logarithmically returns to a lower value than the 0.545 that was seen initially.

Thus, it was found that a frictional law should not hold the coefficient of friction constant but instead the frictional coefficient is better modeled as a function of sliding speed and its history. The law that accounts for these occurrences is referred to as the rate-state constitutive friction law and an example can be seen in Figure 1.2 below.

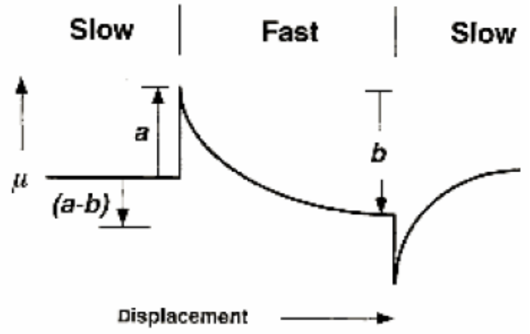

Figure 1.2: Variation of μ due to an instantaneous change in sliding velocity in the rate-state friction law

Coulomb's Law does not accurately describe stick-slip sliding. This stick slip phenomenon can be witnessed in many different situations. While driving home in the rain, one could witness a windshield wiper on a car sticking and then skipping on the glass. Instead of easily sliding across the windshield, it would probably leave layers of water on the glass. This stick-slip is also found on different length scales that might include the squeaking of machinery or the unstable fault slips in the Earth. Earthquakes are stick-slip events on a large length scale measured in kilometers and a large time scale measured in years. Over many years the tectonic plates of the earth along a fault are sticking to one another and building up stress. But as discussed from Figure 1.1a, the static coefficient of friction that keeps these tectonic plates from sliding is gradually increasing which allows for a slip event to trigger an earthquake over many kilometers of the fault line. Figure 1.3 shows the San Andreas Fault as an example of this frictional sliding along an interface (the fault line).

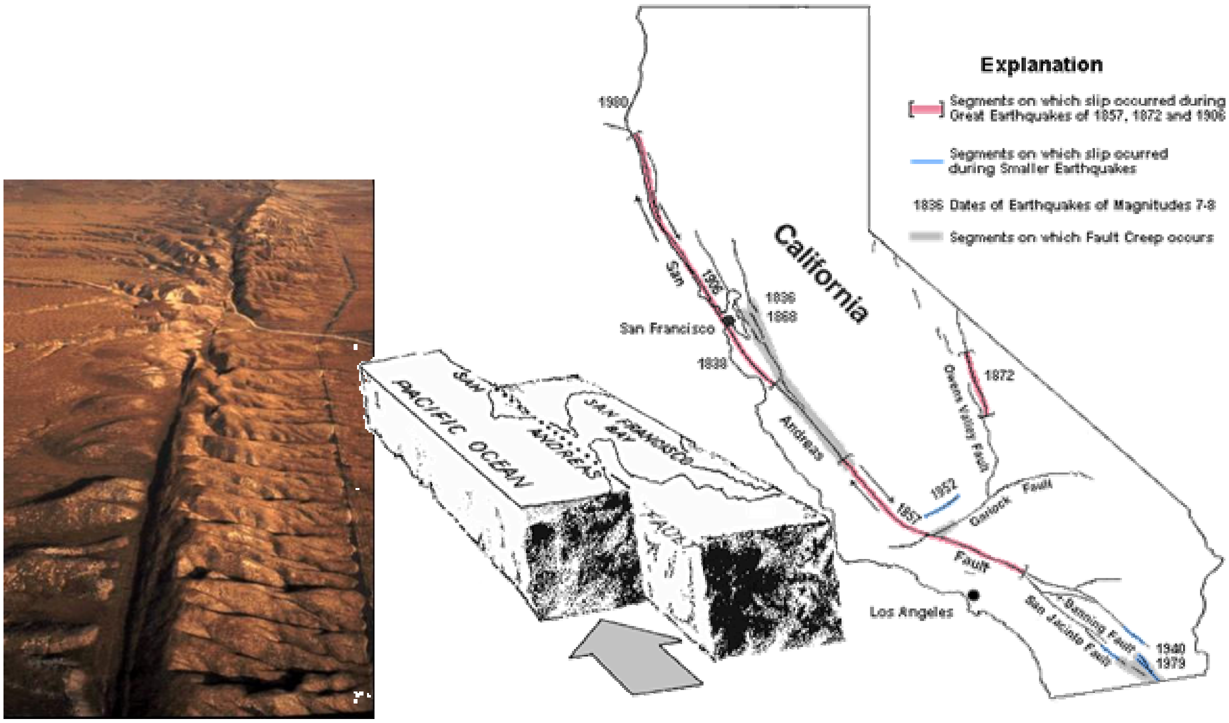

Figure 1.3: San Andreas Fault – earthquakes as an example of frictional sliding

The two blocks shown in the middle of Figure 1.3 are each of similar earth materials and are sliding relative to one another. In fact, this is the driving force behind this research. Instead of simulating two blocks made of rock, this research will look at two Homalite blocks that are sliding relative to one another. Homalite was chosen as the material to model due to its similarities with rock including their brittleness and elastic properties. Homalite's ability to show isochromatic fringes in laboratory experiments that qualitatively showed important correlation to numerical simulation results was also an important factor.

1.2. Introduction to Stick-Slip Sliding

Imagine two blocks held together. Now the bottom block suddenly begins sliding. What might happen? Looking closely in very small time segments at the sliding will reveal the following demonstration seen in Figure 1.4.

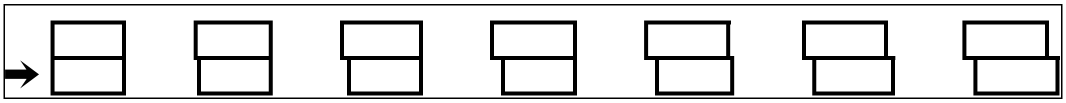

Figure 1.4: Blocks Demonstrating Sliding Behavior

Note that the bottom block does not simply translate to a new position but instead the left side begins to inch its way over and then finally the right side begins to inch its way over until the actual sliding displacement has occurred. This is a demonstration of what is happening during the stick-slip sliding. But how would anyone be able to catch a glimpse of this stick-slip sliding without special equipment? Imagine a sponge that is setting on top of a kitchen counter. If one side of the sponge was held with one hand while pushing or scrunching up the other end, the sponge would constrict. After releasing the sponge, it would then appear to "grow" while it was instead just finishing its forward movement. This can be seen illustratively in Figure 1.5.

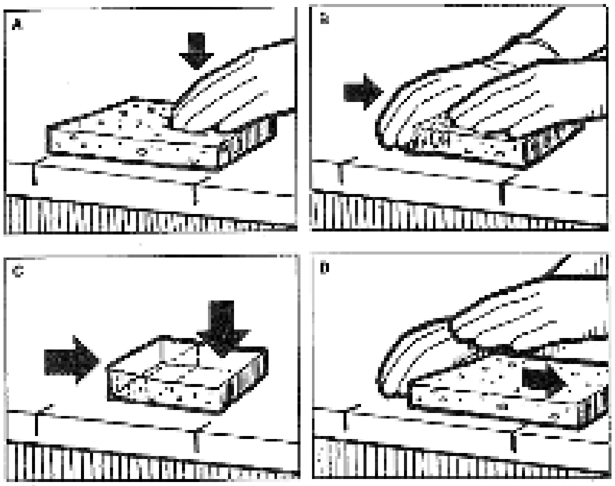

Figure 1.5: Moving a sponge to demonstrate stick-slip behavior

The area of the sponge that is contracting together before it is released is illustrative of sticking in a dynamic frictional stick-slip event. Similarly, as the sponge is released it is reminiscent of the slip pulse associated with stick-slip sliding. This stick-slip sliding occurs not only with a sponge and a counter top, but also could occur between any two objects under the right physical conditions.

CHAPTER 2

REVIEW OF LITERATURE

2.1. Friction Laws

Frictional sliding is important to many different fields including geophysical faulting, composite fracture behavior, machining, and behavior between moving and fixed mechanical parts. In the case of geophysical faulting, constitutive rate-state laws were introduced in order to match the recent observations of dynamic friction experiments on rocks (Dieterich 1979). In recent sliding experiments to simulate fault-like behavior, it was noticed that there was not only an instantaneous dependence on the rate of sliding but also on the dependence of the evolving state (Rice & Ruina 1983). So not only is the frictional behavior dependent on the sliding rate but also on its past history. And so, as previously discussed, Coulomb's Law could not be considered fully adequate to cover these changes in frictional sliding behavior and thus some constitutive rate-state laws emerged.

In addition, the use of these rate-state friction laws allowed the numerical simulations with stable numerical algorithms which allowed the observation of new types of sliding behavior that the use of Coulomb's Law did not allow (Ranjith and Rice 1999, Lapusta et al. 2000, Povirk and Needleman 1993, Marone 1998, Coker et al. 2005). This driving application was the modeling of which was later adapted to applications such as geophysical faulting and also in fiber pull-out (Tsai and Kim 1996) and other frictional model experiments used to examine the effects of frictional sliding of engineering materials.

2.2. Observed Sliding Modes in Dynamic Friction

Numerical studies and laboratory experiments generally find two types of frictional sliding which will be referred to as frictional sliding modes in this research paper. Povirk and Needleman (1993) implemented a rate-state constitutive frictional law into a finite element code in order to simulate a single fiber being pulled out of a surrounding matrix. They reported stick-slip behavior during this fiber pull-out process in addition to steady sliding. Not only was the stick-slip behavior discovered during the fiber pull-out process but also in earthquake faulting as well. Ben-Zion and Huang (2002) studied the dynamic rupture along an interface fault zone between two rock models. In fact, they report that the observation of pulses is occurring and has the tendency to grow in velocity and to be a set distance of nearly 25.5 km apart from one another along the fault. The plot shown in Figure 2.1 is describing the time history of the slip pulses at different locations along the fault zone line.

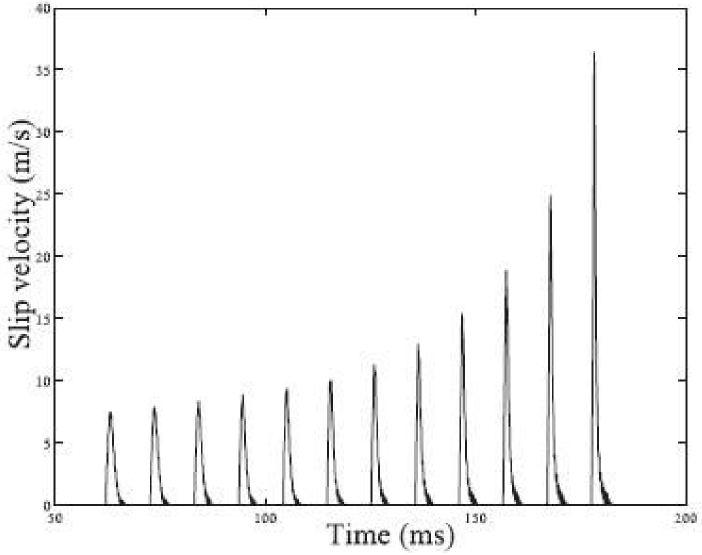

Figure 2.1: Time History of Slip Pulse Along Fault (Ben-Zion and Huang 2002)

Similar pulses were also found by Coker et al. (2005) when they performed numerical simulations using a finite element code that implemented a constitutive rate-state law where the dynamic sliding of a plate subjected to impact was incorporated. Their model setup is identical to the setup used in this research paper and was briefly discussed in Section 1.2 above. In laboratory experiments, Coker et al. (2005) and Lykotrafitis et al. (2006) found not only crack-like sliding but pulse-like sliding as well. Their experiments were conducted using two Homalite plates that were being held together and a projectile was then fired at one of the plates to generate sliding. Coker et al. (2005) also performed experiments and captured similar results. The findings also showed crack-like sliding with a possible pulse-like sliding in some cases. These laboratory findings allowed for numerical studies to look further into these pulse-like and crack-like sliding cases with some qualitative validation of such results.

Coker et al. (2005) began to study the different types of sliding that they observed and found multiple sliding modes. Along with the crack-like sliding mode they report that there are two different stick-slip modes (train of pulses and growing pulses). With this in mind, there are questions as to what other types of sliding might be occurring under similar circumstances.

2.3. Crack Tip Velocity

In numerical simulations, the crack tip speed of the front wave for the frictional sliding has been studied. In work done by Coker et al. (2005), they not only studied numerical simulations but some experimental data as well. The crack tip velocities for experimental and numerical cases are plotted in Figure 2.2.

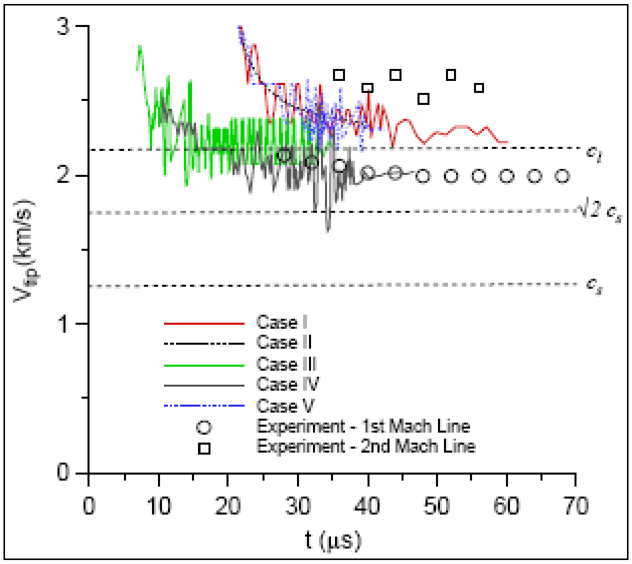

Figure 2.2: Crack Tip Velocities (Coker et al. 2005)

In these simulations, Coker et al. (2005) found that the crack tip propagated at supersonic speeds shown by solid lines in Figure 2.2. However, experiments have shown frictional sliding that has intersonic crack tip velocities between the longitudinal wave speed (denoted by c_l) and the critical crack tip speed of the Homalite material (denoted by $\sqrt{2}c_s$ where c_s is the shear wave speed). Crack tip speeds will be further investigated numerically in this research study.

2.4. Research Objectives

The main objective of this research is to more thoroughly search for and analyze the frictional sliding modes using a finite element method that incorporates a rate-state dependent friction law. The work that has been previously done is not entirely conclusive and was not done in detail. It is expected that multiple sliding modes might be found and so it will also be critical to analyze the stick-slip sliding that should be observed and determine what conditions might cause this versus crack-like sliding.

Not only will the interfacial sliding be studied, but also there is some interest in what is actually happening along the interface. Therefore, the interface will also be closely examined to see what might be occurring during these dynamic frictional sliding events.

It is also important that numerical simulations can be done such that it simulates not only supersonic crack tip velocities but also intersonic crack tip speeds as observed in laboratory experiments. To do this, each simulation will be analyzed to determine the characteristics that might be largely be influencing the crack tip velocity. Then this information will be used to refine the computational simulation by changing input parameters in order to find a specific condition that might invoke these low crack tip velocities.

CHAPTER 3

THEORETICAL BACKGROUND

3.1. Rate-State Friction Law

A rate-state friction law needed to be chosen to model in the finite element simulations. The rate-state equation selected for use in the finite element model was adapted from work done by Dieterich (1979) and Rice & Ruina (1983). This form of the rate-state law represents the coefficient of friction as a function of sliding speed, $\dot{u}_{slip}$, and a state variable, θ, representing the contact quality between sliding surfaces.

$$\mu(\theta, \dot{u}_{slip}) = g(\theta) f(\dot{u}_{slip}) \tag{3.1}$$

where

$$f(\dot{u}_{slip}) = \left(\frac{\dot{u}_{slip}}{V_0} + 1 \right)^{1/m} \tag{3.2}$$

and

$$g(\theta) = \frac{\mu_d + (\mu_s - \mu_d) \exp\left[-\left(\frac{L_0 / \theta}{V_1} \right)^p \right]}{\left(\frac{L_0 / \theta}{V_0} + 1 \right)^{1/m}} \tag{3.3}$$

where L_0 is the characteristic length, V_0 and V_1 are both constants with units of velocity, μ_s is the static coefficient of friction, and μ_d is the dynamic coefficient of friction. It is also important to note that the internal state variable characterizing the state of contact between two surfaces, θ, has units of time. The evolution of this internal state variable, θ, is given by the following differential equation:

$$\dot{\theta} = B\left(1 - \frac{\theta \dot{u}_{slip}}{L_0}\right) \tag{3.4}$$

where $B = \dot{\theta}_0$. Values are required for the constants in the equations mentioned above. The purpose of these constant values is then to take the rate-state law and "match it" with the experimental results obtained in previous laboratory examples by those of Dieterich (1979), Rice & Ruina (1983), and others. These constant values were obtained from Coker et al (2004) because they have been used in the same rate-state law previously. However, the values were manipulated to see what their effects were on the frictional model. It was determined that changing these values did not cause the model to fit the data any better. Thus, it was decided to use the original values from Coker et al (2004) shown below in Table 3.1:

μ_s	**0.6**
μ_d	**0.5**
V_0	**100**
V_1	**26**
p	**1.2**
m	**5**
L_0	**0.00002**

Table 3.1: List of Constants used in Rate-State Law

3.2. Steady-State Frictional Behavior

It is also important to look at the steady-state behavior of the coefficient of friction in Equation 3.1. Thus, plugging in $\dot{\theta} = 0$ to obtain steady-state sliding yields the following result:

$$\dot{\theta}_{ss} = 0 = B\left(1 - \frac{\theta_{ss}\dot{u}_{slip}}{L_0}\right) = 1 - \frac{\theta_{ss}\dot{u}_{slip}}{L_0}$$

$$\frac{\theta_{ss}\dot{u}_{slip}}{L_0} = 1 \tag{3.5}$$

$$\theta_{ss} = \frac{L_0}{\dot{u}_{slip}}$$

Substituting this steady-state value of θ back into Equation 3.3 yields the following:

$$g(\theta_{ss}) = \frac{\mu_d + (\mu_s - \mu_d)\exp\left[-\left(\frac{L_0 / (L_0 / \dot{u}_{slip})}{V_1}\right)^p\right]}{\left(\frac{L_0 / (L_0 / \dot{u}_{slip})}{V_0} + 1\right)^{1/m}}$$

$$g(\theta_{ss}) = \frac{\mu_d + (\mu_s - \mu_d)\exp\left[-\left(\frac{\Delta\dot{u}_{slip}}{V_1}\right)^p\right]}{\left(\frac{\Delta\dot{u}_{slip}}{V_0} + 1\right)^{1/m}} \tag{3.6}$$

Then again inserting Equations 3.2 and 3.6 into Equation 3.1 yields the steady-state expression for the coefficient of friction, μ_{ss}, as can be seen in Equation 3.7.

$$\mu\left(\theta_{ss},\dot{u}_{slip}\right)=\mu_{ss}=\left(\frac{\mu_d+\left(\mu_s-\mu_d\right)\exp\left[-\left(\frac{\dot{u}_{slip}}{V_1}\right)^p\right]}{\left(\frac{\dot{u}_{slip}}{V_0}+1\right)^{1/m}}\right)\left(\frac{\dot{u}_{slip}}{V_0}+1\right)^{1/m}$$

$$\mu_{ss}=\mu_d+\left(\mu_s-\mu_d\right)\exp\left[-\left(\frac{\dot{u}_{slip}}{V_1}\right)^p\right] \tag{3.7}$$

Constants from Table 3.1 (discussed previously) were then inputted into Equation 3.7. This resultant steady-state coefficient of friction, μ_{ss}, was then plotted with respect to the non-dimensionalized slip velocity variable, $\frac{\dot{u}_{slip}}{V_1}$, and can be seen in the following figure:

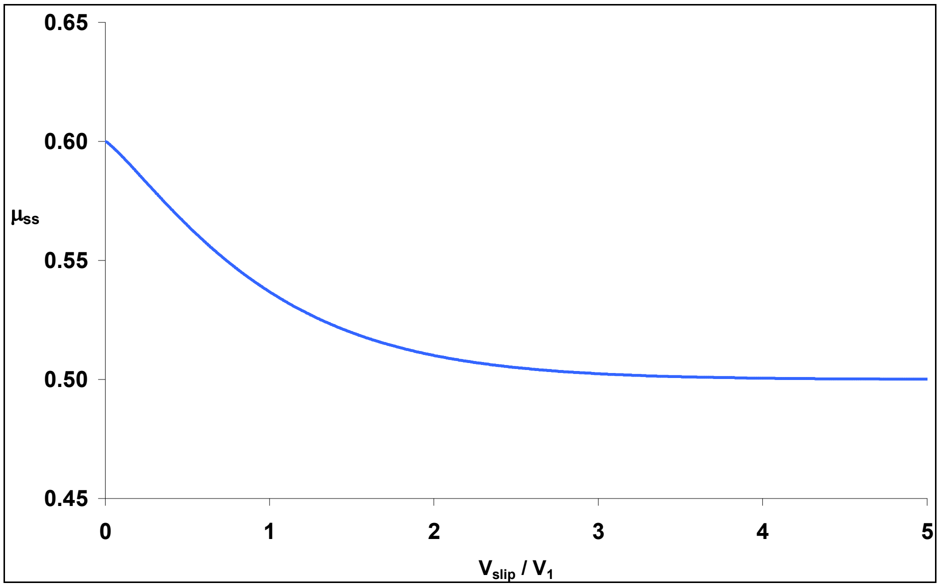

Figure 3.1: Steady-State Friction Coefficient vs. Non-Dimensionalized Slip Velocity

As can be seen from Figure 3.1, the coefficient of friction begins at the static coefficient of friction value of 0.6 and then within four to five time steps (where one time step is equal to a value of one for the non-dimensionalized slip velocity variable) it reaches a steady-state value of 0.5 which is the coefficient of dynamic friction value.

3.3. Non Steady-State Frictional Behavior

Now that a steady-state representation of the coefficient of friction has been shown in a single equation format, the next objective is to find an expression for the coefficient of friction when it is not under steady-state sliding. The steady-state conditions do not apply when $\dot{\theta}$ takes on a non-zero value. Applying this condition requires the differential equation stated previously in Equation 3.4 to be solved. First, the equation is manipulated using a fundamental calculus approach as follows:

$$\dot{\theta} = \frac{\partial \theta}{\partial t} = B\left(1 - \frac{\theta \dot{u}_{slip}}{L_0}\right)$$

$$\frac{d\theta}{\left(1 - \frac{\theta \dot{u}_{slip}}{L_0}\right)} = Bdt \tag{3.8}$$

Now that like terms have been grouped and sorted to each side of the equation, the next step is to integrate both sides:

$$\int \frac{1}{\left(1 - \frac{\theta \dot{u}_{slip}}{L_0}\right)} d\theta = \int Bdt$$

$$-\frac{\dot{u}_{slip}}{L_0} \ln\left(1 - \frac{\theta \dot{u}_{slip}}{L_0}\right) = Bt + C_1 \tag{3.9}$$

All that remains to do in order to simplify this equation are a few simple algebra techniques. The left-hand side is first reduced down to only its logarithm term.

$$\ln\left(1-\frac{\theta\dot{u}_{slip}}{L_0}\right)=-\frac{L_0}{\dot{u}_{slip}}Bt-\frac{L_0}{\dot{u}_{slip}}C_1$$

$$\ln\left(1-\frac{\theta\dot{u}_{slip}}{L_0}\right)=-\frac{L_0}{\dot{u}_{slip}}Bt+C_2 \tag{3.10}$$

The logarithmic equation is then rewritten in an exponential form to simplify Equation 3.10 even further.

$$1-\frac{\theta\dot{u}_{slip}}{L_0}=e^{-\frac{L_0}{\dot{u}_{slip}}Bt}e^{C_2}$$

$$1-\frac{\theta\dot{u}_{slip}}{L_0}=C_3e^{-\frac{L_0}{\dot{u}_{slip}}Bt} \tag{3.11}$$

It is important to note that the desired equation needs to be a function of the following form, $\theta(t)$. Thus, the equation is then rearranged to solve for θ:

$$\frac{\theta\dot{u}_{slip}}{L_0}=1-C_3e^{-\frac{L_0}{\dot{u}_{slip}}Bt}$$

$$\theta=\frac{L_0}{\dot{u}_{slip}}-\frac{L_0}{\dot{u}_{slip}}C_3e^{-\frac{L_0}{\dot{u}_{slip}}Bt}$$

$$\theta(t)=\frac{L_0}{\dot{u}_{slip}}+C_4e^{-\frac{L_0}{\dot{u}_{slip}}Bt} \tag{3.12}$$

In order to solve for the integration constant, C_4, an initial condition of $\theta=\theta_0$ at $t=0$ must be applied.

$$\theta(0)=\theta_0=\frac{L_0}{\dot{u}_{slip}}+C_4e^{-\frac{L_0}{\dot{u}_{slip}}B(0)}$$

$$\theta_0=\frac{L_0}{\dot{u}_{slip}}+C_4$$

$$C_4 = \theta_0 - \frac{L_0}{\dot{u}_{slip}} \tag{3.13}$$

But, this integration constant C_4 is not necessarily valid for all times, t_0. What if the sliding velocities suddenly changed? Then t_0 might not be zero and then using the variable $\theta_0 = \theta(t_0)$ in the constant's expression would be misleading. Instead, think of these velocity jumps occurring at any given time $t = t_n$ where $\theta(t_n) = \theta_n$. Then, recalculating the integration constant to account for this change yields the following result:

$$\theta(t_n) = \theta_n = \frac{L_0}{\dot{u}_{slip}} + C_4^{(n)} e^{-\frac{L_0}{\dot{u}_{slip}} B t_n}$$

$$C_4^{(n)} e^{-\frac{L_0}{\dot{u}_{slip}} B t_n} = \theta_n - \frac{L_0}{\dot{u}_{slip}}$$

$$C_4^{(n)} = \left(\theta_n - \frac{L_0}{\dot{u}_{slip}} \right) e^{\frac{L_0}{\dot{u}_{slip}} B t_n} \tag{3.14}$$

Taking this more diverse constant and plugging back into Equation 3.12 yields the following for an expression of the time history variable, θ:

$$\theta(t)=\frac{L_0}{\dot{u}_{slip}}+C_4 e^{-\frac{L_0}{\dot{u}_{slip}}Bt}$$

$$\theta(t)=\left[\left(\theta_n-\frac{L_0}{\dot{u}_{slip}}\right)e^{\frac{L_0}{\dot{u}_{slip}}Bt_n}\right]e^{-\frac{L_0}{\dot{u}_{slip}}Bt}+\frac{L_0}{\dot{u}_{slip}}$$

$$\theta(t)=\left(\theta_n-\frac{L_0}{\dot{u}_{slip}}\right)e^{\frac{L_0}{\dot{u}_{slip}}Bt_n-\frac{L_0}{\dot{u}_{slip}}Bt}+\frac{L_0}{\dot{u}_{slip}}$$

$$\theta(t)=\left(\theta_n-\frac{L_0}{\dot{u}_{slip}}\right)e^{\frac{L_0}{\dot{u}_{slip}}B(t_n-t)}+\frac{L_0}{\dot{u}_{slip}} \tag{3.15}$$

The finalized equation demonstrated above in Equation 3.15 was then written into an Excel VBA code. A counting variable, delta, was used instead of the time parameter in previous codes of this nature and so a relation of time to delta was also inputted into the program using the following relations:

$$delta=\frac{u_{slip}}{L_0}=\frac{u_{slip}}{L_0}\cdot\frac{t}{t}=\frac{\dot{u}_{slip}}{L_0}t$$

$$t=\frac{L_0}{\dot{u}_{slip}}delta \tag{3.16}$$

A loop was then used to form a time array that was used to calculate the time history variable, θ, for each time step. These values for θ were then plugged back into Equations 3.2 and 3.3 in order to solve for the coefficient of friction as defined in Equation 3.1 previously. The constants were inputted into the program from the previous list from Table 3.1. Next, three different sliding velocities were inputted into the program so that the simulation would experience a sudden increase and decrease in sliding velocities. These velocities were 10 m/s, 100 m/s, and 30 m/s. The following figure shows the coefficient of friction as a function of delta for the three different applied velocity jumps along with Amontons-Coulomb's law for comparison (purple):

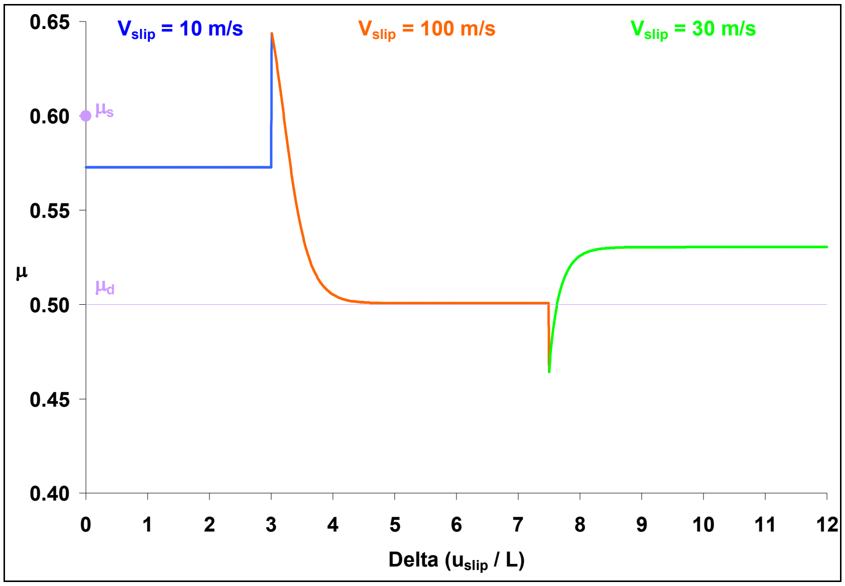

Figure 3.2: Rate-State Friction Coefficient vs. Delta

From Figure 3.2 it is interesting to note that while the dynamic coefficient of friction was inputted as 0.5, the rate-state law did not reach this value until a much larger sliding velocity of 100 m/s was felt. And although the dynamic coefficient of friction was not attained during the simulation of a sliding velocity of 10 m/s, the frictional coefficient did overcome the static coefficient of friction (0.6) and did maintain a steady value below that. Once a higher sliding velocity was inputted, the coefficient of friction first spiked up to a higher value and then dropped in an exponential form as opposed to an immediate drop as one might have expected. It then reached a steady frictional coefficient equal to that of the dynamic coefficient of friction (0.5). Similarly, when the sliding speed was decreased significantly, the frictional coefficient spiked first to a lower value and then increased logarithmically to a steady value above that of the dynamic coefficient of friction but still below the static frictional coefficient value. This information matches well with other experimental data and so it was concluded that this particular rate-state law from Dieterich (1979) and Rice & Ruina (1983) would hold and was sufficiently good for our finite element model simulations.

CHAPTER 4

NUMERICAL IMPLEMENTATION

4.1. Finite Element Method Mesh Setup

The finite element code was used to simulate frictional sliding between two plates as might occur in an earthquake. Homalite was chosen as the material to model because of its similarities with rock as previously discussed in the introduction section. The numerical model is then comprised of two rectangular plates held together by a compressive load, σ_o. An impact velocity is also utilized to initiate sliding and is an input to the finite element code along with the compressive load. A numerical model setup is shown in Figure 4.1 below.

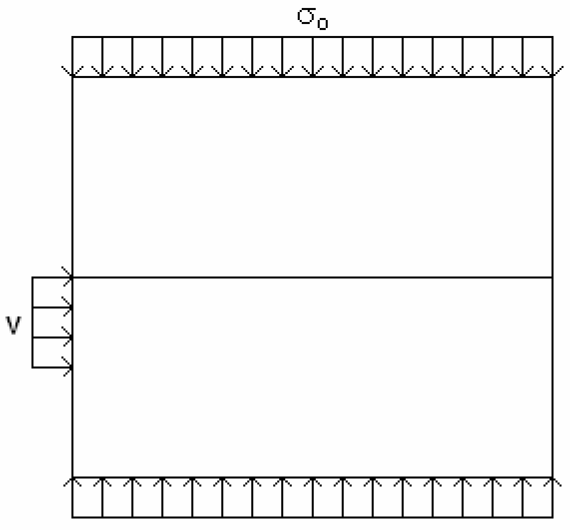

Figure 4.1: Finite Element Model Loading and Geometry

The figure below shows the mesh used in the finite element code simulations.

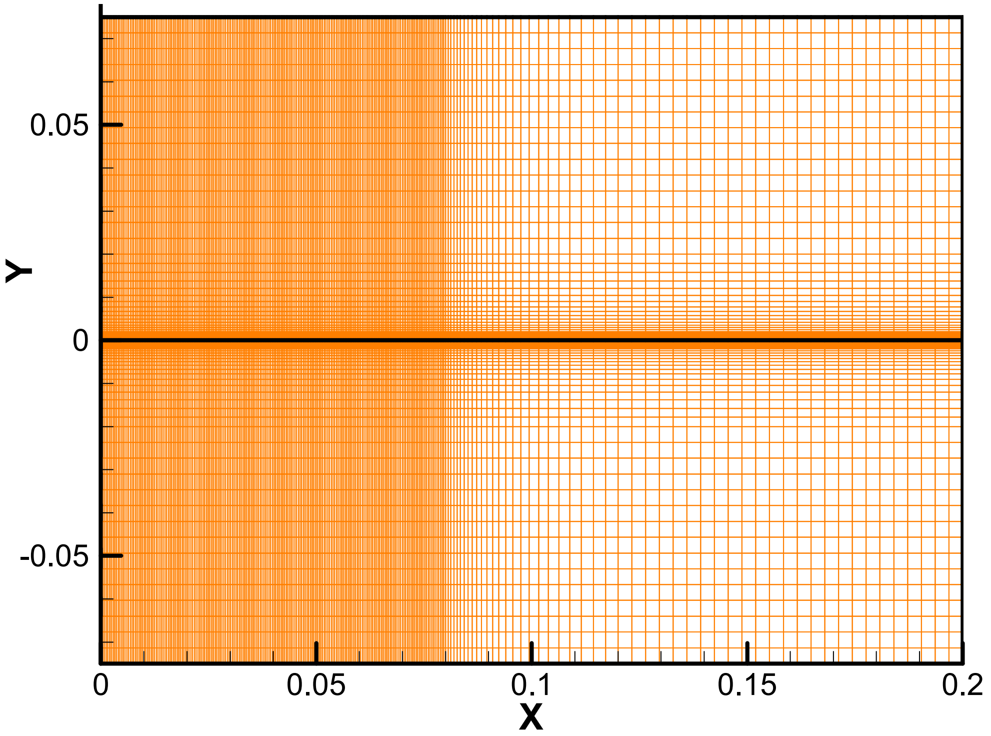

Figure 4.2: Finite Element Model Mesh (lengths measured in meters)

As can be seen from the figure, the left-hand side is comprised of a very fine, uniform mesh until $x = 0.08$ meters which then becomes a transitional region which gradually increases in coarseness until it reaches $x = 0.12$ meters where the mesh becomes uniform again. Each mesh or rectangular plate was made to be 200 millimeters long and 75 millimeters in height as shown above in Figure 4.2. The impact velocity is chosen to simulate a projectile striking the lower plate on the left-hand side as shown above in the numerical model setup (Figure 4.1). The impact velocity profile is shown in the following figure.

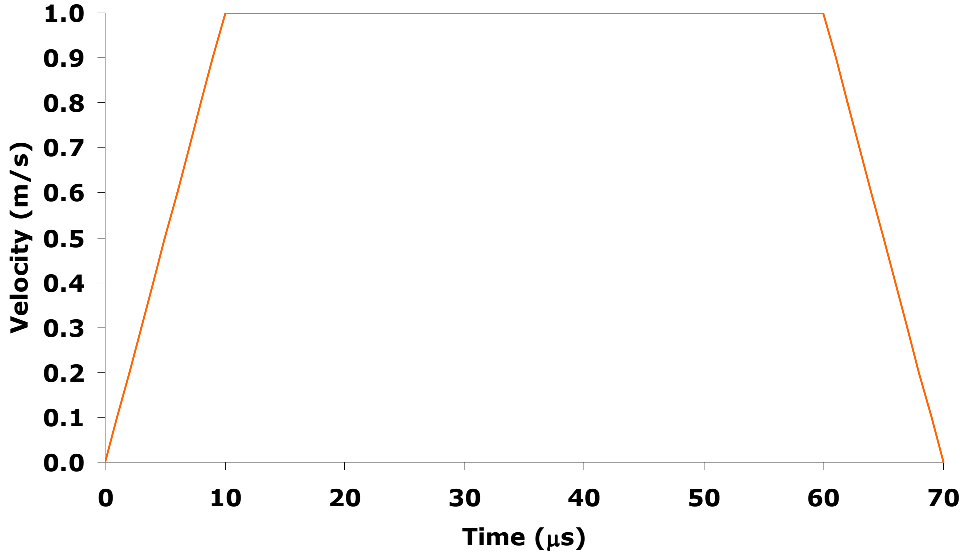

Figure 4.3: Impact Velocity Profile

Figure 4.3 gives the velocity profile that was used in each of the numerical simulations presented in this research. The profile was chosen based on experiments conducted of a projectile hitting a plate which was done in the laboratory and discussed later in Section 4.4.

The Homalite plates modeled in the finite element code have material properties representative of Homalite-100 as shown in Table 4.1.

E (GPa)	ν	ρ (kg/m^3)	c_l (m/s)	c_s (m/s)	c_R (m/s)
5.3	0.35	1246	2201	1255	1170

Table 4.1: Homalite-100 Material Properties

The table above shows the Young's modulus E, Poisson's ratio ν, density ρ, longitudinal wave speed c_l, shear wave speed c_s, and Rayleigh wave speed c_R. These wave speeds were determined using the following equations for plane stress:

$$c_l = \sqrt{\frac{E}{\rho\left(1-\nu^2\right)}}, \quad c_s = \sqrt{\frac{E}{2\rho\left(1+\nu\right)}}, \quad c_R = c_s \frac{0.86+1.14\nu}{1+\nu} \tag{4.1}$$

4.2. Fundamental Equations

The finite element code has two constitutive relations consisting of the bulk material constitutive law relating the stresses and strains in the material along with the cohesive law that gives the relation along the interface. The material law governs an isotropic hyperelastic solid while the constitutive cohesive law utilizes the rate-state model discussed in the previous chapter which relates the traction rates to the displacement jumps. The principal virtual work used in the finite element code is shown below and has also been discussed in Needleman (1987) and Xu and Needleman (1994).

$$\int_V \mathbf{S} : \delta\mathbf{E} dV - \int_{S_{\mathrm{int}}} \mathbf{T} \cdot \delta\boldsymbol{\Delta} dS = \int_{S_{ext}} T \cdot \delta\mathbf{u} dS - \int_V \rho \frac{\partial^2 \mathbf{u}}{\partial t^2} \cdot \delta\mathbf{u} dV \tag{4.2}$$

where **S** is the second Piola-Kirchhoff stress tensor, **u** is the displacement vector, **Δ** is the displacement jump across the cohesive surface, V is the volume, S_{int} is the interfacial cohesive surface area, S_{ext} is the external surface area, and the relation **A : B** denotes $A^{ij}B_{ji}$. Further, the displacement jump and traction relation on the interface is given by the following relations.

$$\begin{aligned} \dot{T}_n &= -C_n \Delta\dot{u}_n \\ \dot{T}_s &= C_s \left[\Delta\dot{u}_s - \mathrm{sgn}(T_s) \dot{q}_{slip} \right] \end{aligned} \tag{4.3}$$

where $\dot{q}_{slip}$ is the sliding rate at the interface. The expression for the slip or sliding rate is the dependent relation shown below:

$$\dot{q}_{slip} = \begin{cases} \dot{q}_0 \left(\beta^m - 1 \right) & \text{for } \beta > 1 \\ 0 & \text{for } \beta \leq 1 \end{cases} \tag{4.4}$$

where β is defined as shown in Equation 4.5.

$$\beta = \frac{|T_s|}{T_n g(\theta)} \tag{4.5}$$

The friction equations are then updated using a single step tangent modulus method for rate dependent solids (Peirce et al. 1984).

4.3. Sliding Velocity Calculation

The following equation is used to calculate the change in sliding (horizontal) velocity:

$$\Delta u(t) = u_x^+ - u_x^- \tag{4.6}$$

where u_x is the displacement in the x-direction of an interfacial point and is described illustratively the following figure:

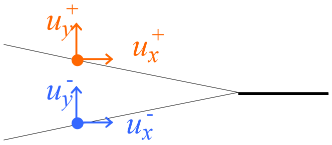

Figure 4.4: Exaggerated Illustration of Sliding Displacements

Although this appears to be a crack-like opening it is in fact an exaggerated view of the two surfaces that are sliding atop one another. Thus the sliding displacements denoted with a positive superscript represent the upper interface and the negative superscript denotes the sliding displacement for the bottom interface. The relative slip velocity can be found using a derivative definition as described in Equation 4.7 below.

$$\dot{q}_{slip} = \frac{\Delta u(t+\Delta t) - \Delta u(t)}{\Delta t} \tag{4.7}$$

4.4. Laboratory Experiments

Experiments were done to validate this program as described in Coker et al. (2005). Their laboratory setup very closely matches the setup described above in for this numerical research done in finite element code.

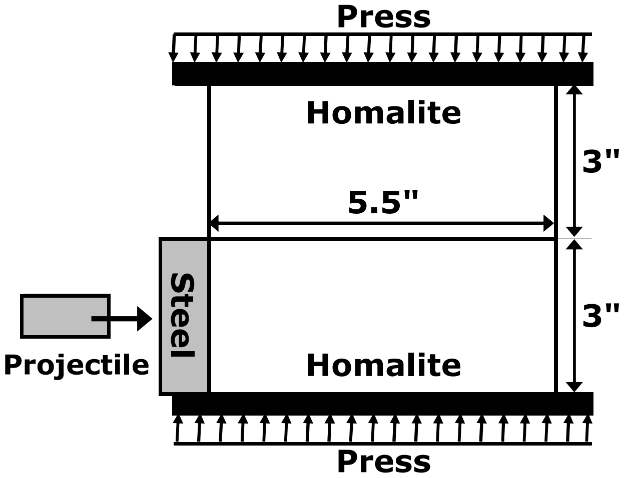

Figure 4.5: Experimental Setup (Coker et al. 2004)

The projectile was shot from close range at the steel plate pushing the bottom plate to initiate frictional sliding between the two Homalite plates. To insure that the projectile was shot horizontally and not at an angle, the impression left behind on the steel plate was observed before any results were considered.

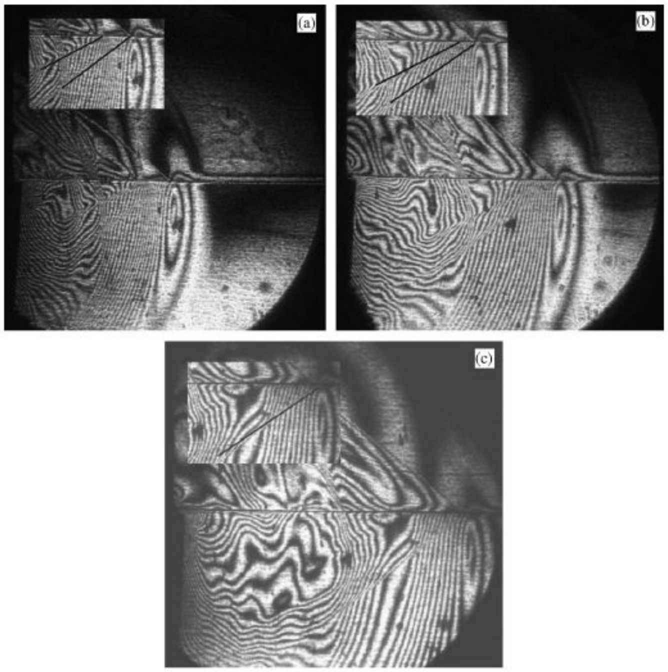

Figure 4.6: Experimental isochromatic fringe patterns from a dynamic friction experiment on Homalite subject to a static compressive stress of 9.4 MPa and impact velocity of 42 m/s, at (a) t = 40 μs; (b) t = 48 μs; (c) t = 60 μs: In the inset one or more lines are drawn to highlight Mach lines. The field of view is 130 mm in diameter (Coker et al. 2004)

The figures show the isochromatic fringe patterns captured by photoelastic equipment in conjunction with a high speed camera at three different times: 40 μs, 48 μs, 60 μs. The progress of the impact wave in the bottom plate with time can be observed. Immediately following the impact wave front, a stress concentration follows with a shear mach wave emanating at two angles from two different points. Even though they are separate initially at 40 μs they eventually coalesce at 60 μs with the back shear mach wave traveling faster and reaching the front wave. Coker et al. (2005) have shown similar behavior using finite element analysis that indicating the experimentally observed fringes could represent unsteady slip-pulse. In addition, Lykotrafitis et al. (2006) made measurements of the particle velocity at the interface proving the existence of slip-pulses.

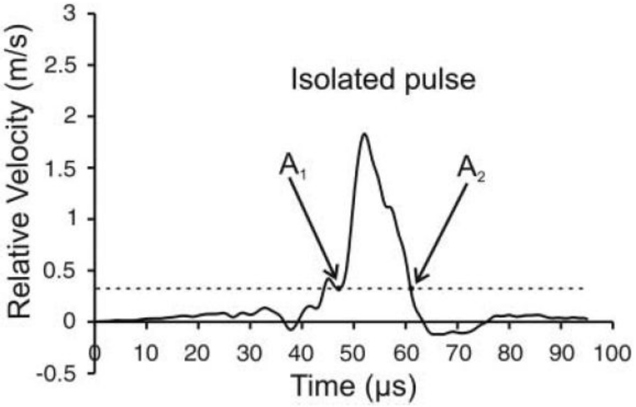

Figure 4.7: The relative sliding speed of a point at the interface located at a distance of 70 mm from the impact side of the Homalite plates shows an isolated pulse A_1 A_2. This experiment was done at 19 MPa and 10 m/s. (Lykotrafitis et al. 2006)

Not only did Lykotrafitis et al. (2006) find an isolated pulse, but they found a crack-like mode as well as seen in the following plot of Figure 4.8.

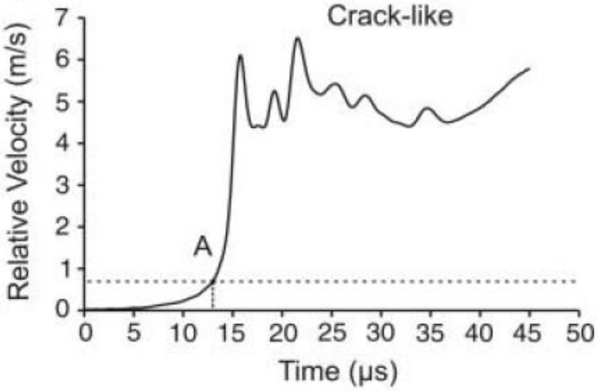

Figure 4.8: The relative sliding speed of a point at the interface located at a distance of 70 mm from the impact side of the Homalite plates shows a crack-like sliding mode. This experiment was done at 19 MPa and 19 m/s.

These laboratory experiments provide qualitative validation, however, the numerical characteristics do not line up perfectly with experiments because of the loading conditions and the parameters used in the friction law simulations.

CHAPTER 5

RESULTS AND OBSERVATIONS

5.1. Introduction into Observations of Different Sliding Modes

Finite element simulations were conducted with the material properties and friction constitutive properties fixed while varying the compressive load and impact velocities. The finite element loading and geometry is shown in Figure 4.1 and the model is shown in Figure 4.2. The frictional sliding starts between the plates at the impact point. the frictional sliding region then travels down the length of the interface finally moving the lower block with respect to the upper block as shown in Figure 5.1.

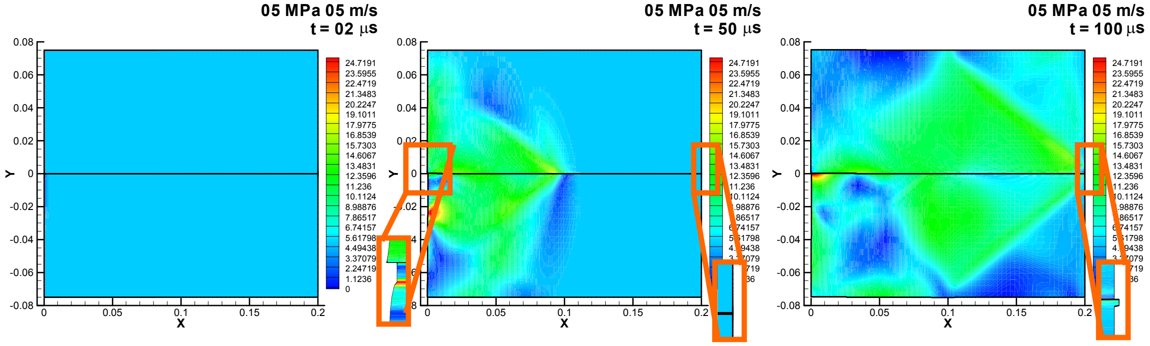

Figure 5.1: Stress contours of the bottom block sliding relative to the top block in three increasing time steps (from left to right): 2 μs, 50 μs, 100 μs.

Figure 5.1 shows the blocks sliding relative to each other in three separate stages. In the figure on the left the sliding is initiated with an impact velocity on the left wall near the interface. The middle plot not only shows the sliding of the blocks near the middle of the interface as the waves propagate along the interface but also that the bottom block has moved on the left wall but not at the right wall yet. The final figure shows that when the wave hits the right wall the block begins to move. However, the block has only moved where the sliding wave has reached. The rest of the right wall on the bottom block will move later when the remainder of the sliding waves reach these points. This gradual growth of the sliding region occurs in six sliding modes. These sliding modes are mapped in the compressive stress-impact velocity phase diagram in Figure 5.2.

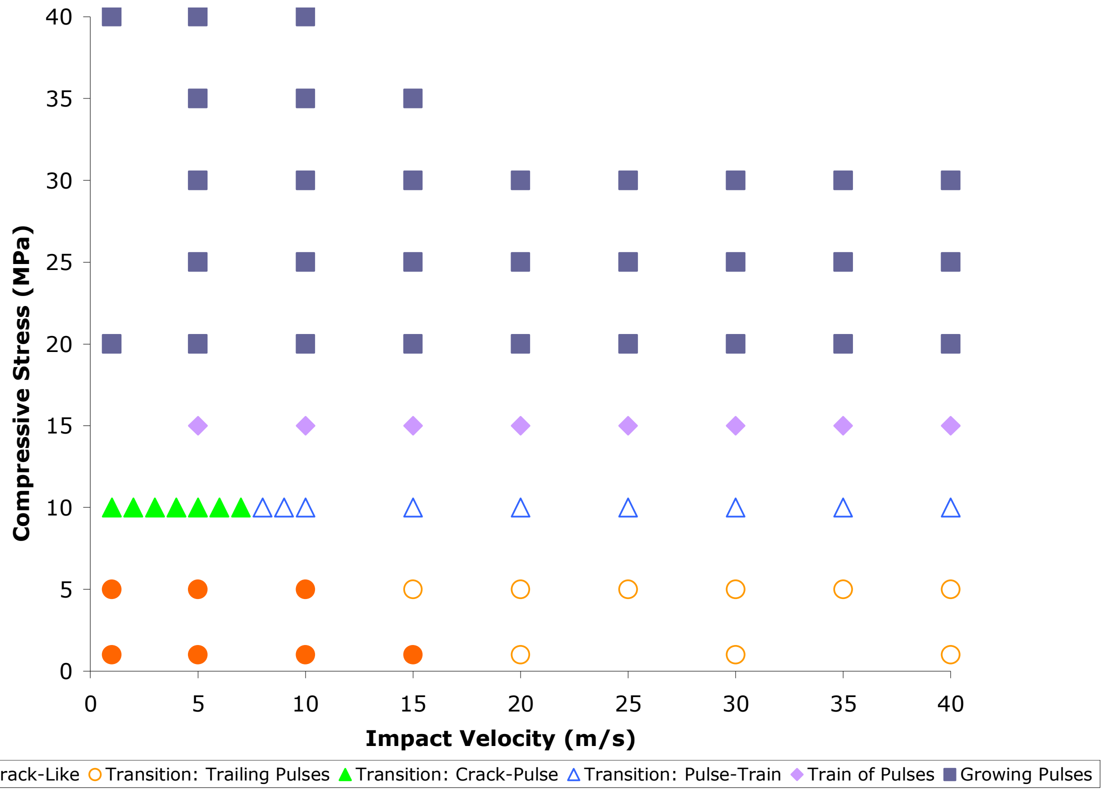

Figure 5.2: Frictional Sliding Modes Phase Diagram

The results will be presented in terms of tractions and sliding velocity along the interface along with stress contours at a fixed time. Using these outputs it was found that there were certain trends pertaining to the way the plates were sliding relative to one another based upon specific combinations of the compressive stress and impact velocity. The following subsections will not only discuss specific trends and traits pertaining to each mode, but will also show figures to further illustrate the modes.

5.1.1. Crack-Like Mode

The sliding velocity and shear stress plots of a typical crack-like mode are shown in Figure 5.3 below:

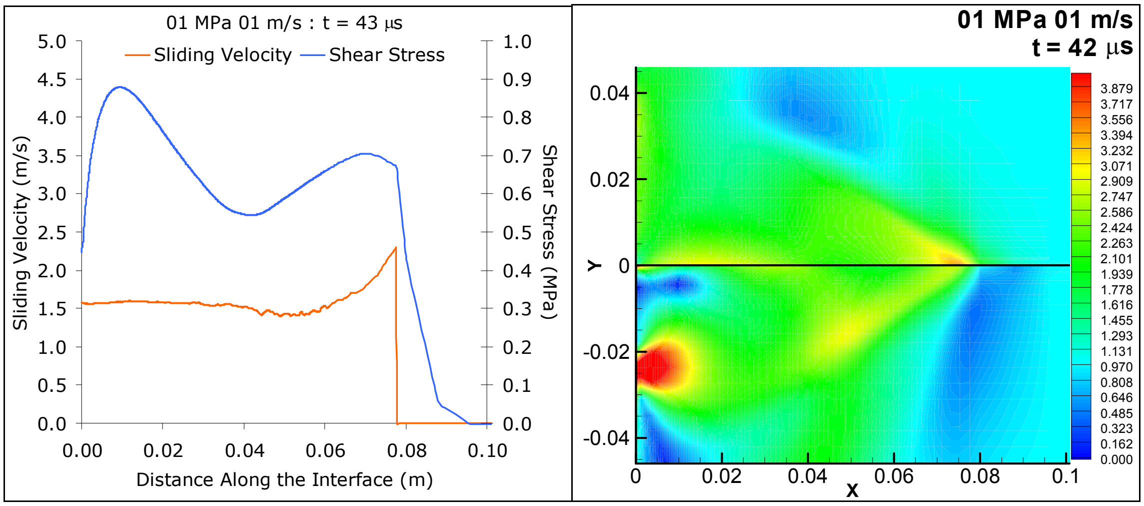

Figure 5.3: Crack-Like Sliding Velocity and Contour Stress Plots

The sliding velocity plot shown on the left of Figure 5.2 is plotted against the distance along the interface between the two rectangular Homalite plates. When looking at this slip velocity plot, some distinct features can be seen that exist only in the crack-like mode. For instance, the single leading pulse is followed by a nearly constant sliding velocity. This constant sliding velocity simulates constant crack growth. Thus, this type of frictional sliding is referred to as “crack-like sliding.” The figure below shows the data points plotted along with the solid line.

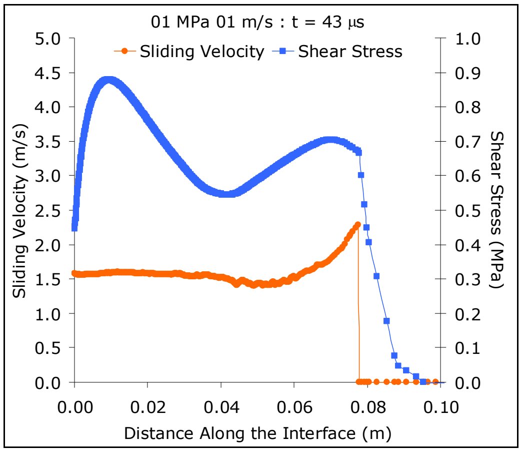

Figure 5.4: **Crack-Like Mode Sliding Velocity and Shear Stress Data Points**

As can be seen in Figure 5.4, the mesh is sufficiently refined to capture the gradual rise in the stresses along. However, the jump in the sliding velocity for this mode occurs almost instantaneously from one node to the other.

The stress contours plot shown on the right of Figure 5.2 is actually the plot of the contours of constant maximum shear stress. When looking at this stress plot, it can be seen that there is a leading wave followed by a sliding region that expands similar to a shear crack.

The normal tractions were also plotted together with the sliding velocity against the distance along the interface in Figure 5.5.

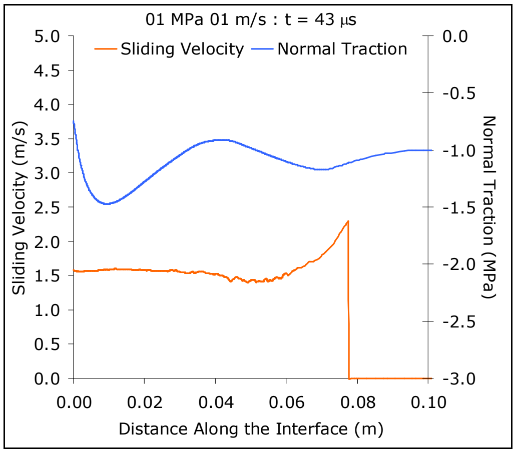

Figure 5.5: Crack-Like Normal Traction with Sliding Velocity plotted against the distance along the interface

The normal traction has the lowest value at the left wall. The normal traction does vary some, although not significant, and does not seem to be contributing to the sliding event itself.

Another analysis tool used was to look at the pulses themselves—more precisely, the pulse peak height (measured by order of magnitudes), the distance between the pulses, and the widths of the individual pulses. In the case of the crack-like sliding mode, the latter two analytic tools described above are not applicable since there is only a single peak and no real "pulse" to follow. Here it is important to note that a pulse will be used to describe a sliding velocity that goes from zero velocity to some maximum peak velocity and back down to zero velocity.

For this particular case of 1 MPa 1 m/s, the peak velocity is around 2.5 m/s. The following figure shows all of the peak velocities between times of 30 μs and 59 μs for each run in the crack-like case.

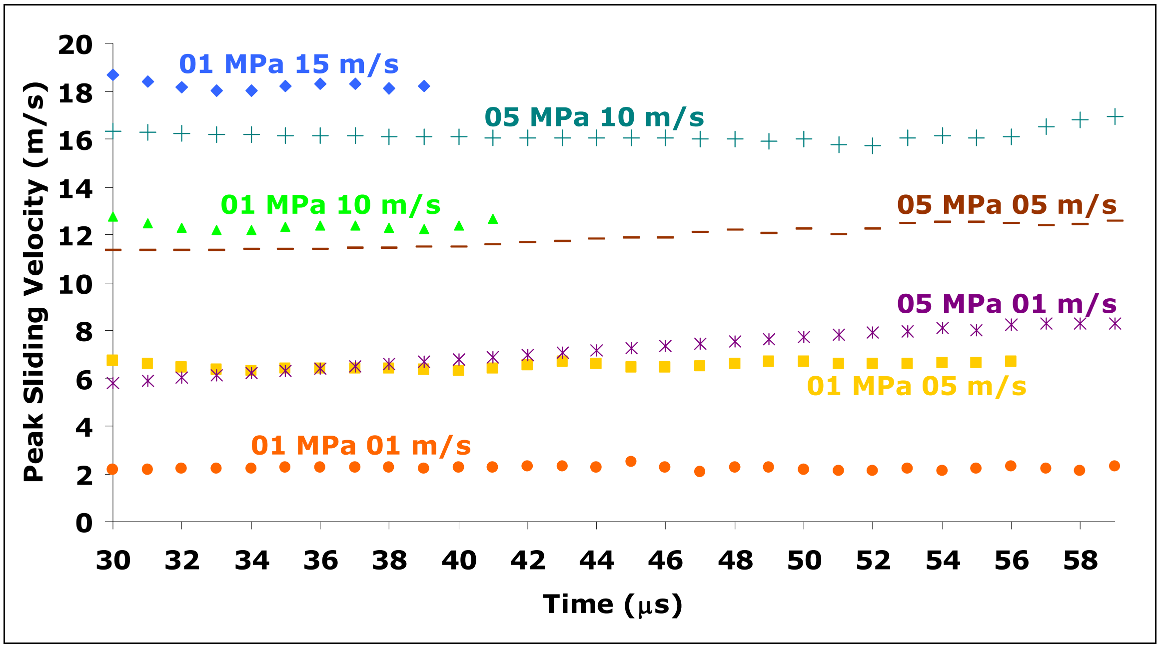

Figure 5.6: Crack-Like Sliding Velocity Peak vs. Time

The times of 30 μs to 59 μs were chosen to illustrate due to the fact that for all of the runs done for this research, most have sliding velocity peaks in this designated time region. However, as can be seen from the figure, not all of the runs will have the same time span available within their respective data sets. Holding the compressive stress constant at 1 MPa, and increasing the impact velocity in increments of nearly 5 m/s every time (the only exception being from 1 m/s to 5 m/s), the peak sliding velocity tends to increase by about 6 m/s throughout the trend as time increases. The same type of trend can be seen when the compressive stress is held at 5 MPa—as the impact velocity increases, the peak sliding velocity also increases by roughly 5 m/s. To illustrate the similarities between the different compressive stresses and trends, the following figure shows the sliding velocity for 5 MPa 10 m/s at a time that follows the trend at 43 μs.

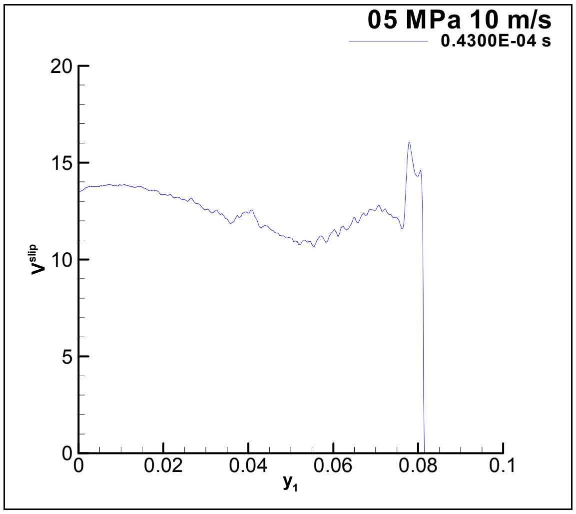

Figure 5.7: Sliding Velocity vs. Distance Along the Interface for 05 MPa 10 m/s

From the figure above, it is important to note that the front leading peak is beginning to form a leading pulse and has a peak velocity of 16 m/s. If the impact velocity is increased by an amount of 5 m/s (putting the total impact velocity input at 15 m/s) the sliding mode is no longer a crack-like mode but it begins to transition into a multi-pulse mode as discussed in the following sections. Similarly, if the compressive stress is increased by 5 MPa, then the leading near-pulse of the above crack-like case, actually forms into a leading pulse for a leading pulse transitional mode also discussed later on in this chapter.

5.1.2. Trailing Pulses Transitional Mode

The sliding velocity and stress plots for this sliding mode can be seen in the following figures:

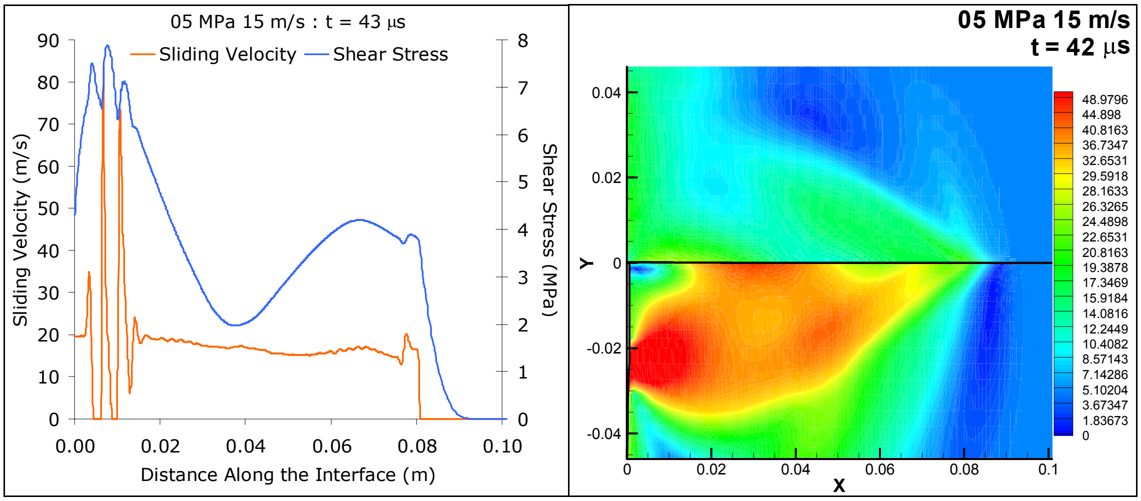

Figure 5.8: **Trailing Pulses Transitional Mode Sliding Velocity and Stress Plots**

Similar to the crack-like mode above, the trailing pulses transitional mode also has a single leading pulse followed by some constant crack-like sliding. However, unlike the crack-like mode, this transitional mode includes some significantly larger pulses that are trailing the crack-like sliding. Thus, this type of sliding is referred to as transitional trailing pulses. Figure 5.9 below shows the data points plotted for the shear stress and sliding velocity plot.

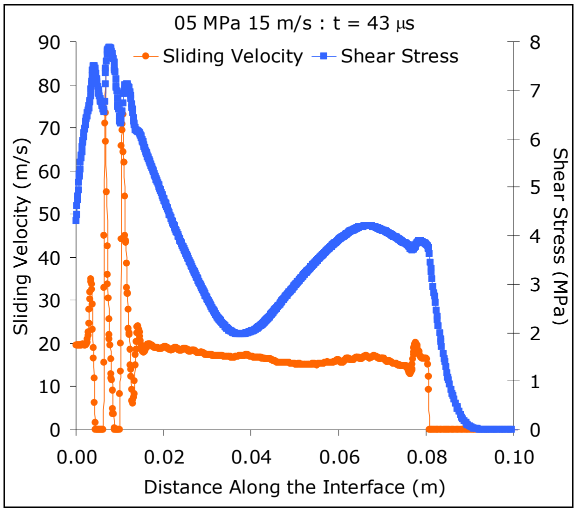

Figure 5.9: Crack-Like Mode Sliding Velocity and Shear Stress Data Points

The data points plotted above show again that the mesh is sufficiently fine and that the data is not mesh dependent. The normal traction is plotted below on the sliding velocity plot versus the distance along the interface.

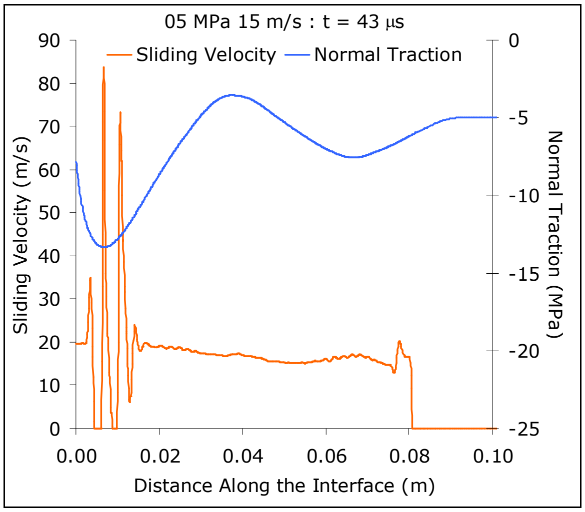

Figure 5.10: Transitional Trailing Pulses Sliding Mode Normal Traction with Sliding Velocity plotted against the distance along the interface

The normal traction increases just before the trailing pulses become evident. This will require further discussion later with sliding modes that include multiple pulses that are not just occurring in the rear.

5.1.3. Crack-Pulse Transitional Mode

The crack-pulse transitional mode sliding velocity and stress plots are shown below:

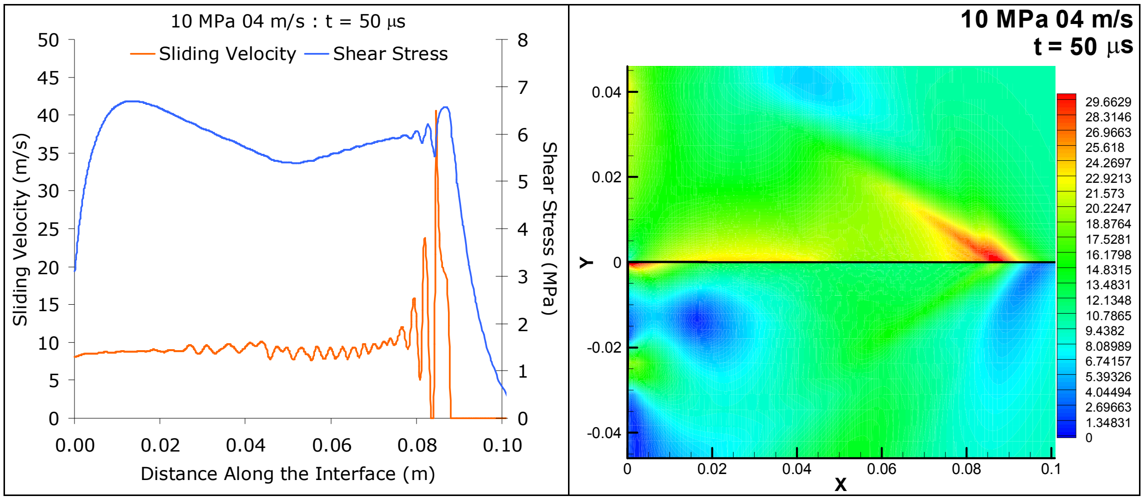

Figure 5.11: Crack-Pulse Transitional Mode Sliding Velocity and Stress Plots

Unlike the previous transitional mode of trailing pulses, this mode leads with at least one front pulse and trails with a crack-like sliding behind the front pulse(s). The leading pulse sliding velocity is an order of magnitude larger than the leading peak velocity of the crack-like sliding mode. There is also a region following the leading pulse that where the sliding velocity is beginning to stick or come to a zero velocity which is why this type of sliding is called the transitional crack-pulse mode.

The shear stress plotted on the sliding velocity plot of Figure 5.11 has a peak in the same region that the initial leading pulse is on the sliding velocity plot. The following figure shows the data points plotted on the sliding velocity and shear stress plot.

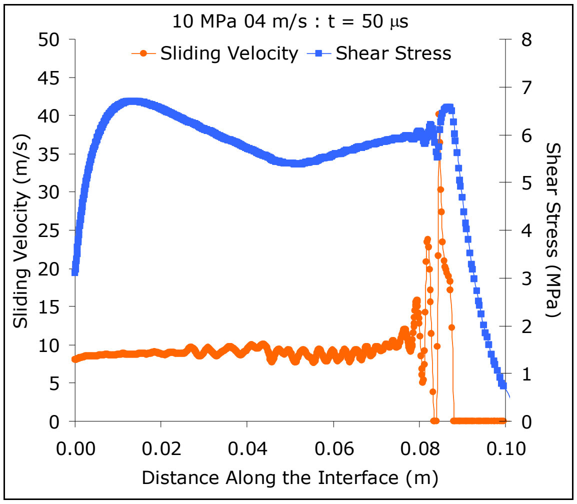

Figure 5.12: Crack-Pulse Transitional Mode Sliding Velocity and Shear Stress Data Points

Figure 5.12 shows that the data is again mesh independent for the crack-pulse transitional mode. The mesh is sufficiently fine such that the data points are accurately occurring. The normal traction is plotted against the distance along the interface with the sliding velocity in the following figure.

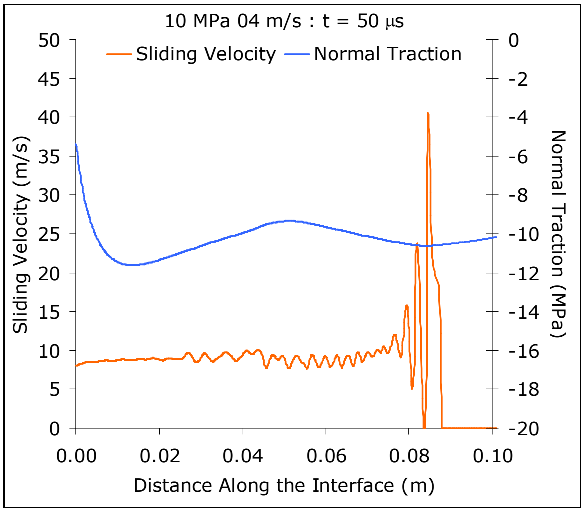

Figure 5.13: Crack-Pulse Transitional Mode Normal Traction with Sliding Velocity plotted against the distance along the interface

The normal traction is the lowest at the left wall, as was the case for each sliding mode discussed so far. The trend of the normal traction is similar and does not seem to be contributing to the actually frictional sliding event.

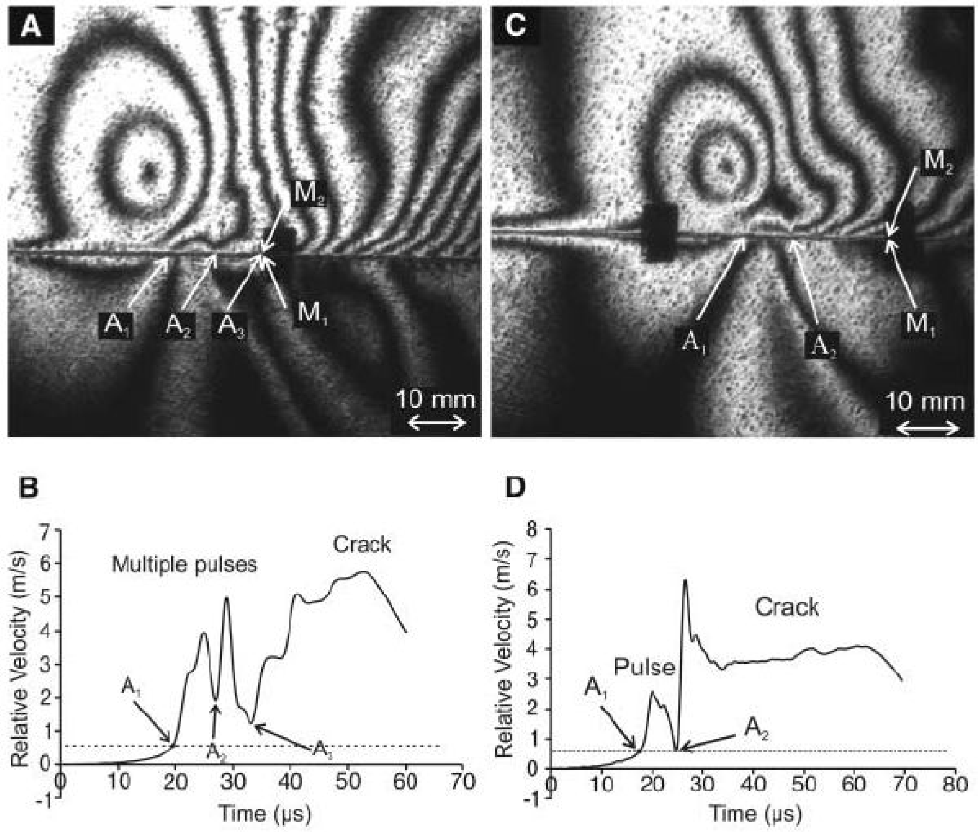

Figure 5.14: **(A) Isochromatic fringe pattern generated during an experiment in which the impact speed was 17 m/s and compressive load was 19 MPa. (B) Relative velocity history of points M_1 and M_2 located at a distance of 70 mm from the impact side of the Homalite plates. Two pulses, A_1A_2 and A_2A_3,were formed. The crack-like rupture mode initiated at A3 immediately behind the second pulse. (C) Isochromatic fringe pattern generated during an experiment in which the impact speed was 13 m/s. (D) Relative velocity history of points M_1 and M_2 located at a distance of 30 mm from the impact side of the Homalite plates. A self healing pulse A_1A_2 was formed. The crack-like rupture mode initiated at A_2 immediately behind the second pulse. (Lykotrafitis et al. 2006)**

The numerical and experimental results exhibit a variety of common features including single and multiple pulses leading with a trailing crack-like sliding mode. It is important to note that the experimental results are plotted with respect to time at a fixed point along the interface while the numerical results shown previously are plotted with respect to distance along the interface at a fixed time. In order to compare the two types of results qualitatively, the experimental result figures should have the time axis inverted. In the experimental results the pulses are leading just as they are in the numerical results with the crack-like sliding mode following.

Thirty times were chosen in the middle of the simulation to show some specific traits of each sliding mode. These times were chosen to be 30 μs to 59 μs because most of the runs included typical results for the entire sliding mode type. The front pulse shape and peak velocity for each of these times can be seen for the transitional crack-pulse mode in Figure 5.15:

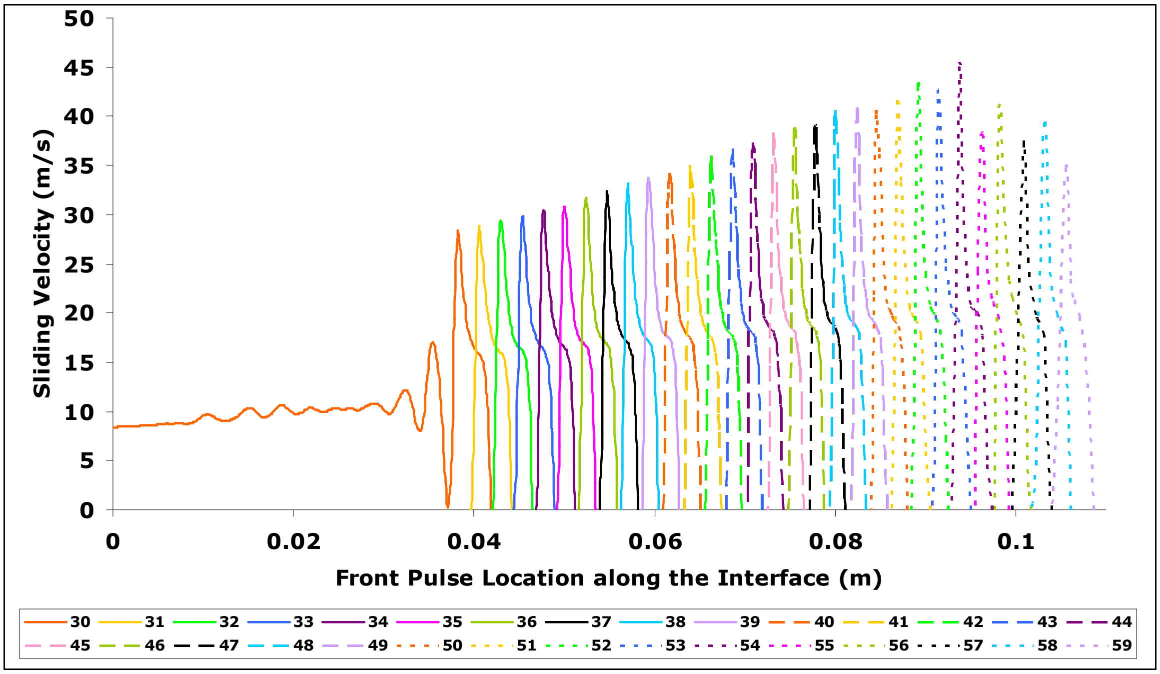

Figure 5.15: Sliding Velocity vs. Front Pulse Location for Crack-Pulse Transitional Mode

At 30 μs, it can be seen that an initial leading pulse had not actually been established yet and it still mostly in a crack-like state. However, one microsecond later, the front pulse is established and separates itself from the crack-like mode. As time increases, the sliding velocity peak for these front pulses also steadily increases until approximately 55 μs where the peak velocity is approximately 45 m/s. After this time the peaks begin to drop off but still fall between 35 m/s and 40 m/s.

Another interesting trend to take note of in Figure 5.15 is the base of each pulse. The following figure shows a line drawn onto Figure 5.15 that signifies where the base pulse approximately ends and the peak of the pulse begins to rise from:

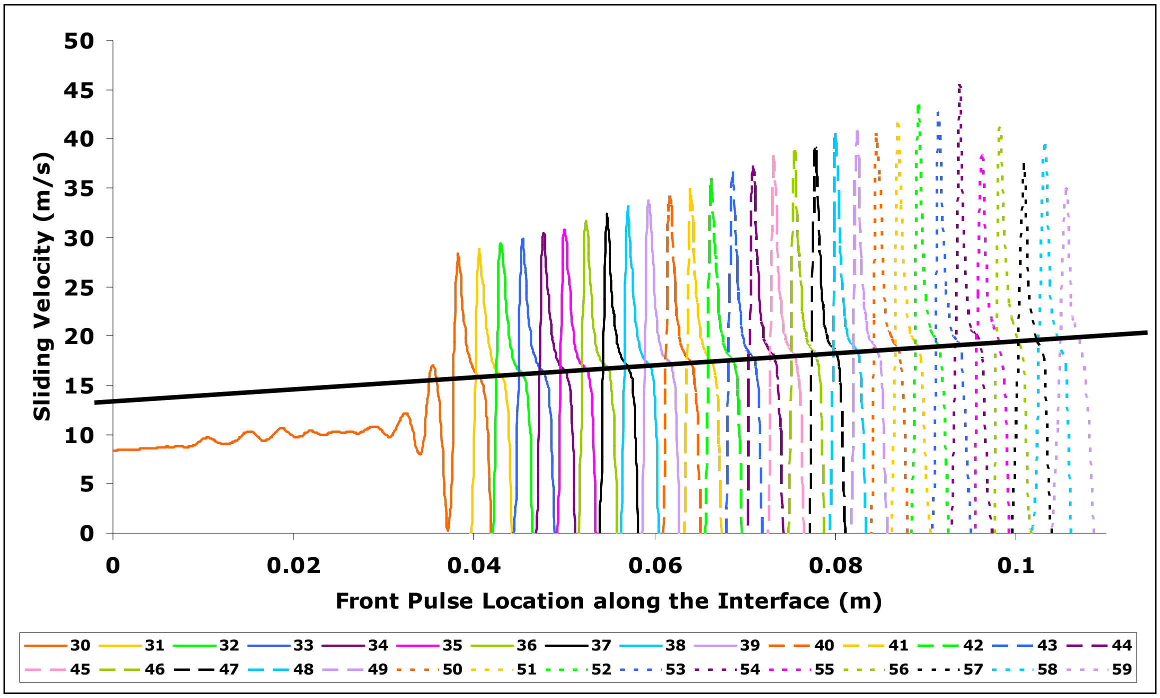

Figure 5.16: Pulse Base for Figure 5.15

The dark line shown in Figure 5.16 is cutting the pulses at the point where the base begins to slope up into the peak of the pulse. For the transitional mode above, the pulse bases range from a "height" of sliding velocity of 16 m/s to 20 m/s. Also, these pulse bases have initial widths ranging from 0.00379 meters to 0.00467 meters and have been plotted in the following figure:

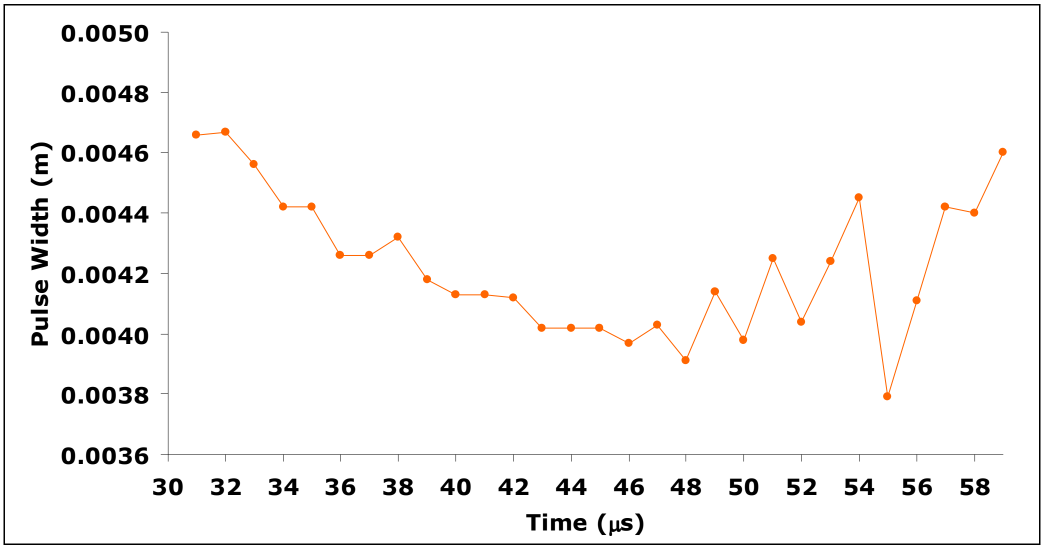

Figure 5.17: Pulse Width vs. Time for 10 MPa 04 m/s

The pulse widths shown above do not include the width at 30 μs since that was not actually a pulse. The pulse widths are all very consistent and close to one another in distance—the maximum and minimum widths are both within one millimeter of each other.

5.1.4. Pulse-Train Transitional Mode

Sliding velocity and stress plots for this pulse-train transitional sliding mode are shown in the following plots of Figure 5.18:

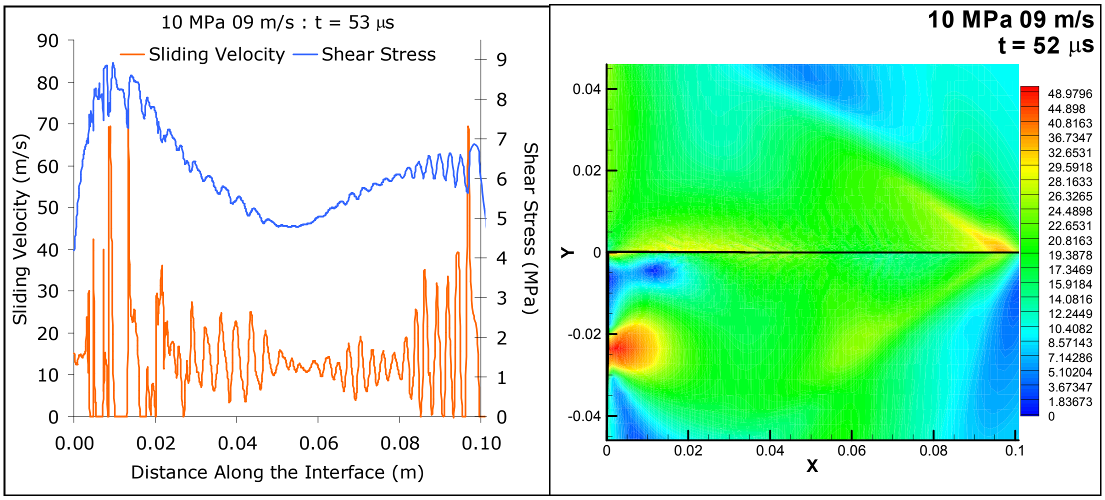

Figure 5.18: Pulse-Train Transitional Mode Sliding Velocity and Stress Plots

The pulse-train transitional mode is a continuation of the previous crack-pulse transitional mode. What separates the two modes is that there is not a trailing crack-like mode in the rear but instead there are pulses beginning to emerge. Also, the mid-section (between the leading pulses and trailing pulses) is pulsating although what keeps this mode as a transitional one is the fact that the mid-section never reaches a velocity of zero to form actual pulses. Figure 5.19 shows the data points for the sliding velocity and shear stress plot of Figure 5.18.

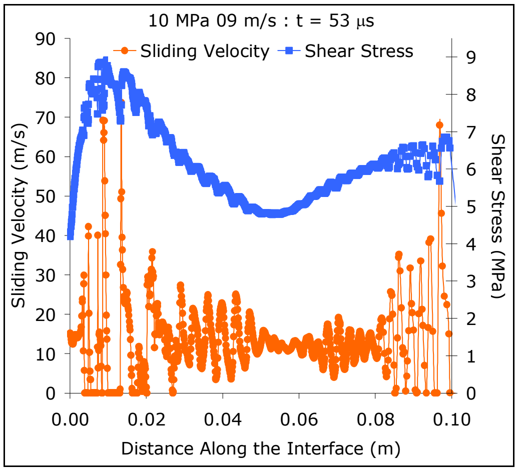

Figure 5.19: Transitional Pulse-Train Sliding Velocity and Shear Stress Data Points

The data points shown in Figure 5.19 demonstrate that there were sufficient data collected within the fine mesh to be accurate. Below is a plot of the normal traction.

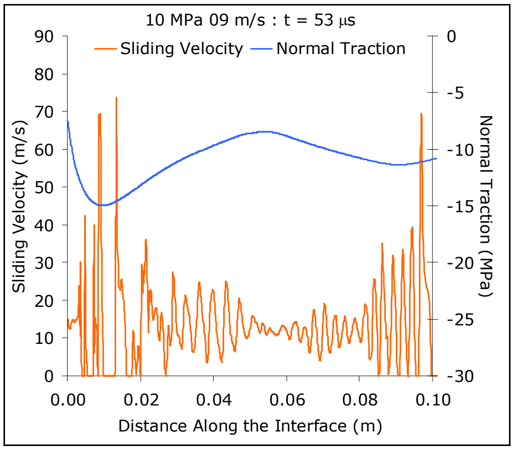

Figure 5.20: Transitional Pulse-Train Sliding Mode Normal Traction with Sliding Velocity plotted against the distance along the interface

The normal traction increases slightly in magnitude just prior to the trailing pulses but does not deviate very much from -10 MPa for the leading pulses. As observed also in previous cases, the gradual variation of the normal tractions along the interface (which is due to dynamic loading waves) is not a factor in the dynamic friction mode characteristics.

The front pulse sliding velocity is plotted below against the position along the interface in Figure 5.21.

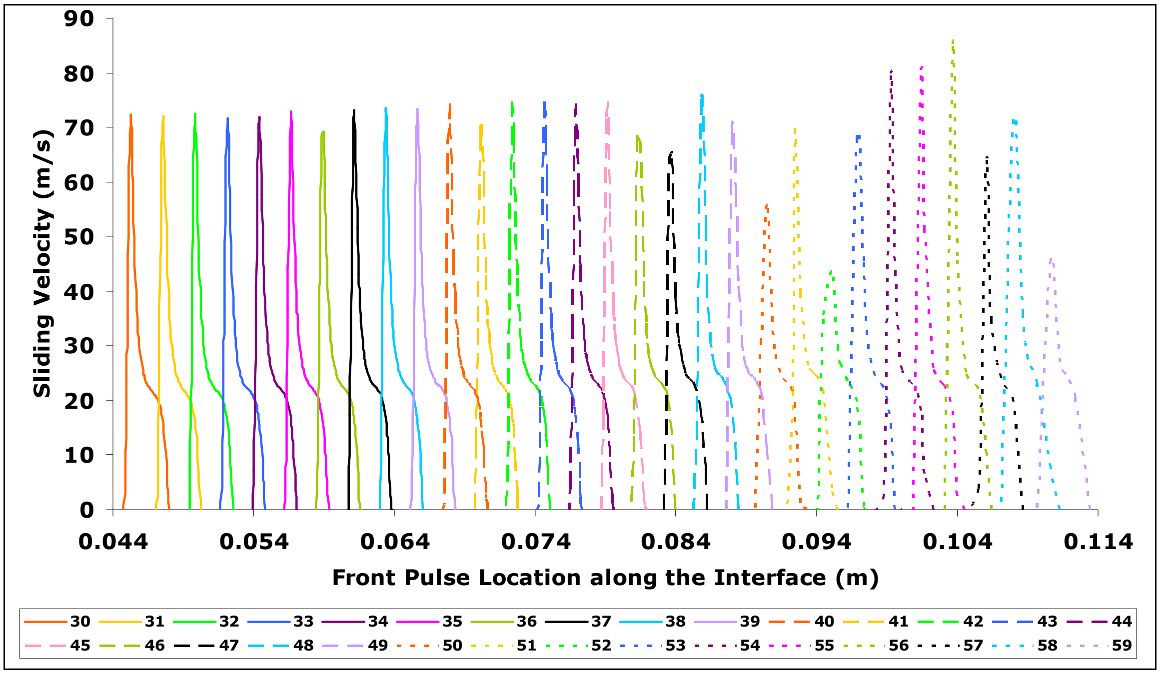

Figure 5.21: Sliding Velocity vs. Front Pulse Location for Pulse-Train Transitional Mode

The peak velocities of these leading pulses hold a somewhat steady peak around 72 m/s although the maximum peak velocity occurs at 56 μs for a velocity of nearly 85 m/s. The pulse bases are also a good measuring tool as shown below in the following figure.

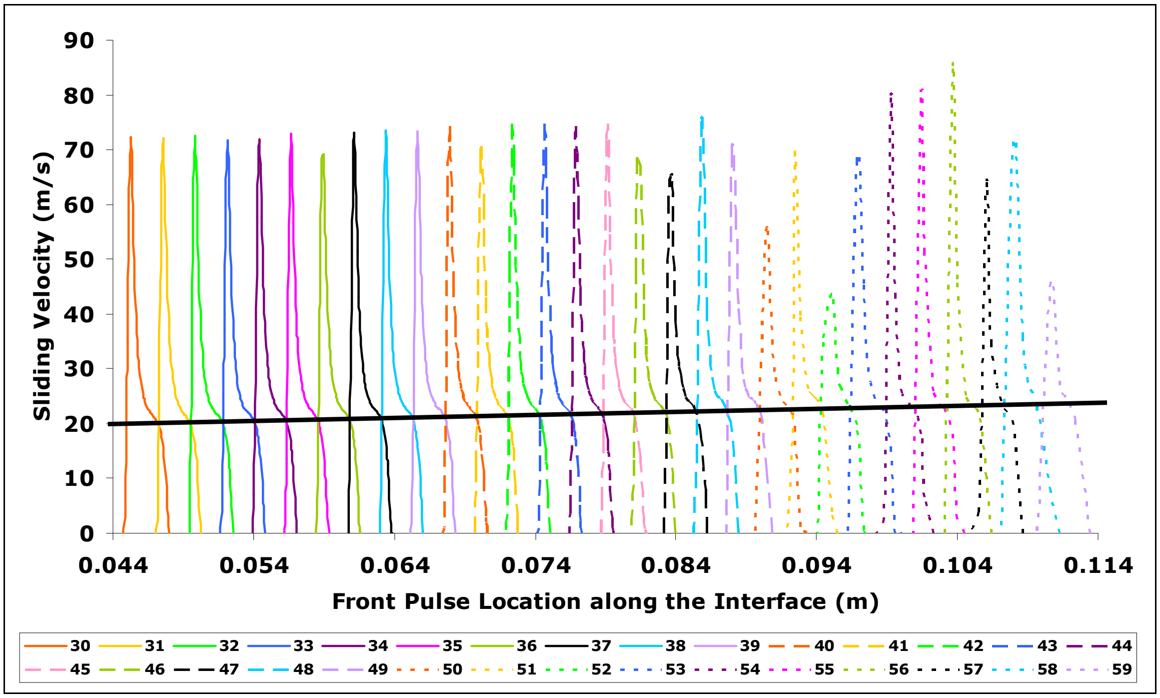

Figure 5.22: Pulse Base for Figure 5.21

The pulse bases range from a sliding velocity of 20 m/s to approximately 24 m/s. These base pulses are around 4 m/s greater than the bases for the crack-pulse transitional mode that was discussed in the previous sub-section. The actual base widths can be seen plotted according to their times of occurrence in the following figure:

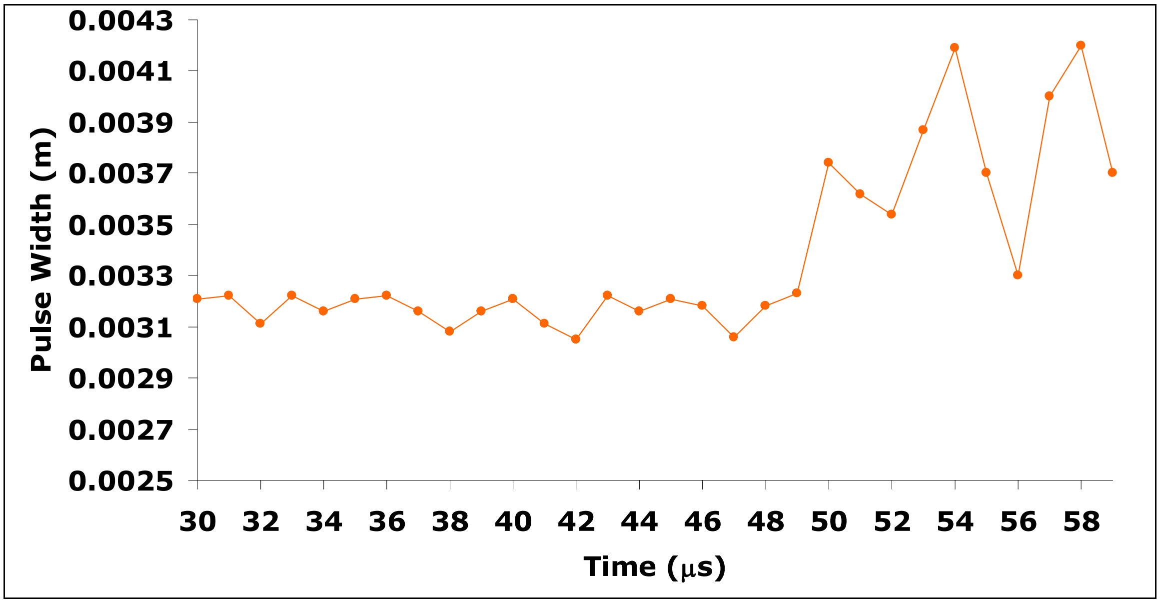

Figure 5.23: Pulse Width vs. Time for 10 MPa 09 m/s Leading Pulse

The base widths vary from 0.00305 meters to 0.00420 meters. These widths are all within approximately one millimeter of each other and therefore are consistent. Another good measuring tool is to compare all of the pulses as shown in the following figure:

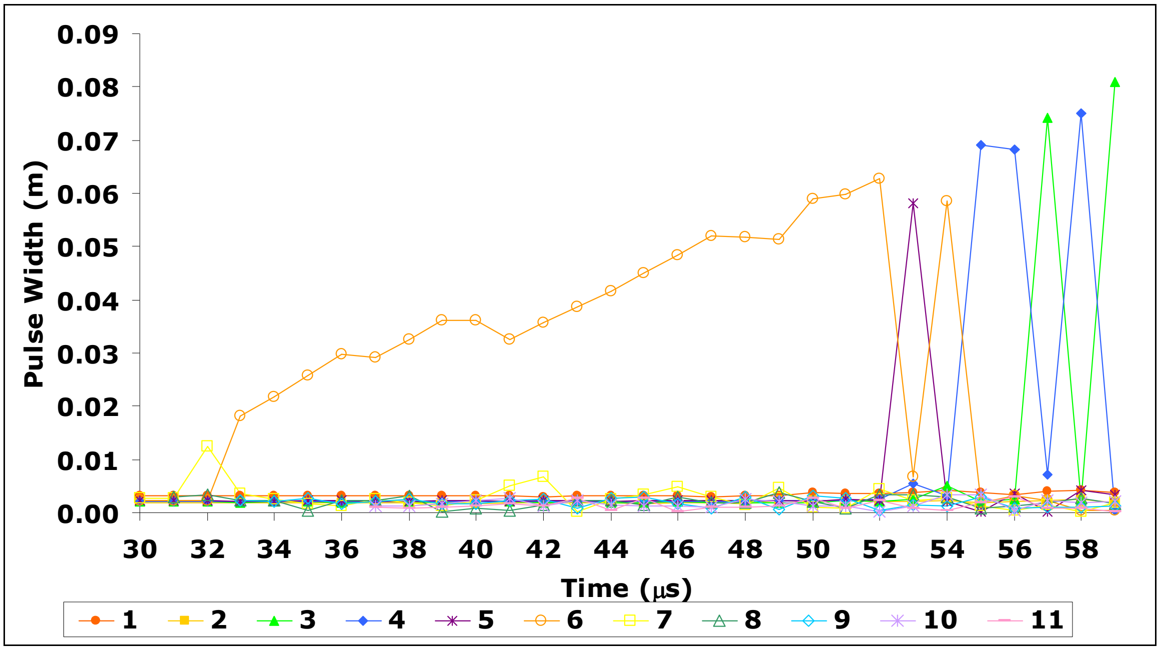

Figure 5.24: Pulse Width vs. Time for 10 MPa 09 m/s

First, it is important to note that the key at the bottom of the figure is denoting the pulse number where '1' denotes the front or leading pulse. Note that the majority of the pulses are fairly constant towards the bottom of the plot. The pulses that have widths jumping up above the line at the bottom are pulses ranging from number 3 through 6 and also pulse 7 jumps up a little. Recall that for this type of transitional mode the midsection of the sliding velocity plot was referred to as pulsating and fluctuating trying to come to zero. This plot shows this same trend with the middle pulses. It is also important to see that the front pack of pulses is nearly the same in base width as the trailing pack of pulses.

5.1.5. Train of Pulses Mode

The train of pulses mode sliding velocity and stress modes are shown in the following figures:

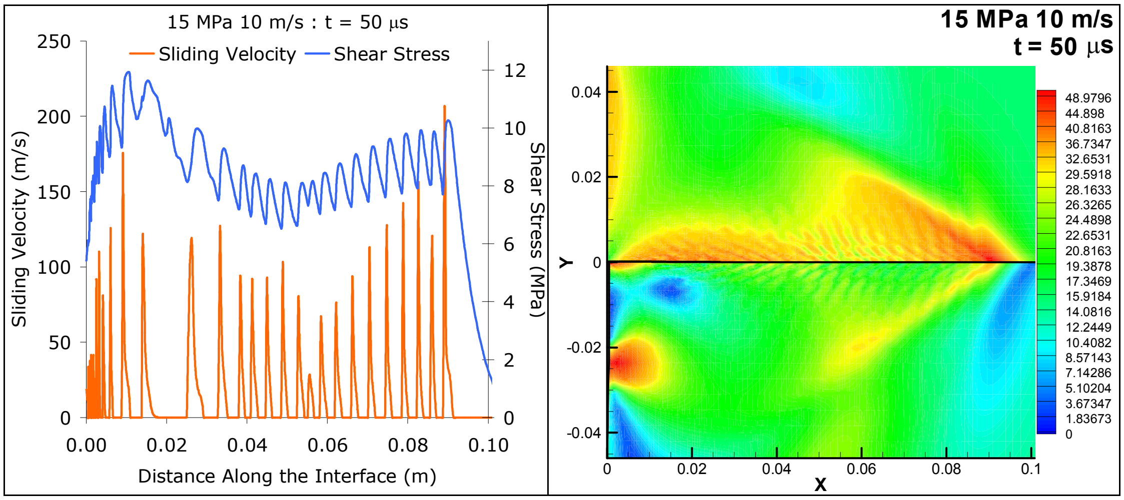

Figure 5.25: **Train of Pulses Mode Sliding Velocity and Stress Plots**

The train of pulses includes many pulses each reaching a zero velocity and then with a slight pause, another well-defined pulse emerges, somewhat reminiscent of a train of pulses. The magnitude of the sliding velocity peaks on these pulses is nearly one order of magnitude greater than the previous pulse transitional modes. The data points for the sliding velocity and shear stress plot on the left of Figure 5.25 are shown below in the following figure.

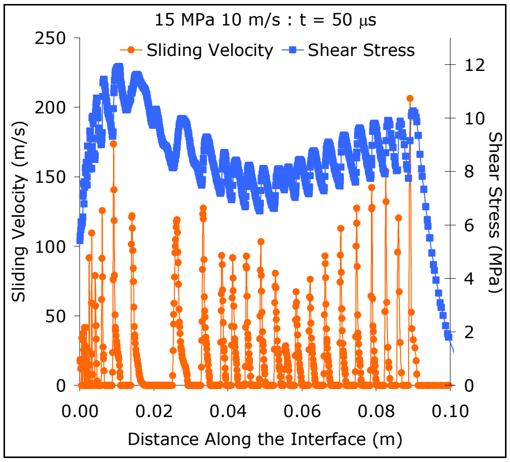

Figure 5.26: Train of Pulses Mode Sliding Velocity and Shear Stress Data Points

The figure above shows that the mesh is sufficiently fine and therefore, the data is independent of the mesh. Another interesting characteristic of Figure 5.26 is the shear stress relation to the sliding velocity. Figure 5.27 below zooms in on the leading pulses to show that correlation.

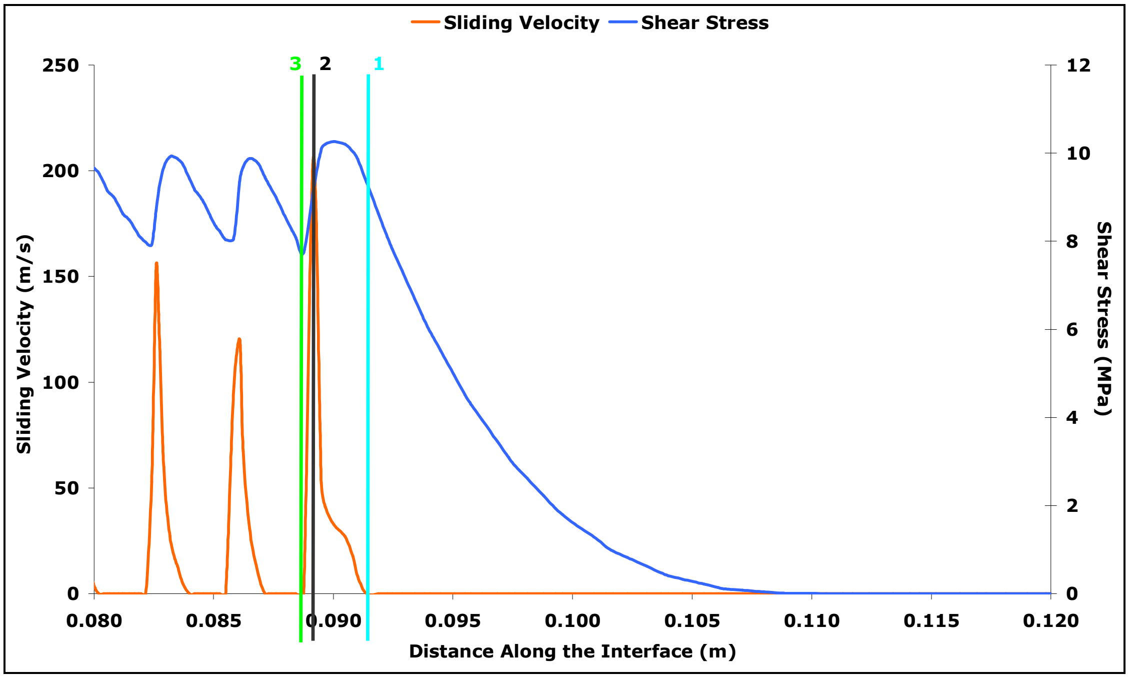

Figure 5.27: Sliding Velocity Pulse Correlation to Shear Stress Plot

As can be seen from Figure 5.27 there are three vertical lines drawn at significant locations of the leading pulse. Line 1 denote the beginning of the pulse and occurs just before the peak of the shear stress plot. This shows that the two Homalite plates are sticking together while the shear stress is building up and just before the sliding velocity pulse begins the plates begin to slip. This sliding velocity pulse peaks just after the shear stress peak as can be seen from Line 2. So just after the shear stress reaches a local maximum, the Homalite plates reach a slip velocity maximum and then begin to slow down rapidly. The shear stress continues to decrease until it reaches a local minimum at

Line 3. This local minimum corresponds to the sticking location of the sliding velocity pulse. At this point, the plates stick again and stop sliding relative to each other.

The normal tractions are plotted against the interfacial distance along with the sliding velocity in Figure 5.28 below.

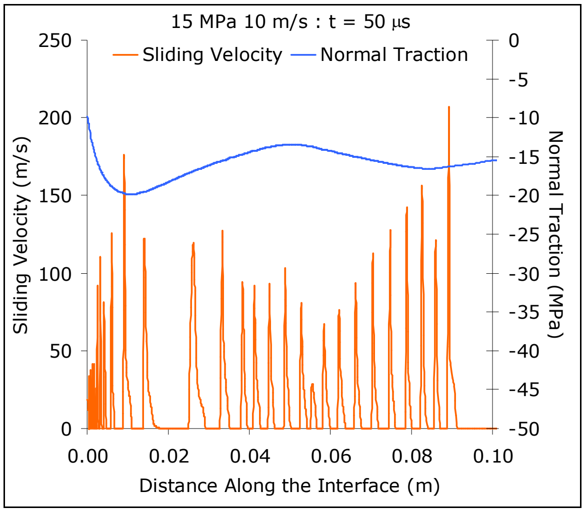

Figure 5.28: Train of Pulses Normal Traction with Sliding Velocity plotted against the interfacial distance

In Figure 5.28 there is not a significant change in the normal tractions along the interface as was also the case in each of the previous sliding modes—including that of the crack-like mode shown in Figure 5.5. Thus, it should be concluded that since there is not a significant jump in the normal traction for each pulse observed that the normal traction along the interface is not a factor in the dynamic frictional sliding characteristics.

A plot of the leading pulses for the times between 30 µs and 59 µs are plotted in Figure 5.29.

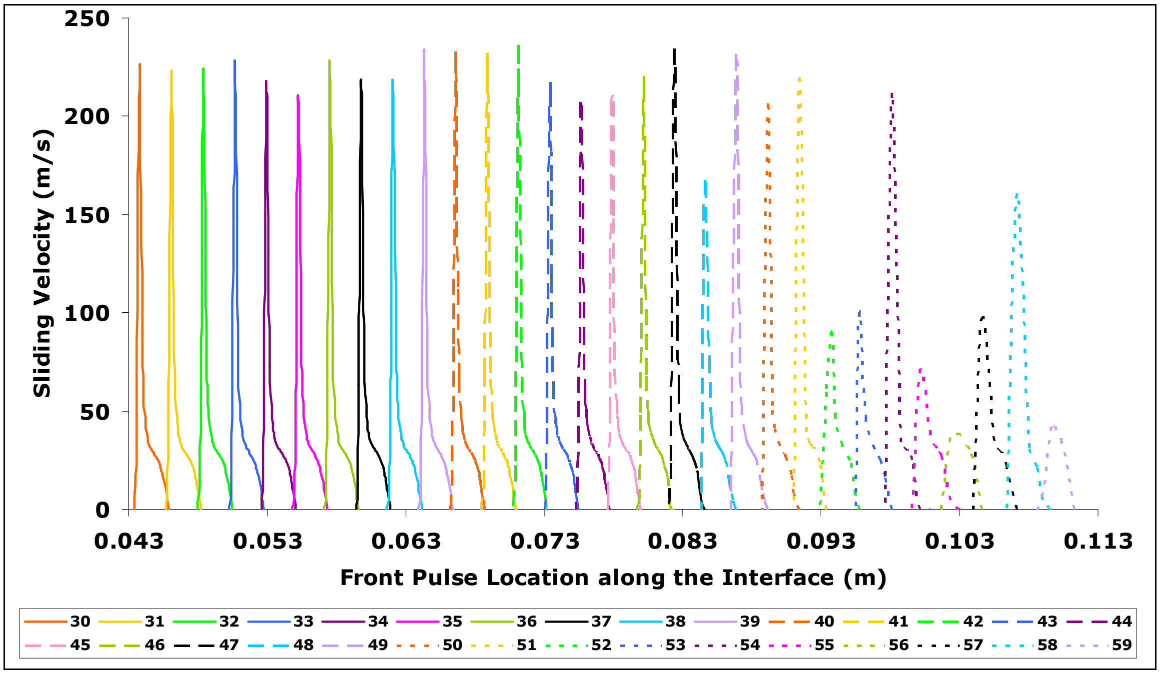

Figure 5.29: Sliding Velocity vs. Front Pulse Location for Train of Pulses Mode

The majority of the sliding velocity peaks fall around 225 m/s until a time of 42 μs where the peaks begin to drop off. The following figure shows the pulse base comparisons.

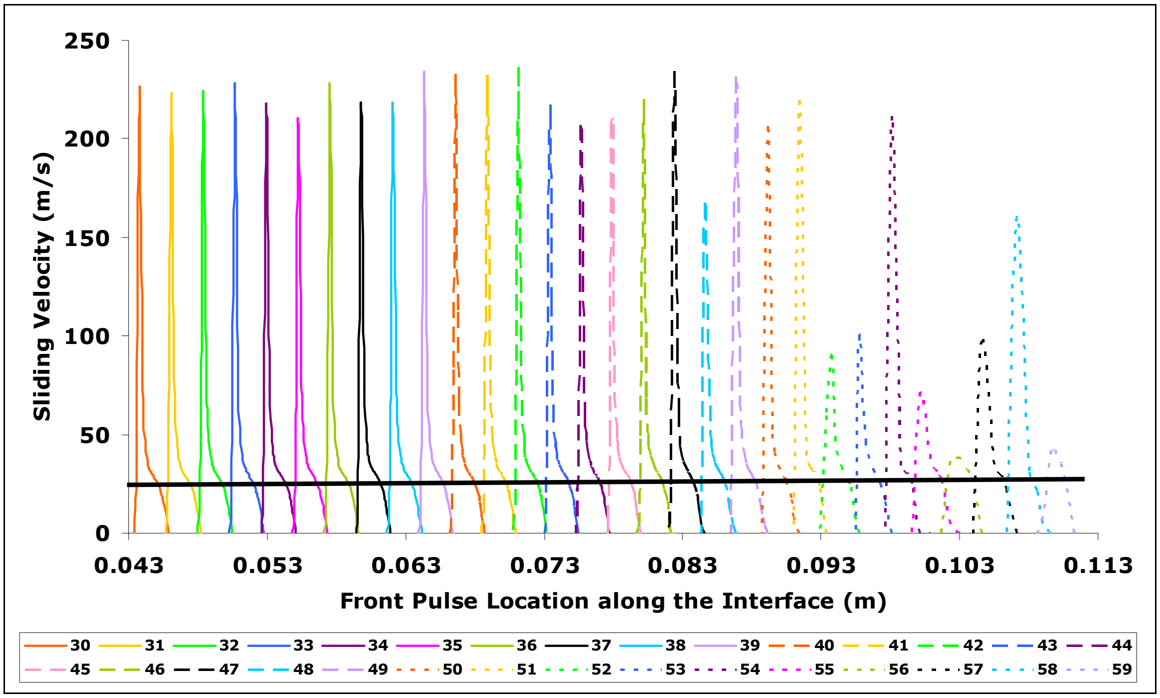

Figure 5.30: Base Pulse for Figure 5.29

The dark line represents the approximate locations of the sliding velocities that occur as the base of the pulse narrows to begin formulating the peak of the pulse. In this case, the base "heights" range from approximately 25 m/s to 30 m/s. The base widths should also be analyzed and plotted for the front pulses as shown below.

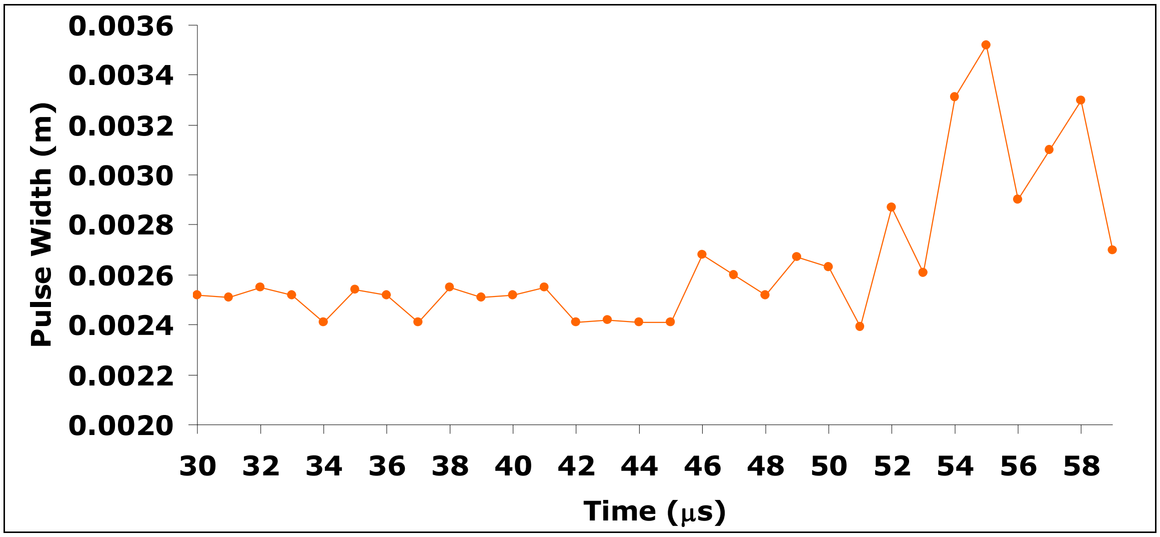

Figure 5.31: Leading Pulse Width vs. Time for 15 MPa 10 m/s

The pulse widths shown above vary from a minimum value of 0.00239 meters and a maximum value of 0.00352 meters. As in the previous sliding modes, the pulse widths are fairly consistent, the range staying within a millimeter between each leading pulse. Figure 5.32 shows the pulse widths for the leading pulse and the pulses that follow.

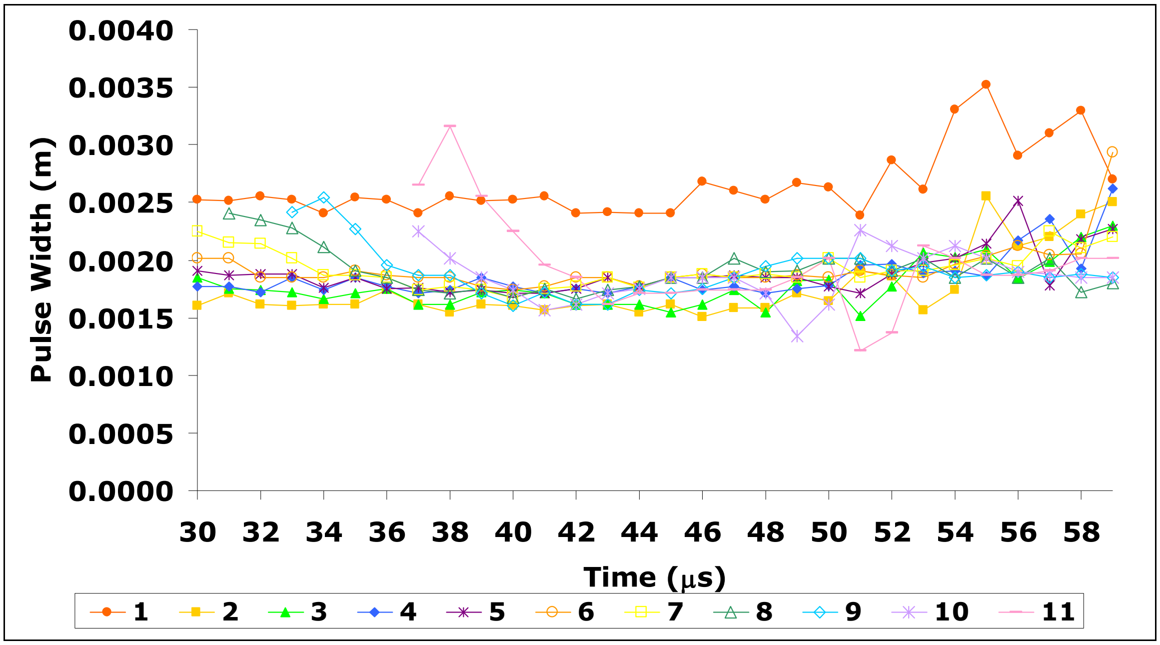

Figure 5.32: Pulse Width vs. Time for 15 MPa 10 m/s

Figure 5.32 shows that the leading pulses, in general, have the widest bases but for the pulses that follow, the pulse widths tend to maintain a pulse width between 0.0015 meters and 0.0020 m. Some pulses have a wider base but not many. This is important as it shows that the leading pulse is distinct and somewhat different from the trailing pulses. The leading pulse also tends to have the greatest peak sliding velocity.

One further interesting trait that should be mentioned for this case is the distance between the maturing pulses. This has not been a relevant study for the previous cases because the pulses were not as constant down the line (or towards the impact zone on the interface). The following figure shows the distance between pulses plotted against the times that range again from 30 μs to 59 μs.

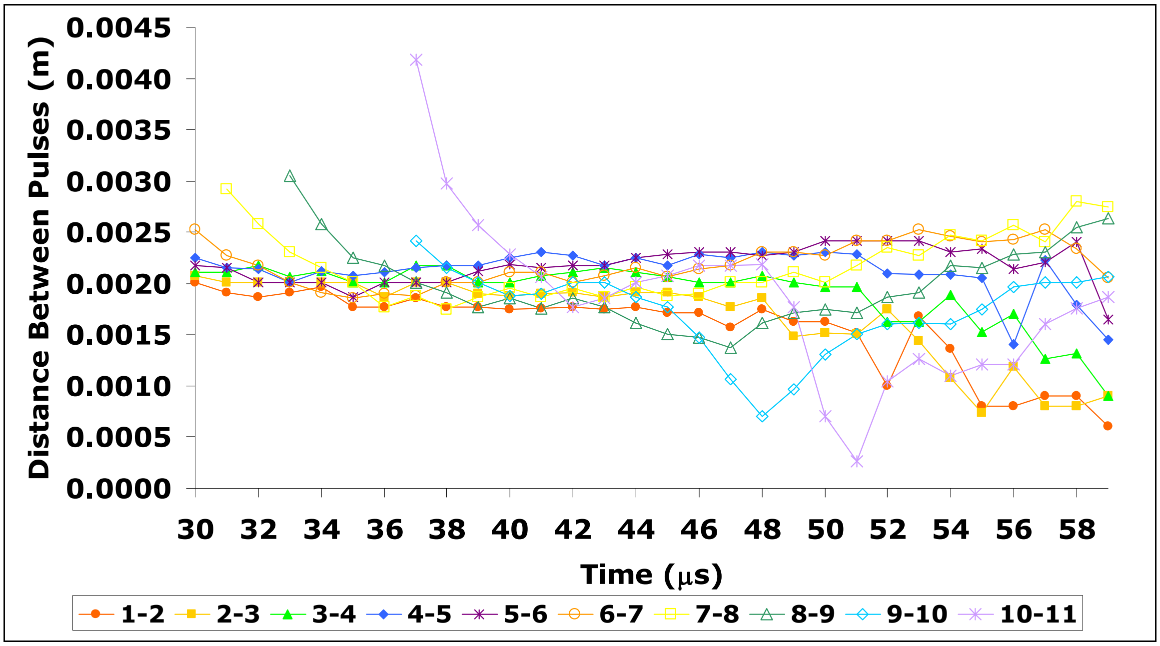

Figure 5.33: Distance between Pulses vs. Time for 15 MPa 10 m/s

The above figure shows that the distances between the pulses are mostly between 1.5 and 2.5 mm. There are some instances where the distance might drop significantly or spike somewhat higher, but these only appear for a couple microseconds and then fall into line with the rest of the data.

5.1.6. Growing Pulses Mode

The growing pulse mode sliding velocity and stress plots are shown below:

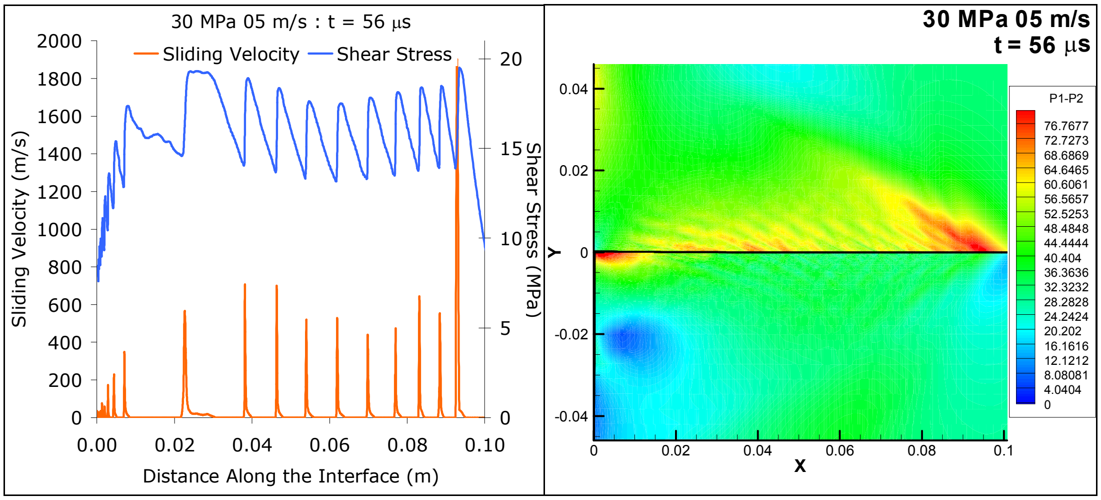

Figure 5.34: **Growing Pulses Mode Sliding Velocity and Stress Plots**

The difference between the pulse train described above and the growing pulses shown here is not only the increase of at least one order of magnitude in the peak velocity but also the distance between pulses.

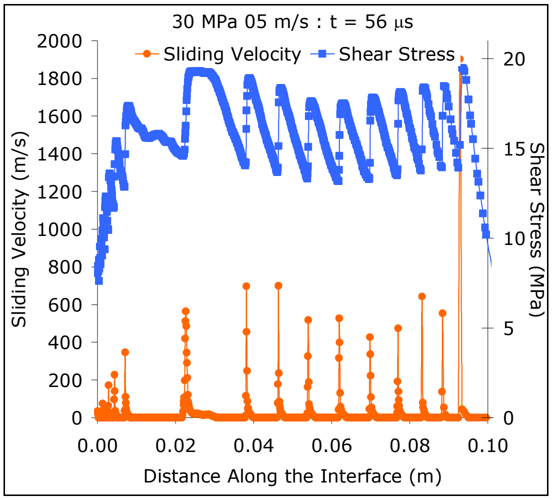

Figure 5.35: Growing Pulses Mode Sliding Velocity and Shear Stress Data Points

The data points in Figure 5.35 show the mesh to be sufficiently fine. This also shows that the data taken is independent of the mesh. The normal traction along the interface is also plotted with the sliding velocity in Figure 5.36.

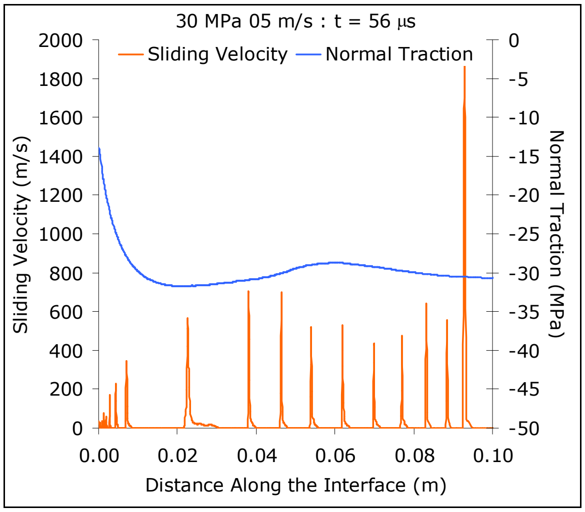

Figure 5.36: Growing Pulses Interfacial Normal Traction with Sliding Velocity plotted against the distance along the interface

Figure 5.36 further illustrates that the interfacial normal traction is not affecting the frictional sliding event by causing slip-pulses.

An investigation of the leading pulse was also conducted for this sliding mode and is plotted in the following figure.

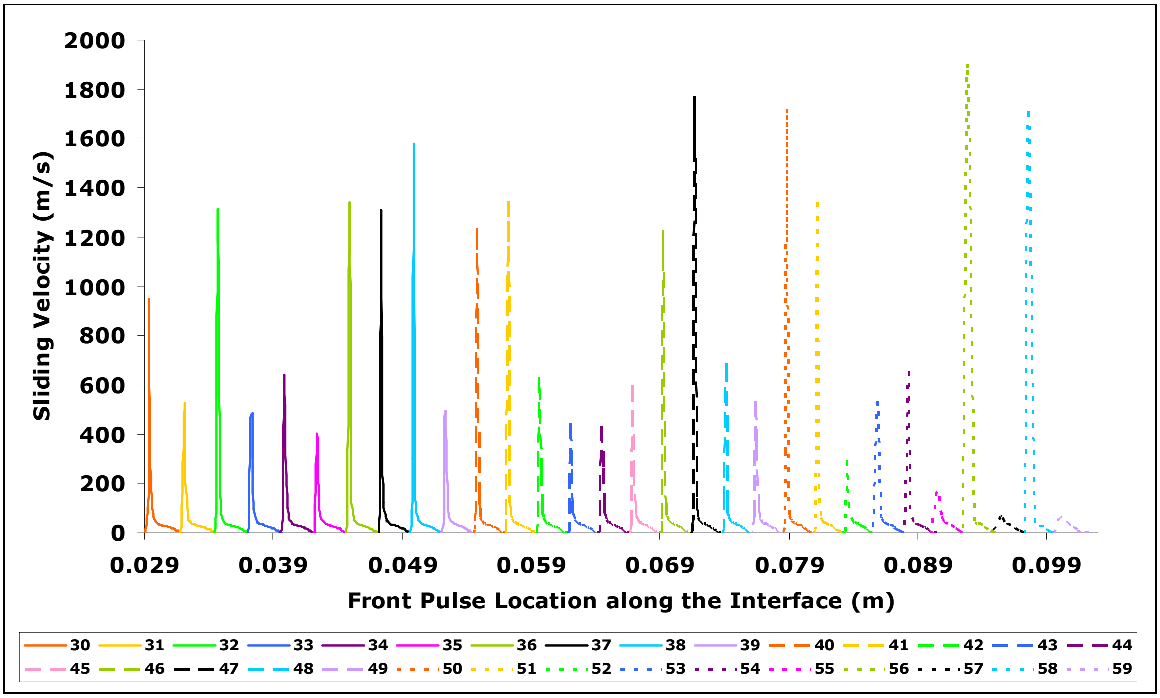

Figure 5.37: Sliding Velocity vs. Front Pulse Location for Growing Pulses Mode

Here it is interesting at how much the peak velocity fluctuates. With the growing pulses sliding mode the front pulse tends to spike at a high sliding velocity and then drop down, still to a velocity that is higher than the previous sliding modes, and rebuild only to spike again in a short amount of time (only a few microseconds). As in previous cases, the base of the pulse remains to be around 30 μs. The next case to investigate is the width of the pulses. The front pulse base widths are plotted against time in Figure 5.38.

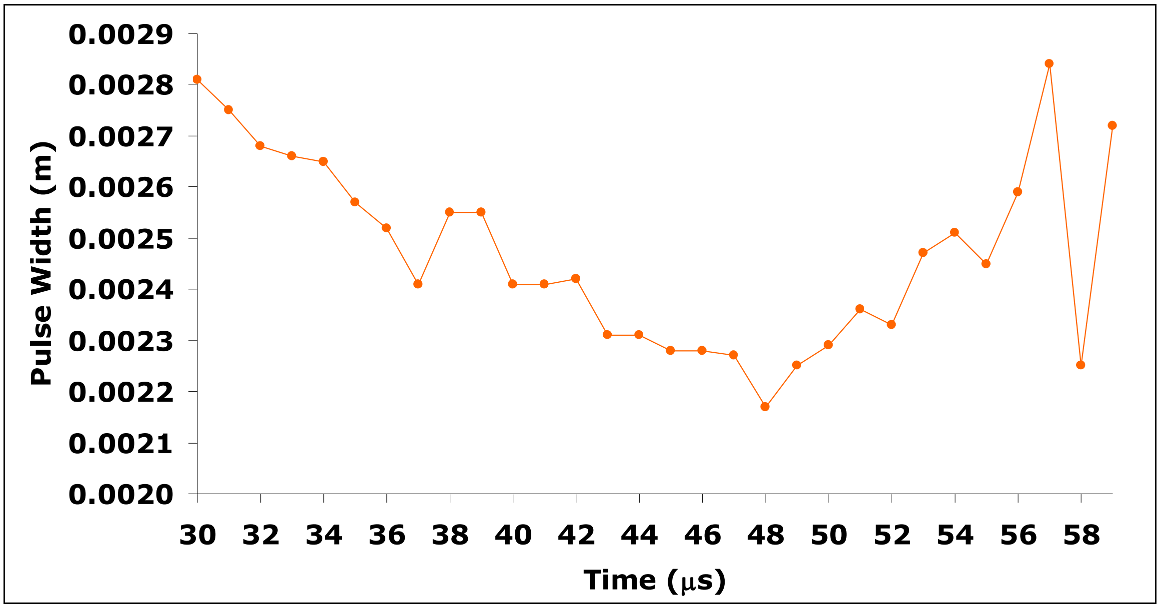

Figure 5.38: Leading Pulse Width vs. Time for 30 MPa 05 m/s

As can be seen above, the pulse widths are all within one millimeter of each other as time increases. The minimum pulse width is 0.00217 meters and the maximum width is 0.00284 meters. The figure below shows the pulse widths plotted against time for the leading pulse along with the pulses that follow.

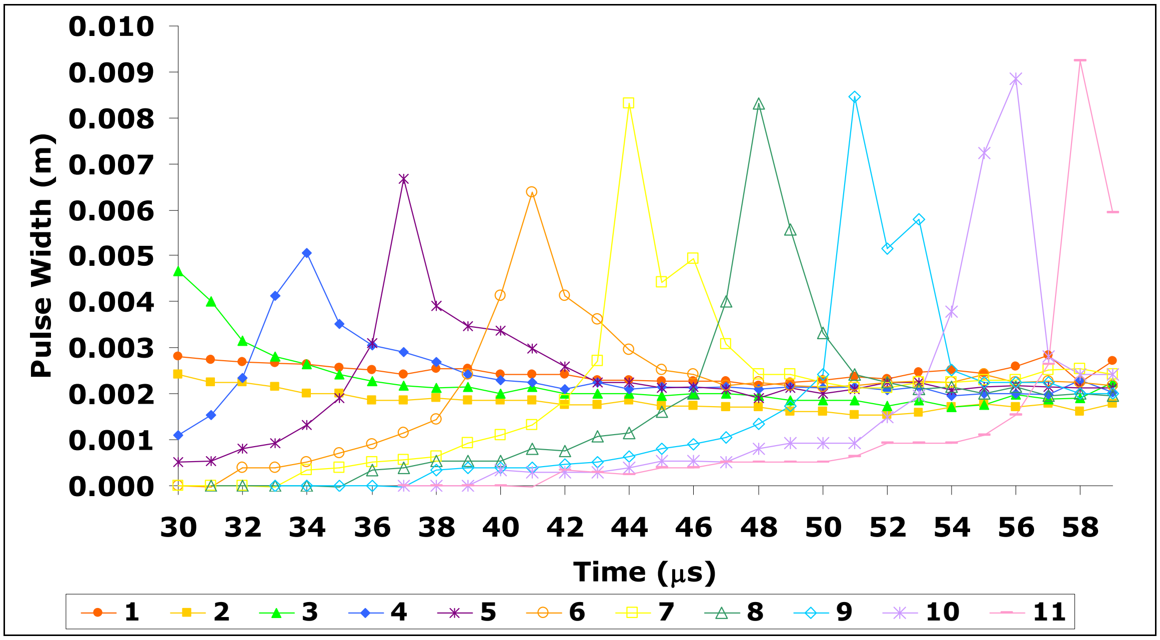

Figure 5.39: Pulse Width vs. Time for 30 MPa 10 m/s

There are a couple of interesting features of Figure 5.39. One is that the first two pulses are nearly constant. The following pulses all seem to hold a very distinct pattern which begins with a very small width between pulses in which the general trend as the widths increase has a positive concavity and then the width begins to decrease quickly at first at a decreasing rate and then the widths level off to the same "line" as the previous pulses.

Another trait that should be discussed is the distance between pulses. This is really only an issue for the train of pulses and the growing pulses sliding modes because these are the only modes that have mature and consistent pulses. The following figure shows the distance between pulses for the growing pulse mode plotted against time:

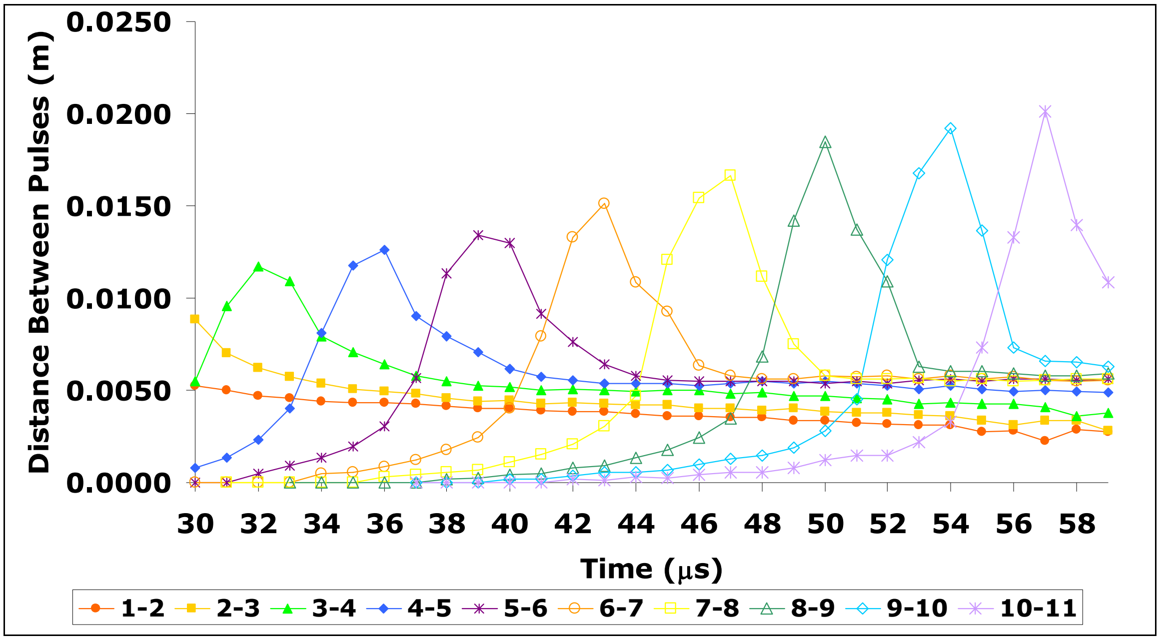

Figure 5.40: Distance between Pulses vs. Time for 30 MPa 05 m/s

This plot also shows a general trend that is followed by every pulse. The key indicates the distance between the appropriate numbered pulses (i.e. 1-2 would show the distance between the first and second pulse). These pulses hold a constant distance of approximately 5 millimeters between the first two pulses where the following pulses can be nearly 20 millimeters apart from one another.

5.1.7. Phase Overviews and Comparisons

Now that a foundation has been set for each of the observed sliding modes, it is important to actually compare them and describe some of the important differences that separate one mode from another. First, recall that the train of pulses mode and the growing pulses mode are the two modes with the most mature pulses. But what actually separates the two modes? For one thing, the actual sliding velocity peak on the leading pulse is generally larger for the growing pulses mode than for the train of pulses.

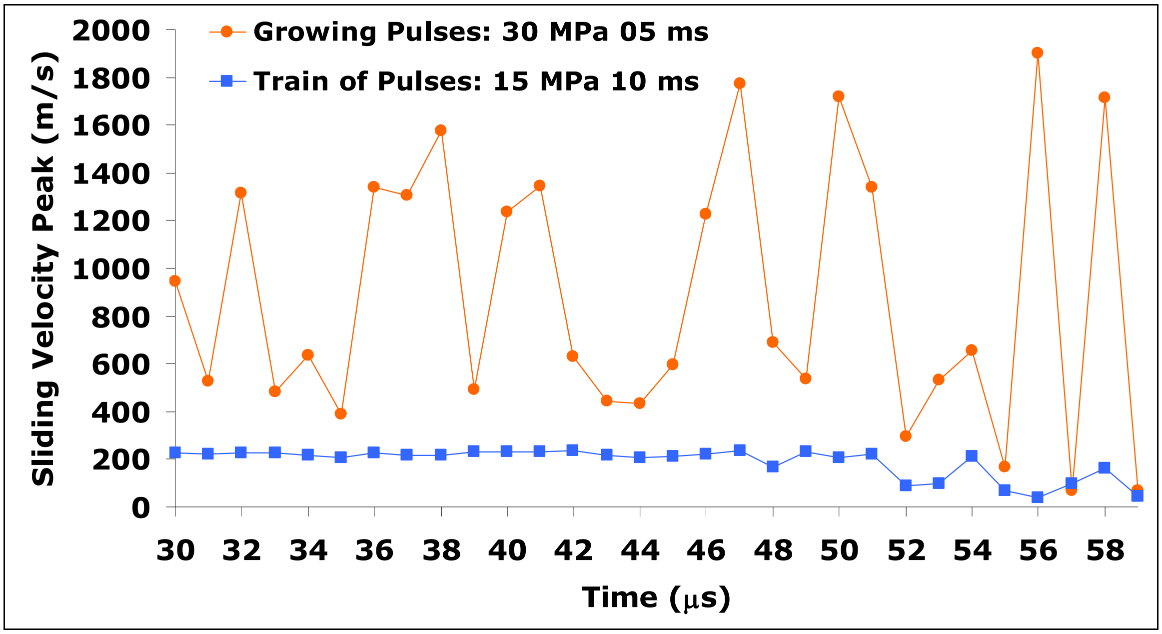

Figure 5.41: Leading Pulse Sliding Velocity Comparison for Growing Pulses vs. Train of Pulses

From the figure shown above, it is evident that the sliding velocities for the leading pulses of the growing pulses mode is above the train of pulses mode for nearly every time displayed. Another interesting note to make is that it seems that some time after 50 μs the trends begin to break down a little. The growing pulses however holds onto its rebuilding or growing stage from time segment to time segment, dropping down to around 400 m/s and then shooting back up to nearly 2000 m/s, while the train of pulses holds somewhat steady around 200 m/s. Another comparison that should be noted is that of the pulse widths shown below:

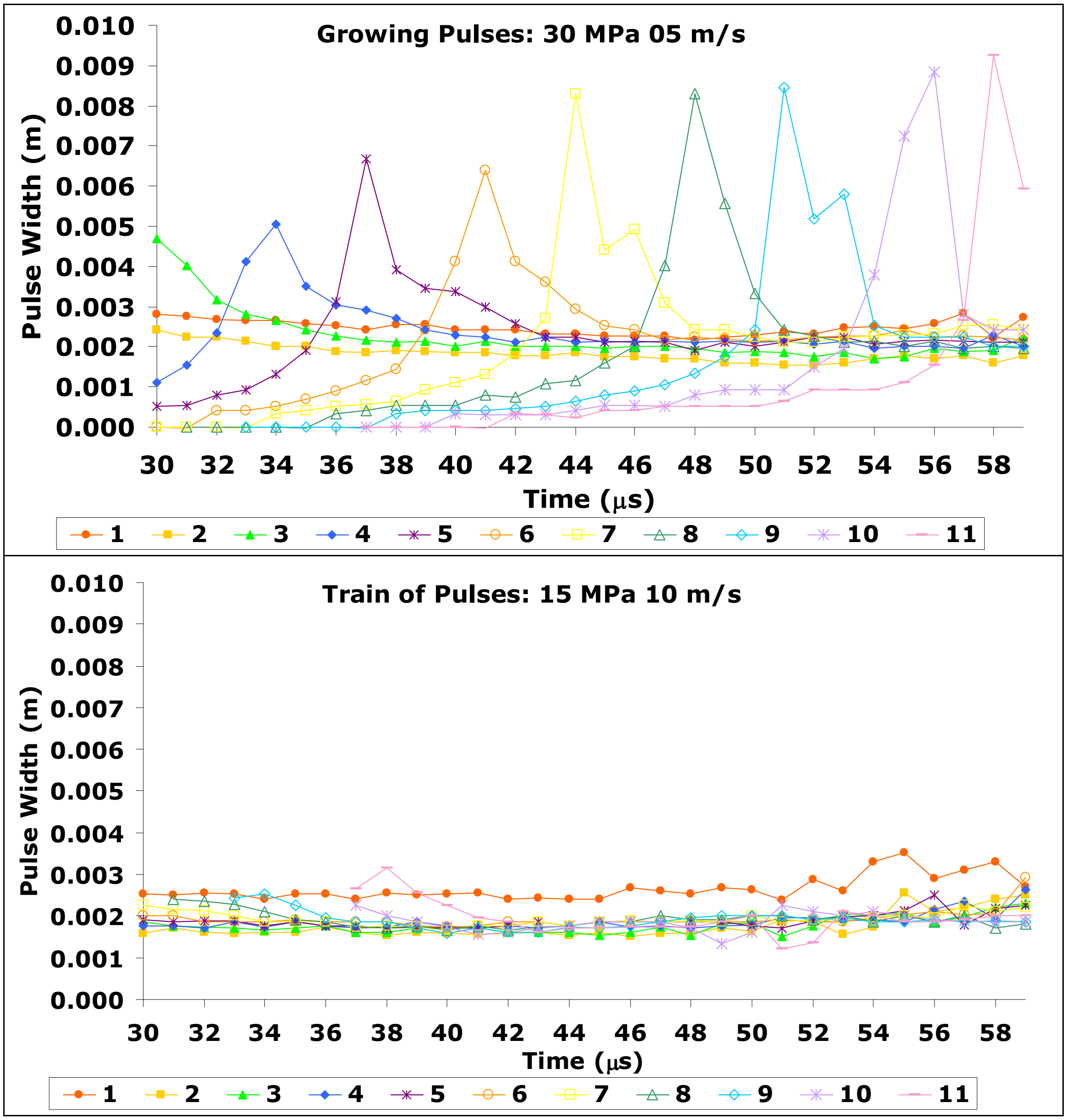

Figure 5.42: Pulse Width Comparison for Growing Pulses vs. Train of Pulses

The plots shown in Figure 5.42 were placed in the same viewing window dimensions to show the actual trend comparisons. While the front pulses are actually very similar in width for the two modes, the rest of the following pulses tend to be much different. The train of pulses pulse widths don't seem to really increase more than 3 millimeters, while the growing pulses can have at least one pulse width up to nearly 9 millimeters at any given time. The last trait to discuss, and perhaps one of the more important traits, is the distance between pulses.

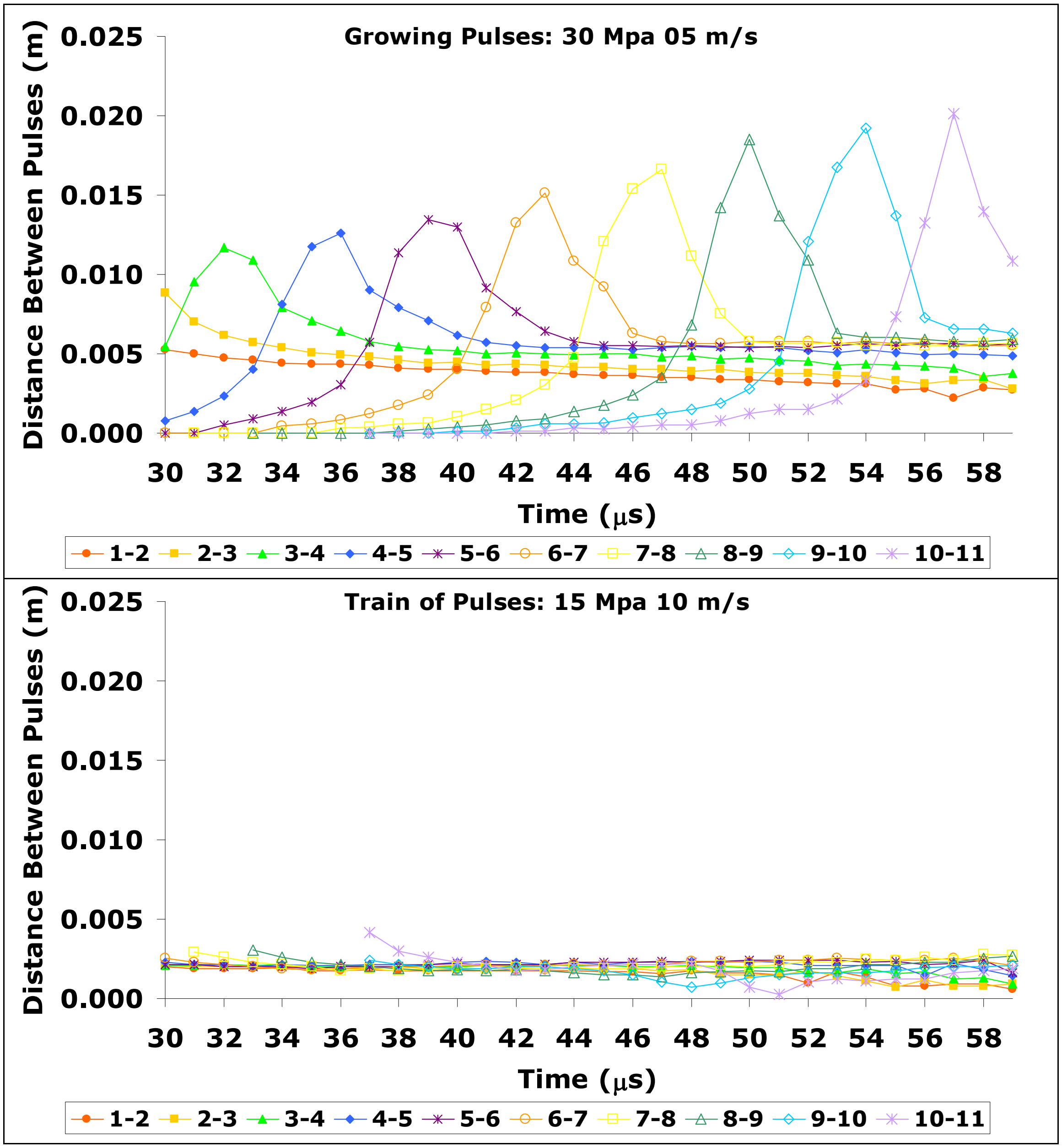

Figure 5.43: Distance between Pulses Comparison for Growing Pulses vs. Train of Pulses

The distance between pulses for the train pulses holds fairly constant at about 2.5 millimeters apart, while the distance between pulses for the growing pulses mode can be up to 20 millimeters apart. One final look at these comparisons can be the sliding velocity plotted against the distance along the interface shown in Figure 5.44 below:

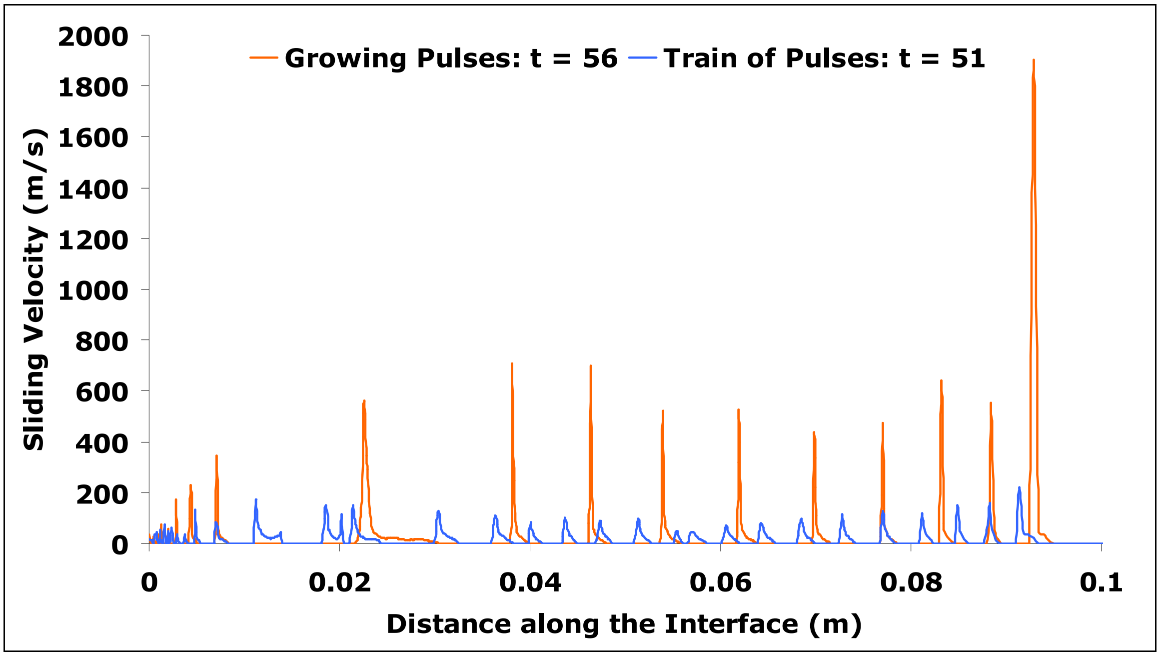

Figure 5.44: Sliding Velocity Plot Comparison for Growing Pulses vs. Train of Pulses

This plot clearly shows that the pulses are significantly larger for the growing pulses mode and the distance between pulses is significantly larger as well. Another interesting look at these two modes is how much more defined the pulses are for the growing pulses mode than for the train of pulses mode.

Next, the transitional modes will be analyzed. Recall that the crack-pulse transitional mode has at least one leading pulse followed by a crack-like sliding in the rear. However, the trailing pulse transitional mode does not lead with a defined pulse but instead starts like a crack-like mode and has pulses trailing the crack-like sliding. The following figure shows the sliding velocity of each of these transitional modes plotted together against the distance along the interface between the two homogenous sliding plates.

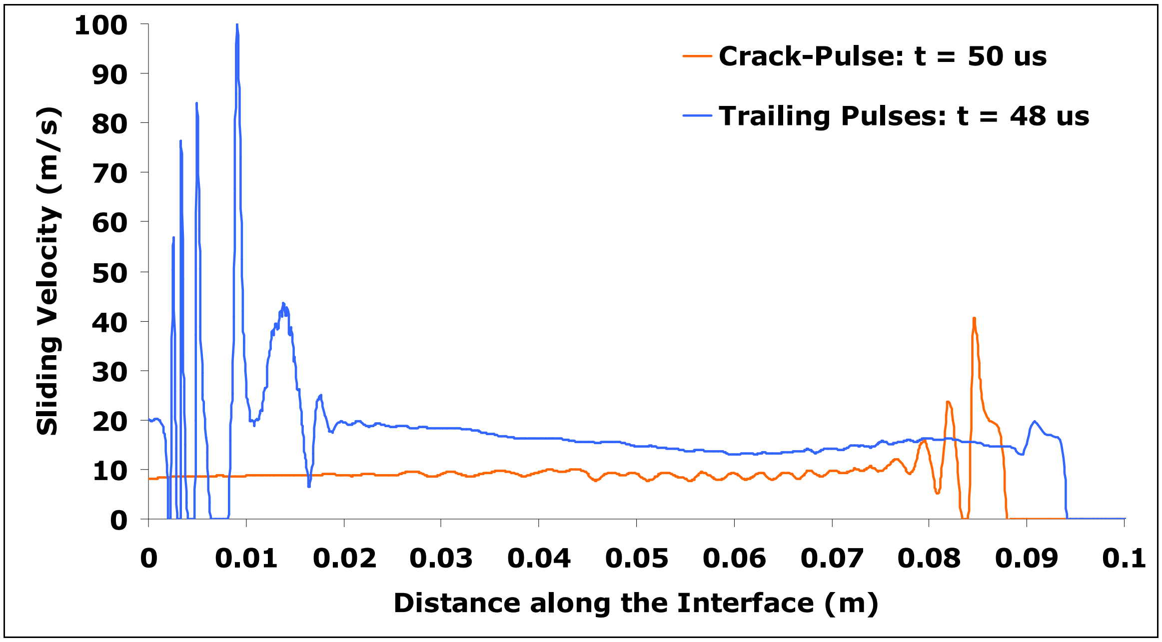

Figure 5.45: Sliding Velocity Plot Comparison for Crack-Pulse vs. Trailing-Pulse Transitional Modes

From the figure above, it can be seen that these two transitional modes, when spliced together, look significantly like the final transitional mode—the pulse-train transitional mode—shown in the figure below:

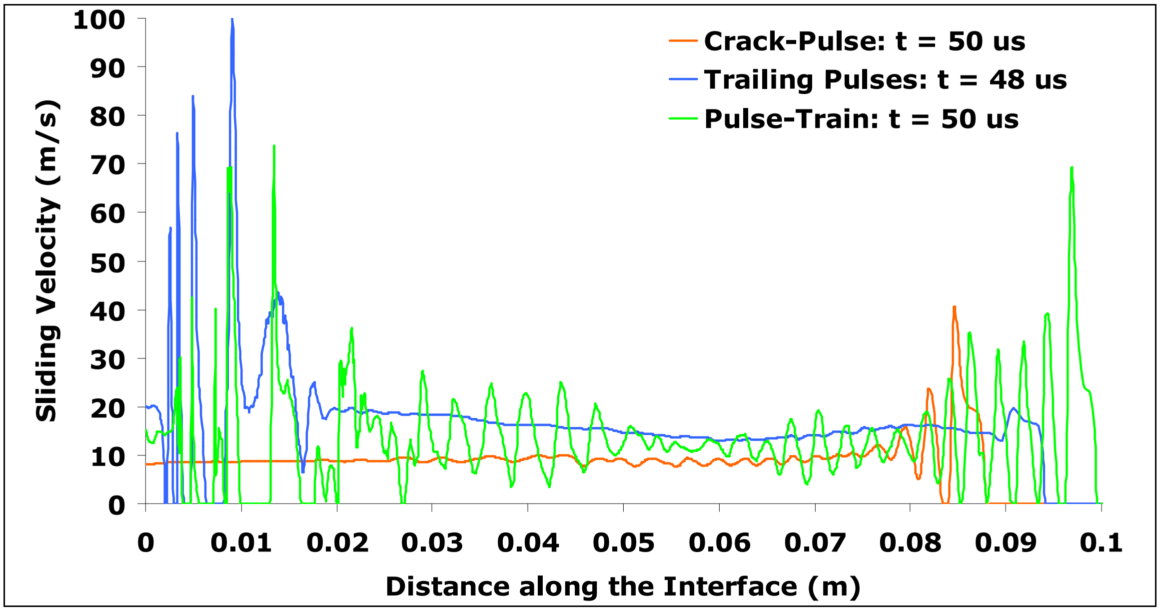

Figure 5.46: Sliding Velocity Plot Comparison for Figure 5.45 vs. Pulse-Train Transitional Mode

From Figure 5.46, the train-pulse mode is a transitional mode that leads into the train of pulses mode but is also a combination of the previous transitional modes.

After discussing the six different sliding modes observed, a sliding modes diagram was created as seen in Figure 5.2. To get a better understanding of what is happening, a blended illustration of this modal diagram was created to see how the transitions might be occurring. However, in order to make this diagram non-material dependent, it has been normalized with the material's Young's modulus and the shear wave speed and can be seen in Figure 5.47.

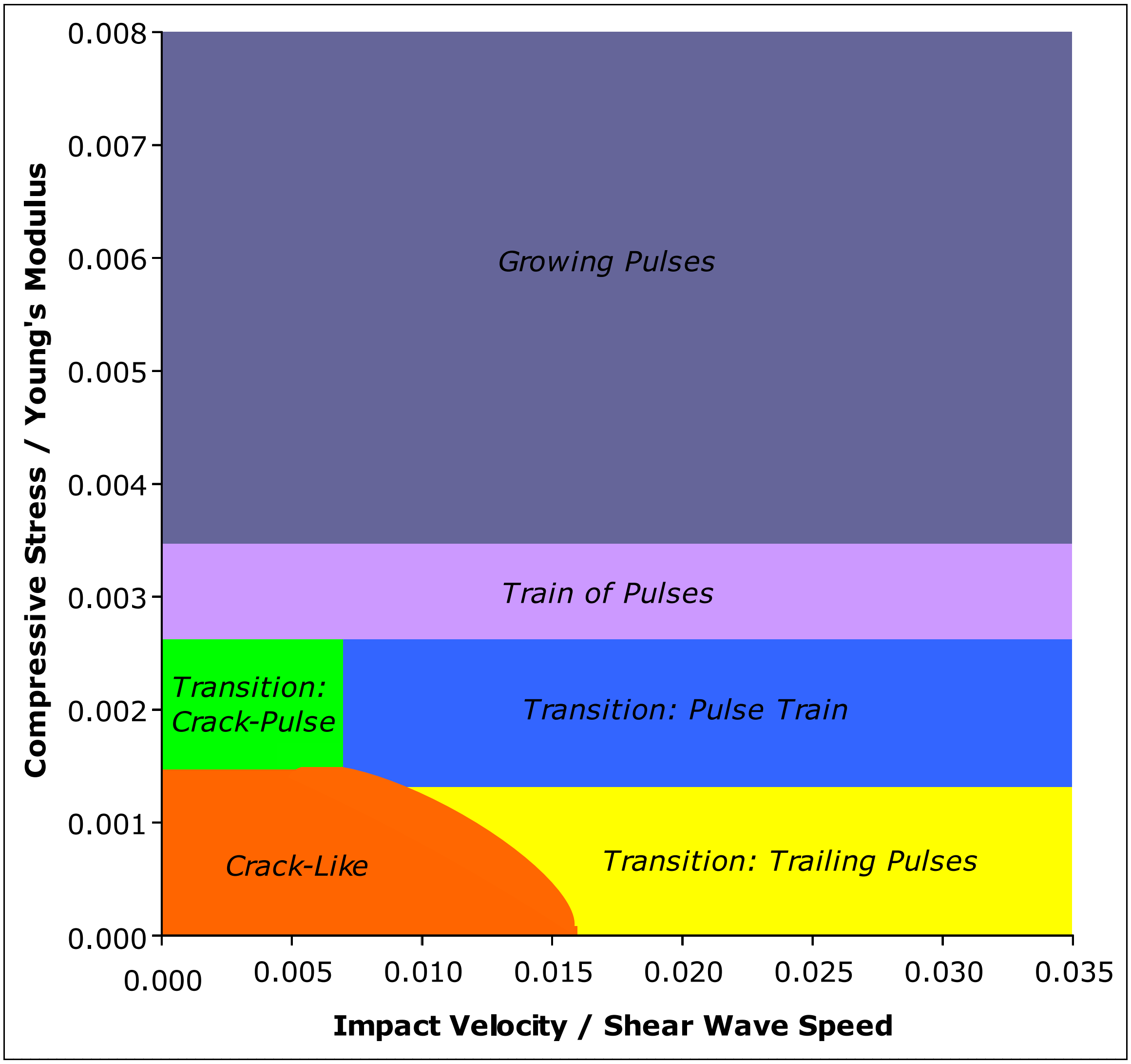

Figure 5.47: **Normalized Blended Sliding Modes Phase Diagram**

Figure 5.2 and Figure 5.47 show some interesting sliding mode trends. Generally as the impact velocity increases, trailing pulses emerge and mature. For example, looking at a low compressive stress $\left(\frac{\sigma_0}{E} \leq 0.0015\right)$ the sliding would begin as a simple crack-like sliding and as the impact velocity increases, the crack-like sliding will begin to transition into a pulse-like mode with some trailing pulses. However, holding the impact velocity constant and varying the compressive stress allows pulses to begin to mature in the lead as the crack tip formulates. For example, looking at a low compressive stress $\left(\frac{\sigma_0}{E} \leq 0.0015\right)$ would show that there is crack-like sliding initially which transitions to a leading pulse with a crack-like trail behind the crack tip. From this crack-pulse transition, the pulses begin to mature everywhere behind the crack tip to form a train of pulses sliding mode.

Recall the similarities between the three transitional modes. It was previously stated that the pulse-train transitional mode looked like the crack-pulse transitional mode and the trailing pulse transitional modes put together. Looking at the phase diagrams, it can be seen why this is so. The trailing pulses begin around an impact velocity of $\frac{V_{imp}}{c_s} > 0.016$, while the leading pulses begin to emerge for an intermediate compressive stress $\left(\frac{\sigma_0}{E} > 0.0015\right)$. As the compressive stress continues to increase, the pulses begin to increase in magnitude and separate their distance from one another.

5.2. Openings

The stick-slip sliding occurring along the interface brings up some questions as to what is actually going on. When the interface between the two Homalite plate meshes was zoomed in on, it was found that an opening was actually occurring as shown in Figure 5.48 for the crack-like case of 1 MPa 1 m/s.

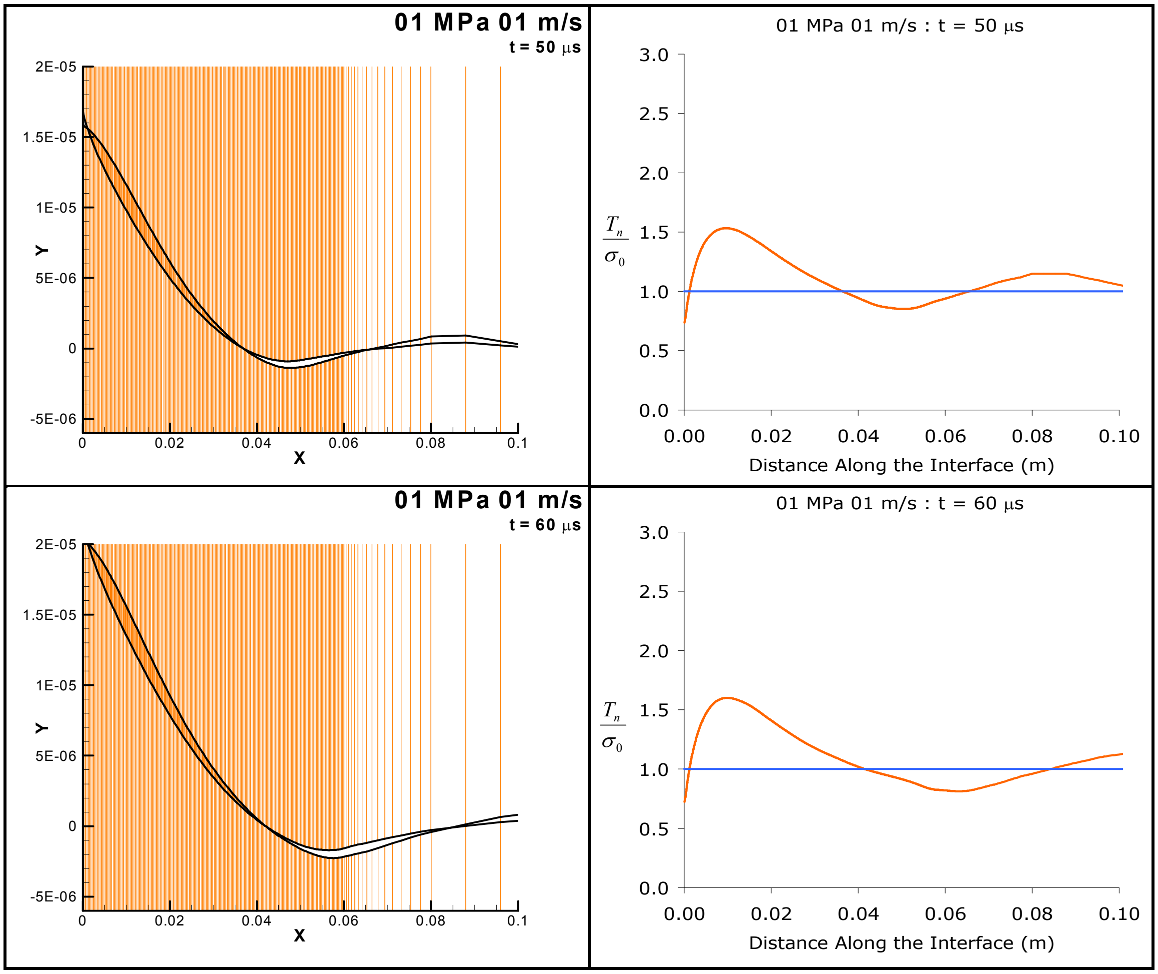

Figure 5.48: Mesh Opening for 01 MPa 01 m/s (left) and the Ratio of Interfacial Normal Traction to Applied Compressive Load vs. Distance Along the Interface (right) at t = 50 μs (top) and t = 60 μs (bottom)

In the mesh opening figures on the left of Figure 5.48, a white region can be seen between the x-locations of 0.04 meters and 0.08 meters. These areas are the separation of the two plates along the interface. The normal tractions occurring along the interface have been normalized with the applied compressive load and are plotted in the figures on the right of Figure 5.49. There is separation occurring between the two plates along the interface when the ratio of the normal traction to the applied compressive load drops below one. Therefore, it can be inferred that when the interfacial normal tractions drop below the applied compressive load that there will be separation occurring along the interface between the two plates. This occurs not only for the crack-like case but for every numerical simulation studied in this research. Figure 5.49 shows an opening example for the train of pulses example case of 15 MPa 10 m/s:

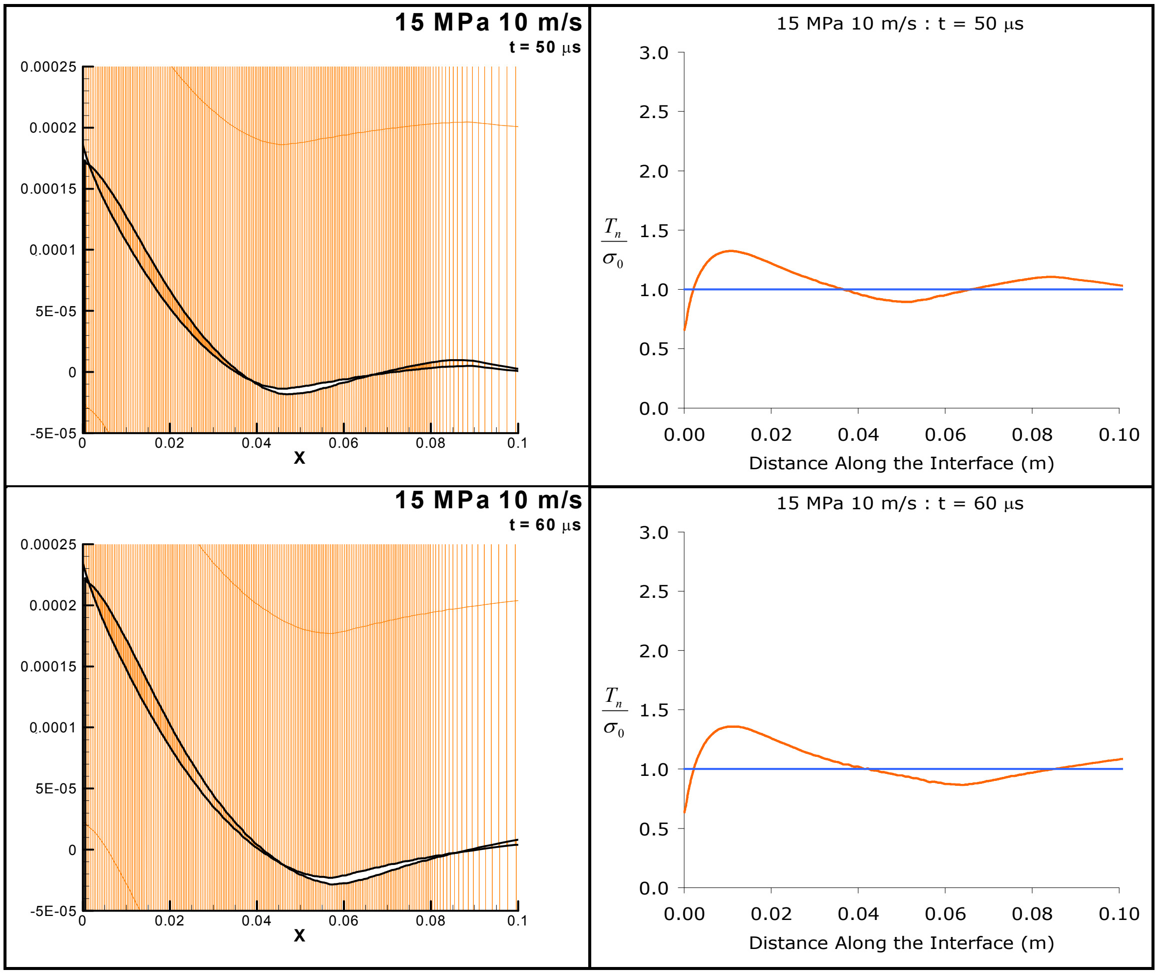

Figure 5.49: Mesh Opening for 15 MPa 10 m/s (left) and the Ratio of Interfacial Normal Traction to Applied Compressive Load vs. Distance Along the Interface (right) at t = 50 μs (top) and at t = 60 μs (bottom)

Figure 5.49 shows a very similar scenario as the one portrayed by Figure 5.48. The orange region to the left and right of the interface is a slight interpenetration of the two meshes. While these interpenetrations may not actually be happening in reality, the cohesive laws allow for very small interpenetrations to keep numerical stability. This can also be seen in the normalized figures on the right of Figure 5.49. For any normal traction to applied load ratios greater than one, interpenetrations occur. Thus, it can be concluded that when the interfacial normal traction is larger than the applied compressive load, interpenetrations will occur between the two meshes.

The openings waves that have been observed in this research are reminiscent of Schallamach waves that were discovered by closely examining the relationship between rubber and the hard material that it was sliding on. These Schallamach waves are actually openings that occur between the rubber interface with a harder track during the stick-slip frictional events (Schallamach 1971). An opening along a Homalite interface was also found in simulations done using a cohesive law formulation (Coker et al. 2003).

The front locations of the opening waves observed for some numerical simulations are plotted in Figure 5.50.

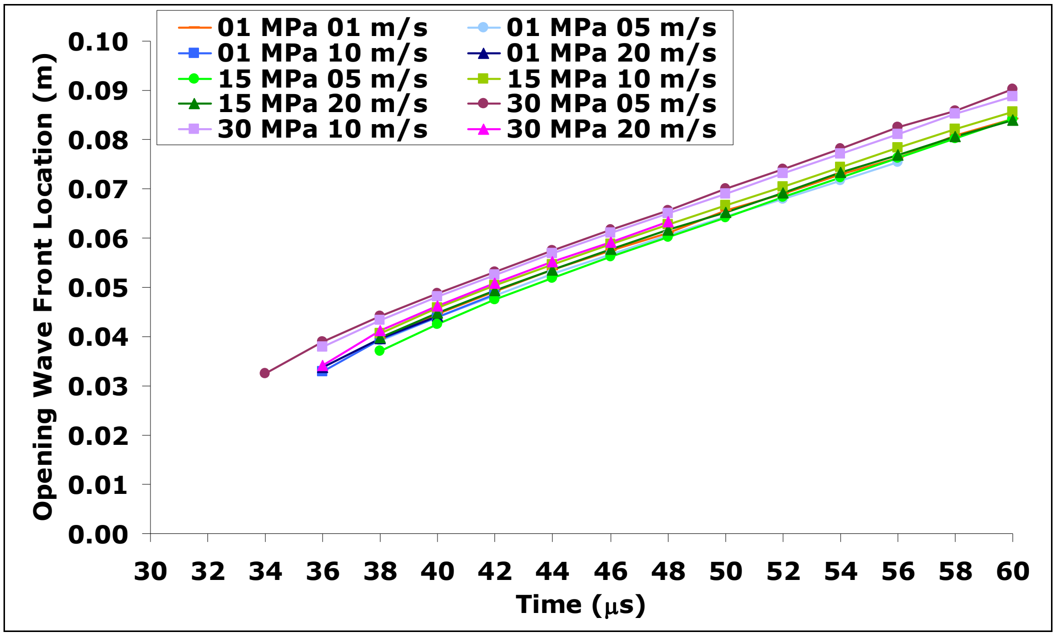

Figure 5.50: Opening Wave Front Locations vs. Time

The opening waves are all very similar in location throughout time. As can be seen, the opening waves usually start between 33 and 36 μs. These opening waves begin at nearly the same location of approximately 0.03 meters regardless of the compressive stress or impact velocity. The following figure plots the length of the opening waves with respect to time.

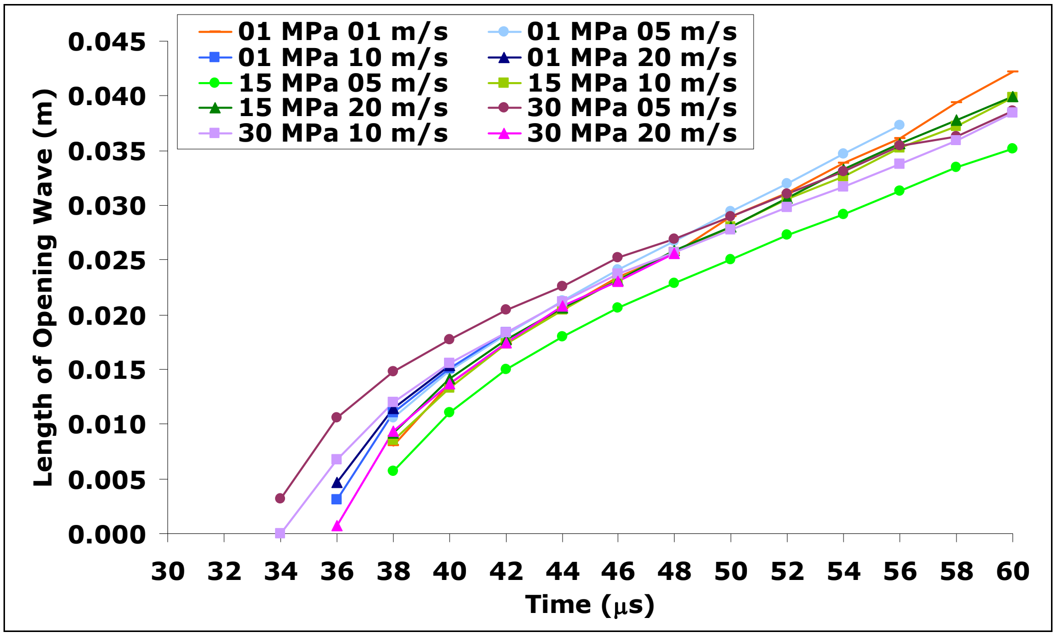

Figure 5.51: Length of Opening Waves vs. Time

The lengths of the opening waves follow a similar trend throughout time for each of the cases represented in Figure 5.51. The lengths of the opening waves are all within ten millimeters of one another for any given time shown above. Also, it should be noted that these opening waves are always growing as time increases. Finally, the actual speeds that these opening waves are moving at can be seen in Figure 5.52 below.

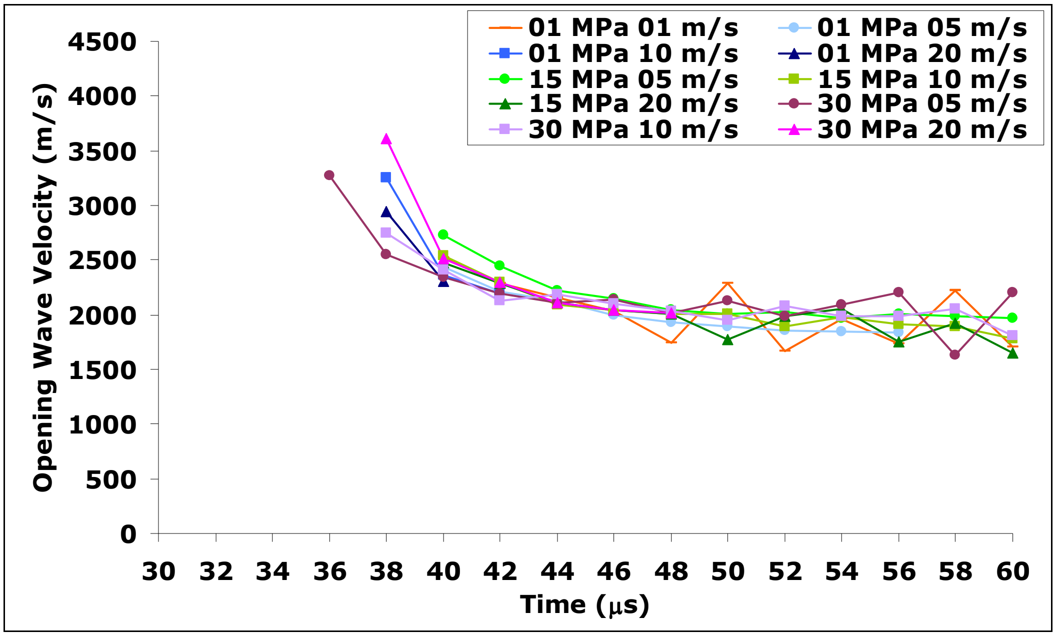

Figure 5.52: Opening Wave Velocities vs. Time

The opening wave velocities are all similar as well. These wave speeds are all around the longitudinal wave speeds for the Homalite material represented in the numerical simulations. Thus, it is interesting to note that regardless of the compressive stress holding the plates together and regardless of the impact velocity used to start sliding between the two plates, there are always opening waves occurring along the interface. Not only are they occurring every time, but they are also all beginning at relatively similar locations and following the same trends as far as opening speed and lengths are concerned.

5.3. Crack Tip Velocity

As discussed previously in Chapter 2, the crack tip velocity associated with frictional sliding has been analyzed. The results of the crack tip velocities found for this research is shown in Figure 5.53:

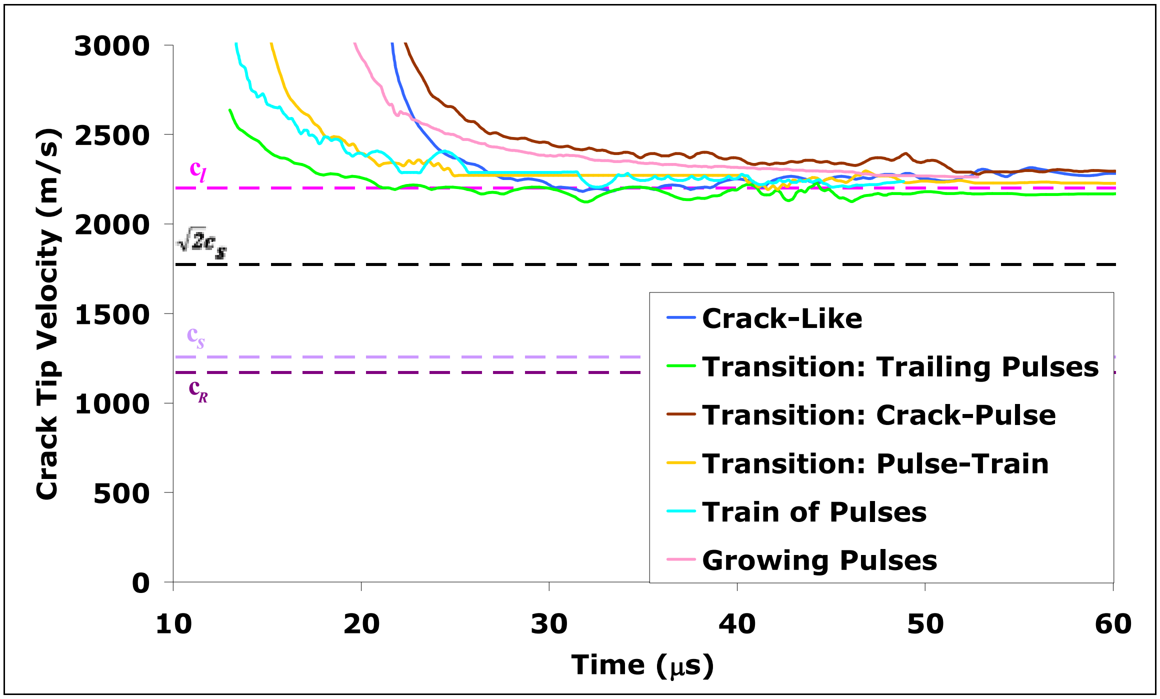

Figure 5.53: Crack Tip Velocity Plot for each Sliding Mode

In Figure 5.53, c_l denotes the longitudinal wave speed, c_s is the shear wave speed, $\sqrt{2}c_s$ denotes the critical crack tip speed, and c_R is the Rayleigh wave speed. From the figure, it can be determined that for each sliding mode, the crack tip velocity is around the longitudinal wave speed for Homalite. However, in some laboratory experiments the crack tip velocity has been observed to be intersonic between the longitudinal wave speed and the shear wave speed. During the numerical simulations performed in this research, there were some isolated cases that showed the crack tip velocities to be intersonic and one case showed a sub-Rayleigh velocity. These isolated cases are all crack-like sliding, but are not necessarily representative of the entire sliding mode as a group. These velocities are plotted in Figure 5.54.

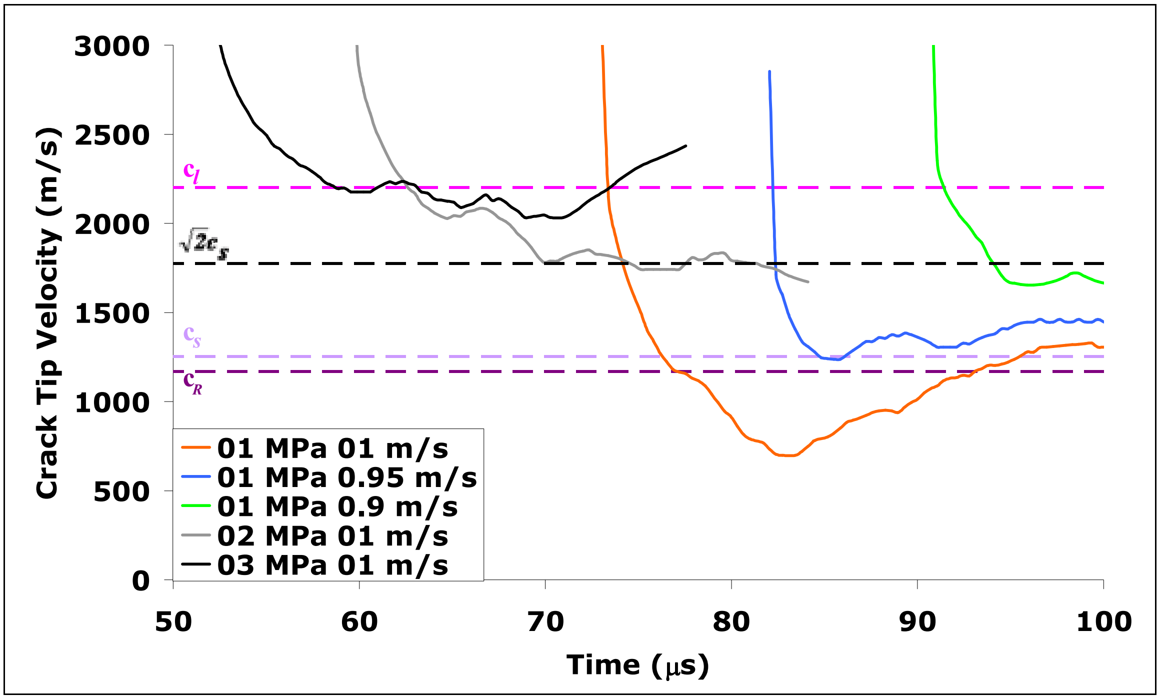

Figure 5.54: Intersonic and Sub-Rayleigh Crack Tip Velocities

There is a sub-Rayleigh crack tip velocity for the crack-like case of 1 MPa and 1 m/s. As the compressive stress increases, the crack tip speed also increases above this Rayleigh wave speed and becomes intersonic. But if the impact velocity is decreased, the sliding not only seems to start later but it also falls between the critical crack tip speed of $\sqrt{2}c_s$ the shear wave speed, c_S.

CHAPTER 6

CONCLUSIONS AND RECOMMENDATIONS

6.1. Summary

The dynamic behavior of frictional sliding between two Homalite plates subject to an impact velocity under compressive loading was studied. Simulations were carried out using finite element analysis with a rate-state friction law implemented in a framework of cohesive element interfacial model. Frictional sliding occurred between two identical elastic plates held together by compressive load and by the application of an impact velocity to the bottom plate.

6.2. Conclusions

Previous to this research three different modes of stick-slip behavior were known to exist—crack-like, slip-pulse (including multiple pulses), and a transitional mode between the crack-like and pulse sliding modes. The results of this current research support the conclusion that in fact six different modes of partial frictional sliding exist. These modes depend on the compressive load and the impact velocity as shown in the frictional sliding blended phase diagram of Figure 5.47. Frictional sliding occurred in an expanding crack-like mode for low compressive stress $\left(\frac{\sigma_0}{E} \leq 0.0015\right)$ and impact velocity $\left(\frac{V_{imp}}{c_s} \leq 0.016\right)$, where σ_0 is the applied compressive load, E is Young's modulus, V_{imp} is the applied impact velocity, and c_s is the material's shear wave speed.

Multiple pulses were found for intermediate to large compressive loading $\left(\frac{\sigma_0}{E} > 0.0015\right)$ for all impact velocities. These pulses are stable compared to growing pulses since they propagate steadily and have not been confirmed experimentally. Although growing pulses are numerically unstable, experiments have shown single growing pulses that are stable. More specifically, a train of pulses frictional sliding mode was observed $\left(0.0025 \le \frac{\sigma_0}{E} \le 0.0035\right)$ whereas higher compressive loads allowed for growing pulses $\left(\frac{\sigma_0}{E} > 0.0035\right)$. In addition to crack-like mode, train of pulses, and growing pulses, intermediate transitional modes were identified. A transitional mode with stick-slip occurring behind the leading wave (trailing pulses transitional mode) was found for low compressive stress $\left(\frac{\sigma_0}{E} \le 0.0015\right)$ and intermediate to high impact velocities $\left(\frac{V_{imp}}{c_s} > 0.016\right)$. Another transitional mode has a leading wave with a pulse that is emerging (crack-pulse transitional mode) that occurs for compressive loading, $0.0015 < \frac{\sigma_0}{E} \le 0.0025$, and low impact velocities $\left(\frac{V_{imp}}{c_s} \le 0.007\right)$. After these two transitional modes had been established, it was found that there was indeed a third transitional mode that combines these two modes and begins to stick-slip more often (pulse-train transitional mode). This pulse-train transitional modes occur for intermediate to high impact velocities $\left(\frac{V_{imp}}{c_s} > 0.007\right)$ and occurs in a compressive loading region, $0.0015 < \frac{\sigma_0}{E} \le 0.0025$.

In addition to slip-pulses mentioned above which are sliding of adjacent points at the interface, opening waves were found. Opening waves are the separation of the adjacent points along the interface which are occurring behind the leading sliding waves. This behavior has been noted in previous research done with the same materials by Coker et al. (2003) and two different materials by Schallamach (1971). A new finding of this research is that this region of separation occurs independently of the sliding mode, impact velocity, and compressive load. This seems to be an artifact of dynamic loading and is always reached when the local compressive stresses become less than the applied compressive load as the impact wave progresses. This remains to be observed in experiments.

The observed sliding modes and the separation opening waves were observed for the sliding of identical materials and did not require a bimaterial interface. It has been shown that these sliding modes have occurred between identical plates and does not require sliding between dissimilar materials.

The crack-tip speed is usually supersonic in previous numerical studies (Coker et al. 2005). In this study, it was concluded that both supersonic crack-tip velocities and intersonic crack-tip velocities were possible at very low compressive loads and impact velocities. Previously, intersonic crack-tip velocities were found in the laboratory but not in numerical experiments.

6.3. Recommendations for Future Work

While the train of pulses sliding mode has been observed numerically, it has not been seen experimentally. This experimentally elusive train of pulses sliding mode could be searched for by finding the compressive load at which these are generated. In the laboratory, once the compressive load is discovered that could allow for multiple pulses, then the train of pulses mode would begin to emerge.

It will be important to look at the effect of the friction law constitutive parameters on these sliding modes. The effect of the impact velocity shape and dimensions of the impact velocity loading and its effect on the interfacial separation will need to be studied more in detail as well. Adding energy calculations into the program would be useful to see the energy dissipation associated with each sliding mode. This would be important not only for industry but is also a critical aspect in earthquake faulting.

REFERENCES

Ben-Zion, Y. and Y. Q. Huang (2002). Dynamic rupture on an interface between a compliant fault zone layer and a stiffer surrounding solid. Journal Of Geophysical Research-Solid Earth 107(B2).

Coker, D. (1997). Size of the fractured zones beneath terrestrial impact craters and its relationship to crater diameter.

Coker, D., G. Lykotrafitis, A. Needleman and A. J. Rosakis (2005). Frictional sliding modes along an interface between identical elastic plates subject to shear impact loading. Journal of the Mechanics and Physics of Solids 53(4): 884-922.

Coker, D., R. W. Neu and T. Nicholas (1996). Analysis of the thermoviscoplastic behavior of [0/90] SCS-6/TIMETAL®21S composites. Thermo-Mechanical Fatigue Behavior of Materials: Second Symposium AmericanSociety for Testing and Materials STP 1263. Philadelphia.

Coker, D. and A. J. Rosakis (2001). Experimental observations of intersonic crack growth in asymmetrically loaded unidirectional composite plates. Philosophical Magazine a-Physics of Condensed Matter Structure Defects and Mechanical Properties 81(3): 571-595.

Coker, D., A. J. Rosakis and Y. Y. Huang (1999). Subsonic and intersonic dynamic crack growth in unidirectional composites. Proceedings of the 12th International Conference on Composite Materials, Paris, France.

Coker, D., A. J. Rosakis and A. Needleman (2003). Dynamic crack growth along a polymer composite-Homalite interface. Journal Of The Mechanics And Physics Of Solids 51(3): 425.

Daphalapurkar, N. P., H. Lu, D. Coker and R. Komanduri (2007). Simulation of dynamic crack growth using the generalized interpolation material point (GIMP) method. International Journal of Fracture 143(1): 79-102.

Dieterich, J. H. (1979). Modeling of rock friction.1. Experimental results and constitutive equations. Journal of Geophysical Research 84(NB5): 2161-2168.

Dieterich, J. H. (1979). Modeling of rock friction.2. Simulation of pre-seismic slip. Journal of Geophysical Research 84(NB5): 2169-2175.

Dieterich, J. H. and B. Kilgore (1996). Implications of fault constitutive properties for earthquake prediction. Proceedings Of The National Academy Of Sciences Of The United States Of America 93(9): 3787.

Dieterich, J. H. and B. D. Kilgore (1994). Direct observation of frictional contacts – new insights for state-dependent properties. Pure and Applied Geophysics 143(1-3): 283-302.

Dieterich, J. H. and B. D. Kilgore (1996). Imaging surface contacts: Power law contact distributions and contact stresses in quartz, calcite, glass and acrylic plastic. Tectonophysics 256(1-4): 219-239.

Dieterich, J. H. and M. F. Linker (1992). Fault stability under conditions of variable normal stress. Geophysical Research Letters 19(16): 1691-1694.

Lapusta, N. and J. R. Rice (2003). Nucleation and early seismic propagation of small and large events in a crustal earthquake model. Journal Of Geophysical Research-Solid Earth 108(B4).

Lapusta, N., J. R. Rice, Y. Ben-Zion and G. T. Zheng (2000). Elastodynamic analysis for slow tectonic loading with spontaneous rupture episodes on faults with rate- and state-dependent friction. Journal Of Geophysical Research-Solid Earth 105(B10): 23765.

Lykotrafitis, G. and A. J. Rosakis (2006). Dynamic sliding of frictionally held bimaterial interfaces subjected to impact shear loading. Proceedings of the Royal Society a-Mathematical Physical and Engineering Sciences 462(2074): 2997-3026.

Lykotrafitis, G., A. J. Rosakis and G. Ravichandran (2006). Self-healing pulse-like shear ruptures in the laboratory. Science 313(5794): 1765-1768.

Ma, K., et. al (2006). Slip zone and energetics of a large earthquake from the Taiwan Chelungpu-fault Drilling Project. Nature 444: 473-476.

Marone, C. (1998). Laboratory-derived friction laws and their application to seismic faulting. Annual Review Of Earth And Planetary Sciences 26: 643.

Marone, C. and E. Richardson (2006). Do earthquakes rupture piece by piece or all together? Science 313(5794): 1748-1749.

Povirk, G. L. and A. Needleman (1993). Finite-element simulations of fiber pull-out. Journal of Engineering Materials and Technology-Transactions of the ASME 115(3): 286-291.

Povirk, G. L., A. Needleman and S. R. Nutt (1991). An analysis of the effect of residual-stresses on deformation and damage mechanisms in Al-SiC composites. Materials Science and Engineering a-Structural Materials Properties Microstructure and Processing 132: 31-38.

Prakash, V. (1998). Frictional response of sliding interfaces subjected to time varying normal pressures. Journal of Tribology-Transactions of the ASME 120(1): 97-102.

Prakash, V. and R. J. Clifton (1993). Pressure-shear plate impact measurement of dynamic friction for high speed machining applications. Proceedings of the Seventh International Congress on Experimental Mechanics. Society of Experimental Mechanics: 556–564.

Ranjith, K. and J. R. Rice (1999). Stability of quasi-static slip in a single degree of freedom elastic system with rate and state dependent friction. Journal Of The Mechanics And Physics Of Solids 47(6): 1207.

Ranjith, K. and J. R. Rice (2001). Slip dynamics at an interface between dissimilar materials. Journal Of The Mechanics And Physics Of Solids 49(2): 341.

Rice, J. R., N. Lapusta and K. Ranjith (2001). Rate and state dependent friction and the stability of sliding between elastically deformable solids. Journal Of The Mechanics And Physics Of Solids 49(9): 1865.

Rice, J. R. and A. L. Ruina (1983). Stability Of Steady Frictional Slipping. Journal Of Applied Mechanics-Transactions Of The Asme 50(2): 343.

Ruina, A. (1983). Slip Instability And State Variable Friction Laws. Journal Of Geophysical Research 88(NB12): 359.

Schallamach, A. (1971). How does rubber slide. Wear 17(4): 301-&.

Scholz, C. H. (1998). Earthquakes and friction laws. Nature 391(6662): 37.

Tinti, E., A. Bizzarri and M. Cocco (2005). Modeling the dynamic rupture propagation on heterogeneous faults with rate- and state-dependent friction. Annals of Geophysics 48(2): 327-345.

Tinti, E., P. Spudich and M. Cocco (2005). Earthquake fracture energy inferred from kinematic rupture models on extended faults. J. Gephys. Res. 110: 1-25.

Tsai, K. H. and K. S. Kim (1996). The micromechanics of fiber pull-out. Journal Of The Mechanics And Physics Of Solids 44(7): 1147.

APPENDIX

A.1. More Examples of Crack-Like Mode

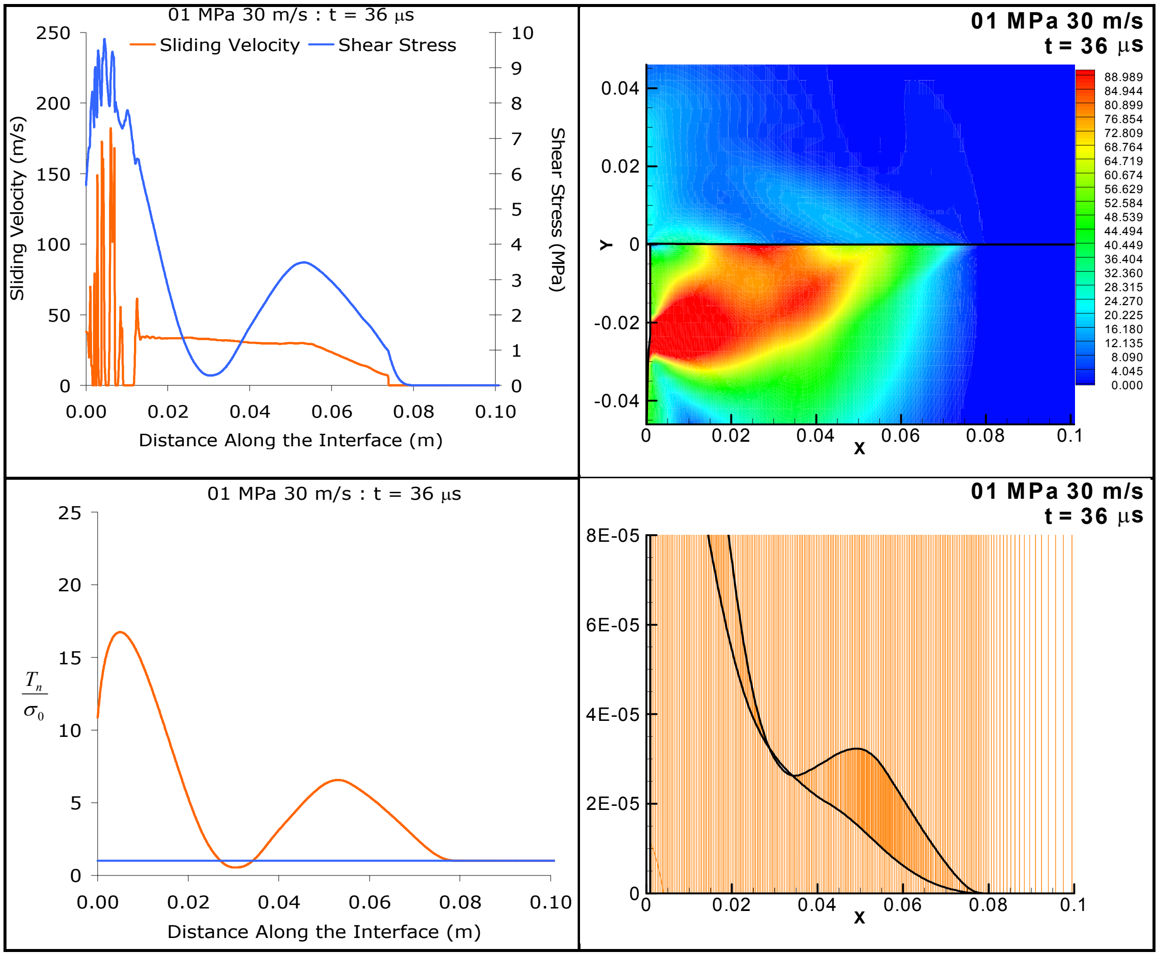

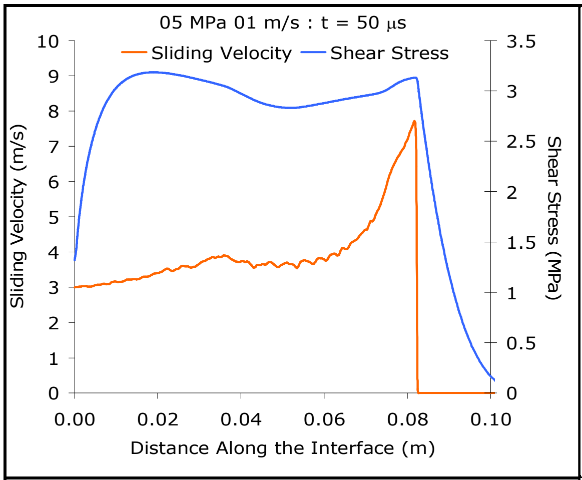
05 MPa 01 m/s : t = 50 μs
Sliding Velocity
Shear Stress
Sliding Velocity (m/s)
Shear Stress (MPa)
Distance Along the Interface (m)
0
1
2
3
4
5
6
7
8
9
10
0
0.5
1
1.5
2
2.5
3
3.5
0.00
0.02
0.04
0.06
0.08
0.10

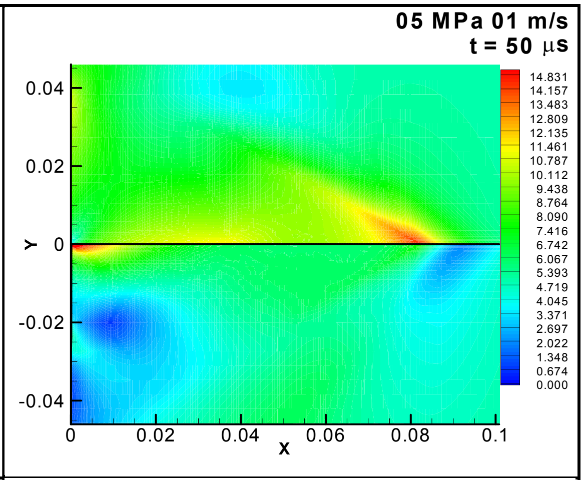
05 MPa 01 m/s
t = 50 μs
Y
X
0.04
0.02
0
-0.02
-0.04
0
0.02
0.04
0.06
0.08
0.1
14.831
14.157
13.483
12.809
12.135
11.461
10.787
10.112
9.438
8.764
8.090
7.416
6.742
6.067
5.393
4.719
4.045
3.371
2.697
2.022
1.348
0.674
0.000

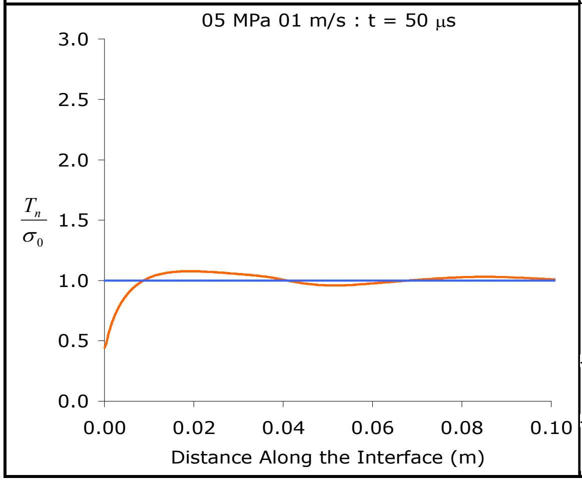
05 MPa 01 m/s : t = 50 μs
$\frac{T_n}{\sigma_0}$
Distance Along the Interface (m)
3.0
2.5
2.0
1.5
1.0
0.5
0.0
0.00
0.02
0.04
0.06
0.08
0.10

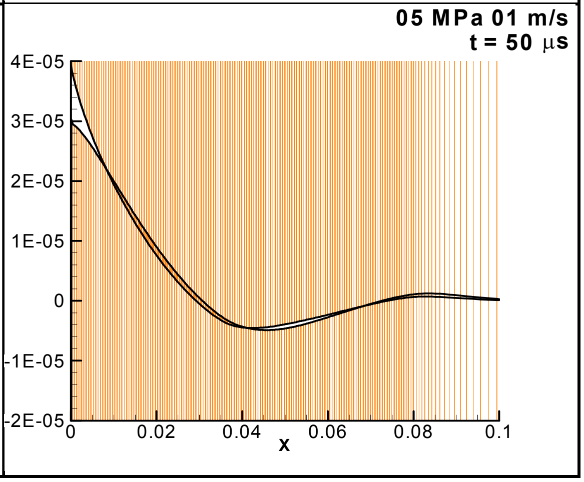
05 MPa 01 m/s
t = 50 μs
X
4E-05
3E-05
2E-05
1E-05
0
-1E-05
-2E-05
0
0.02
0.04
0.06
0.08
0.1

A.2. More Examples of Trailing Pulses Transitional Mode

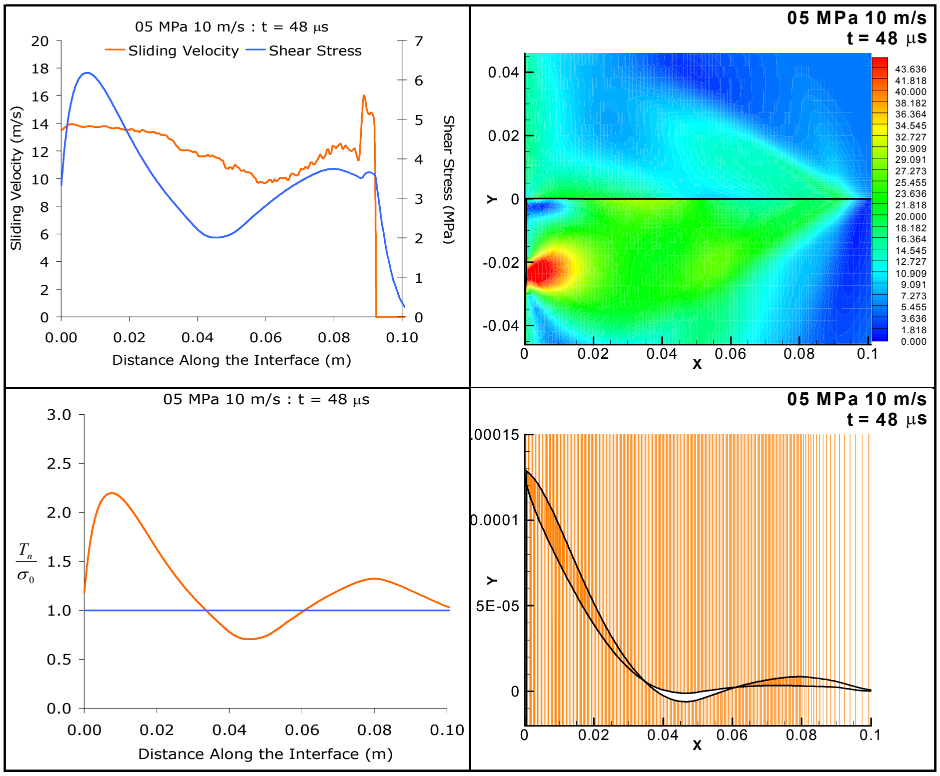

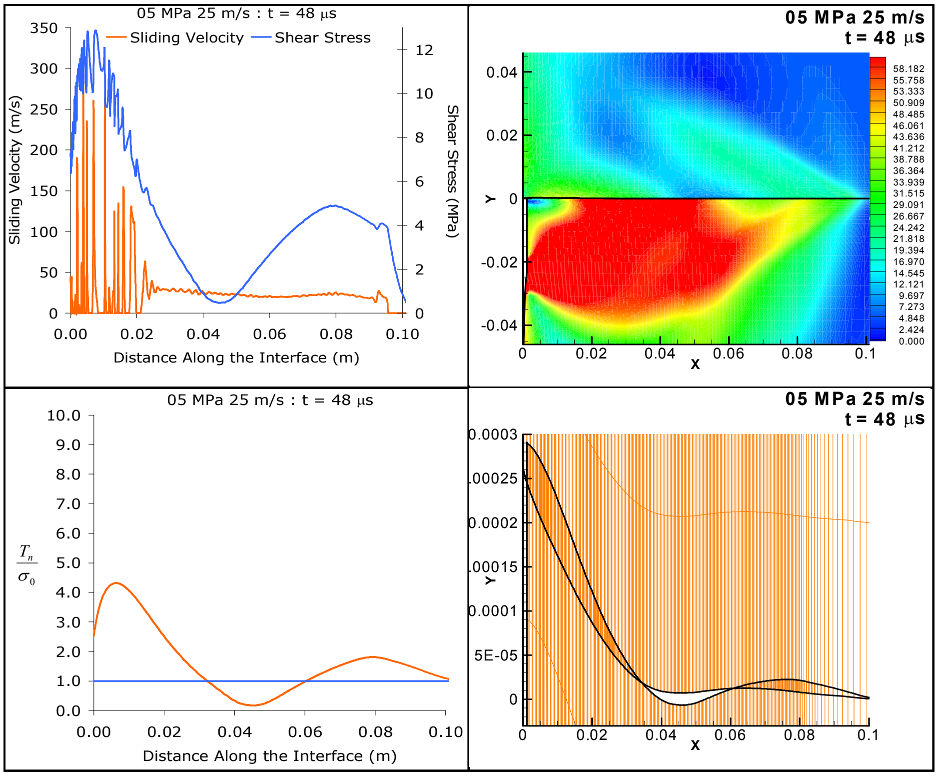

A.3. More Examples of Crack-Pulse Transitional Mode

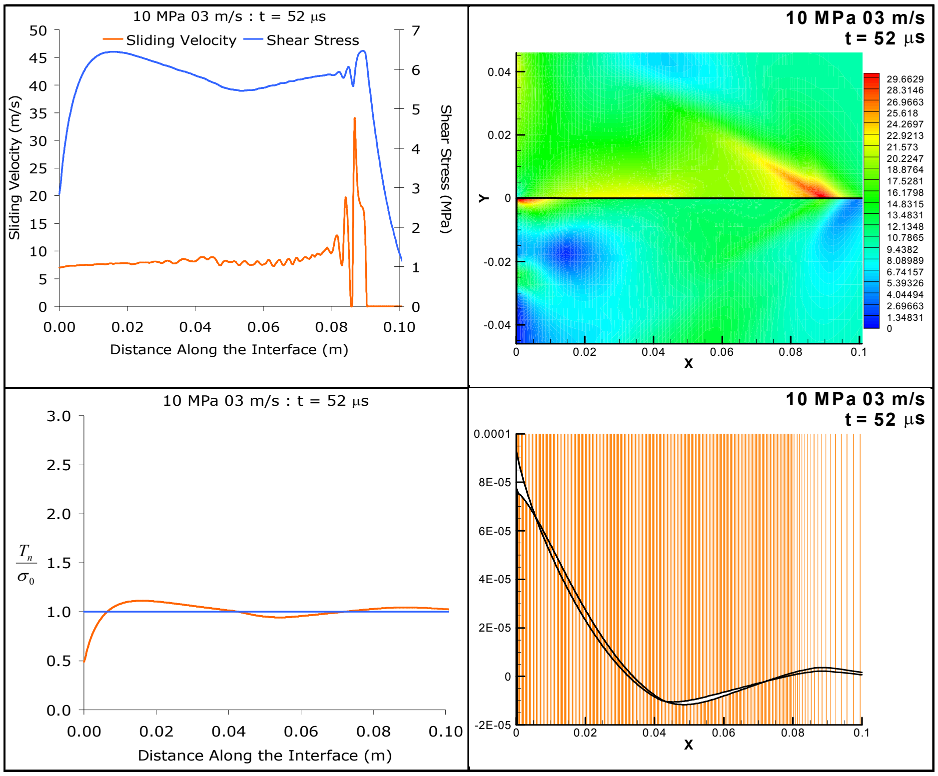

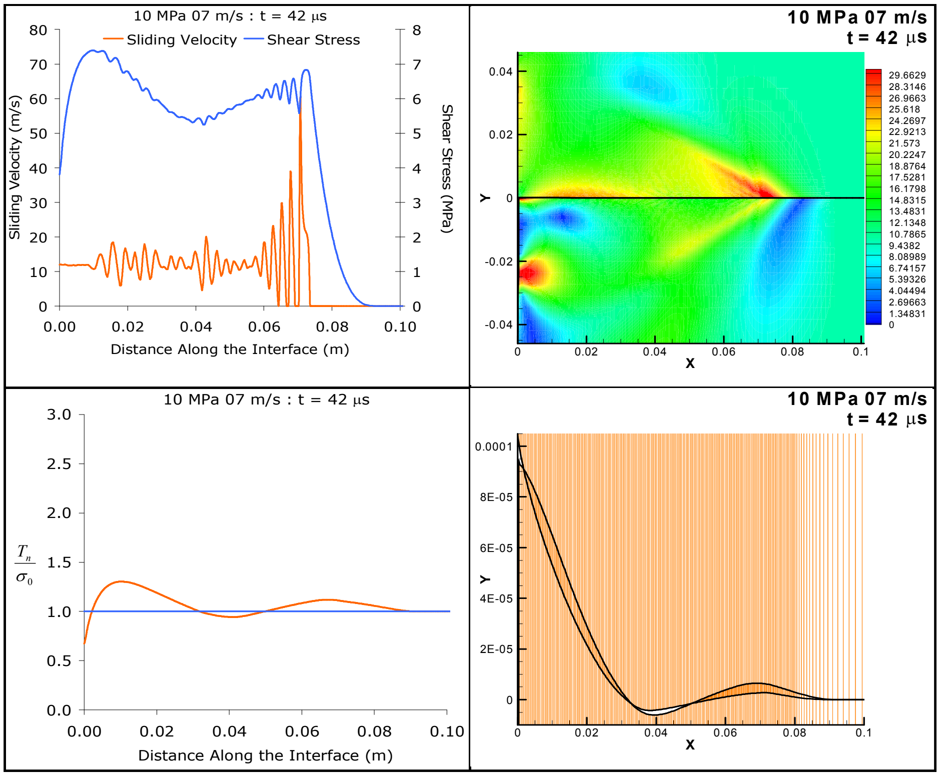

A.4. More Examples of Pulse-Train Transitional Mode

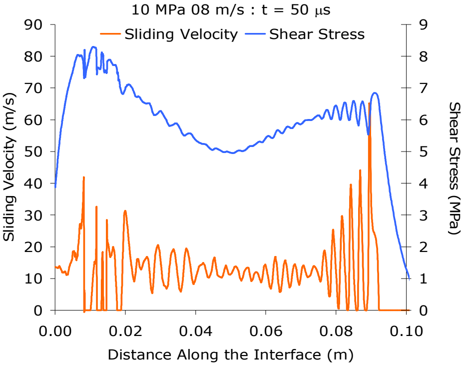

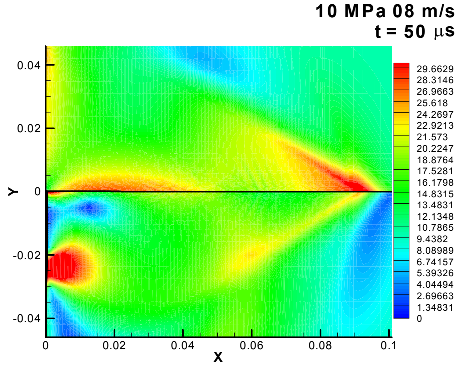

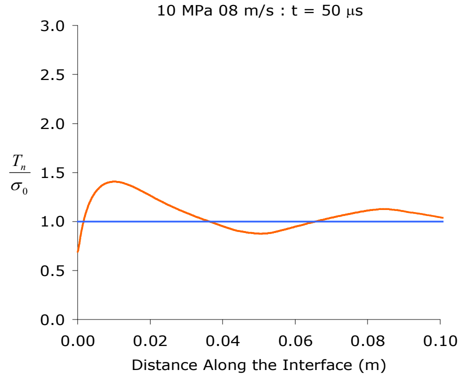

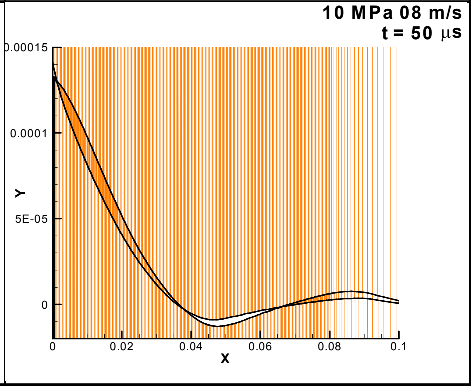

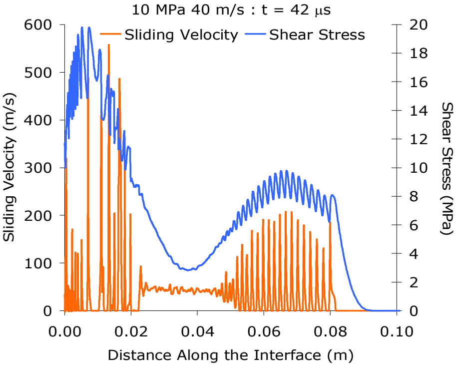

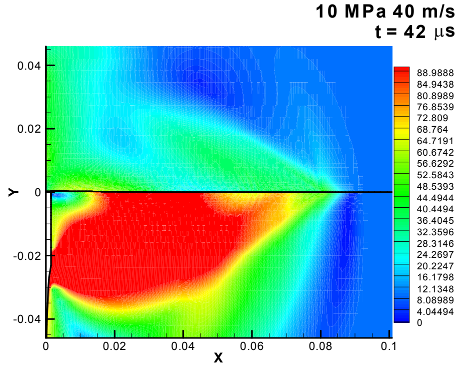

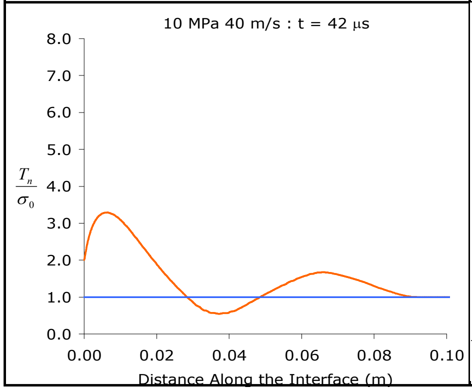

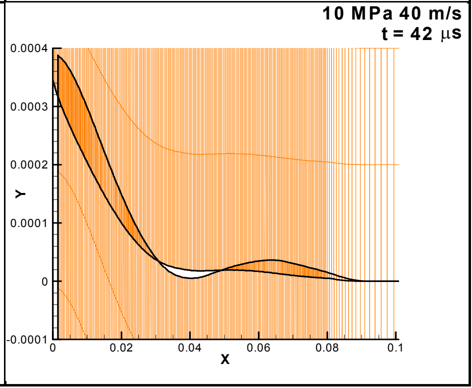

A.5. More Examples of Train of Pulses Mode

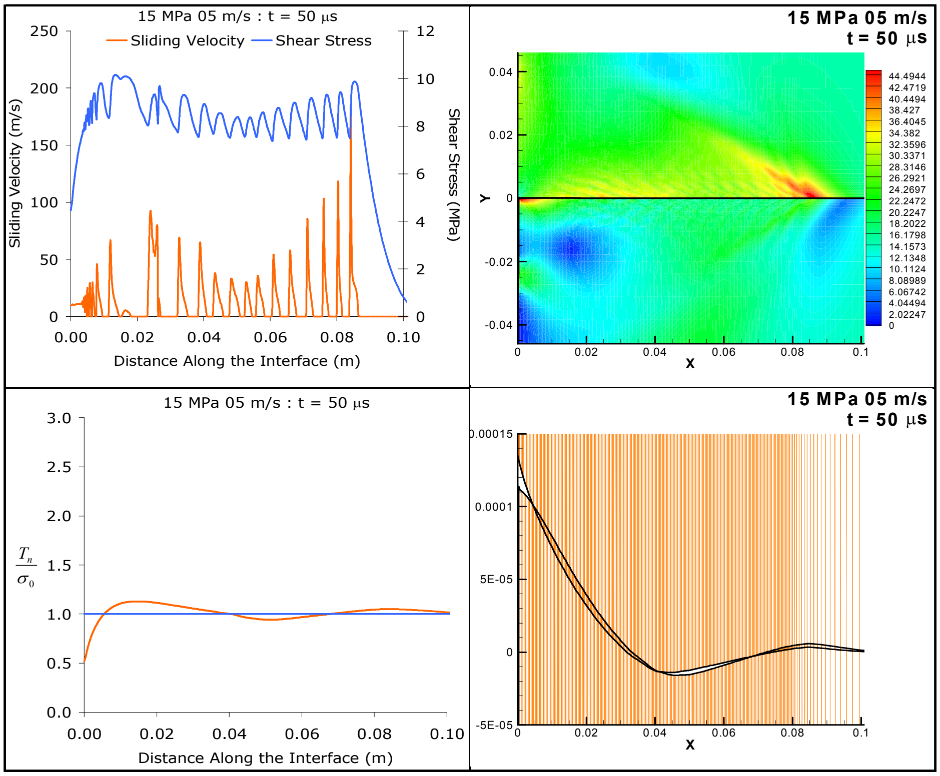

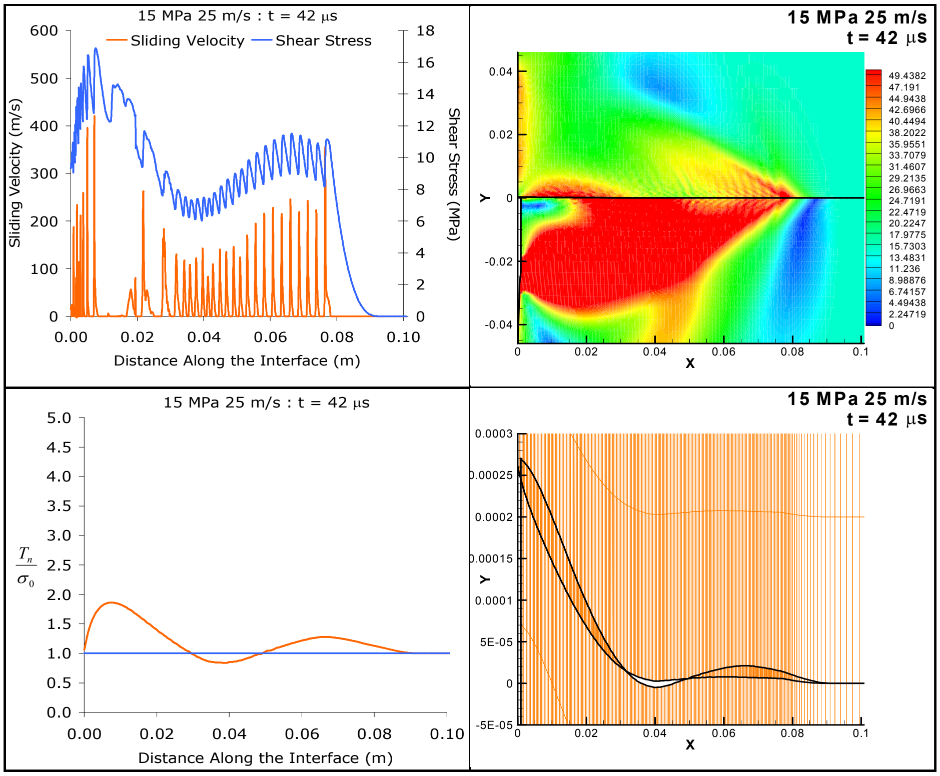

A.6. More Examples of Growing Pulses Mode

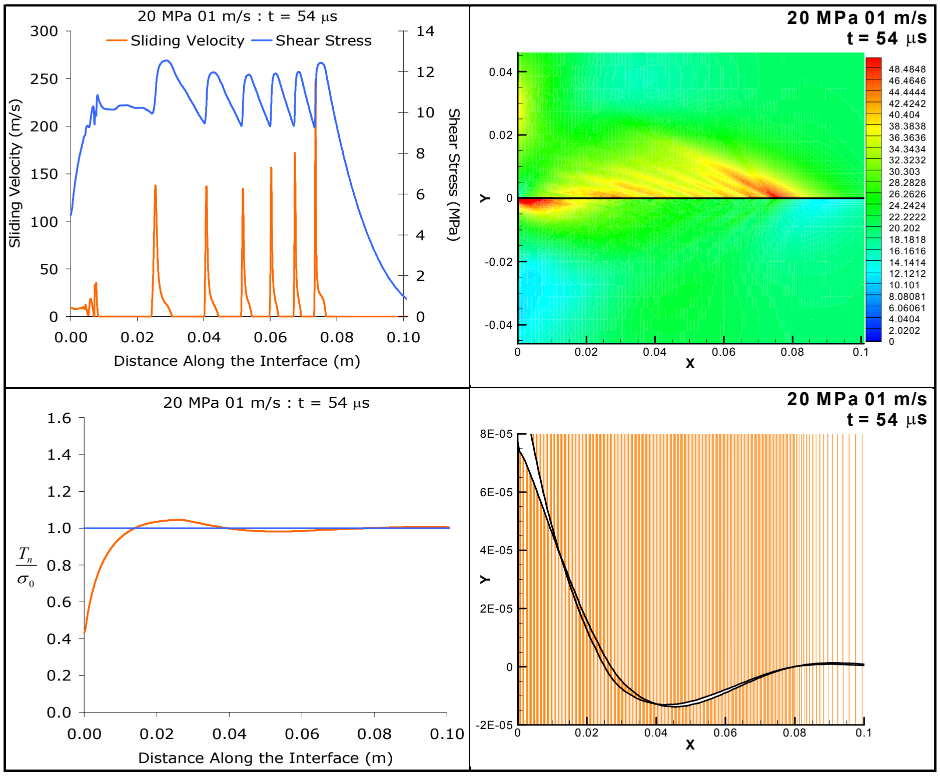

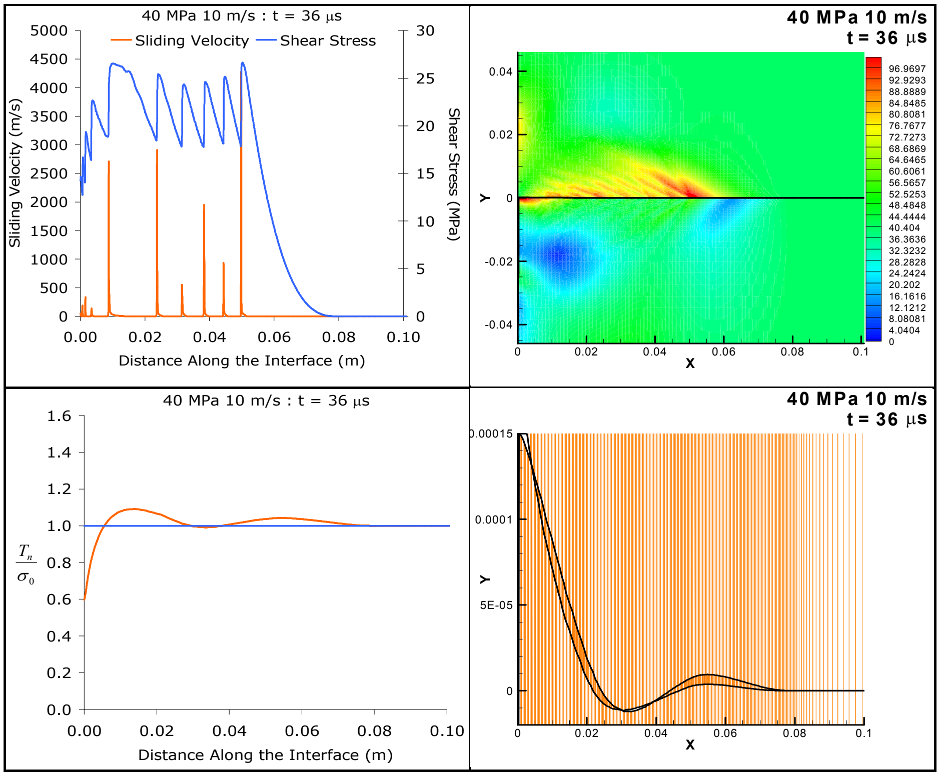

VITA

Erika Ennis Nichols

Candidate for the Degree of

Master of Science

Thesis: DYNAMIC FRICTIONAL SLIDING ALONG AN INTERFACE BETWEEN TWO HOMOGENEOUS BLOCKS

Major Field: Mechanical Engineering

Biographical:

Personal Data: Born in Edmond, Oklahoma on June 30, 1983, the daughter of J. Steven and Kathryn D. Ennis. Married Rodney E. Nichols on July 23, 2005.

Education: Graduated from Edmond North High School, Edmond, Oklahoma, in May 2001; received Bachelor of Science degree in Mechanical Engineering from Oklahoma State University, Stillwater, Oklahoma, in May 2006; completed the requirements for the Master of Science in Mechanical Engineering at Oklahoma State University, Stillwater, Oklahoma in May 2008.

Experience: Mathematics Tutor, Mathematics Learning Resource Center, 2004; Head Coordinator, Mathematics Learning Resource Center, 2005-2006; Research Assistant, OSU Department of Mechanical Engineering and Aerospace Engineering, 2005-2008; Teaching Assistant, OSU Department of Mechanical Engineering and Aerospace Engineering, 2006-2007; Mathematics Tutor, OSU Academic Services for Student-Athletes, 2007-2008; Mathematics Instructor, Northern Oklahoma College Department of Mathematics, 2008.

Professional Memberships: American Institute of Aeronautics and Astronautics, Pi Tau Sigma, Tau Beta Pi, Pi Mu Epsilon, Phi Kappa Phi.

Name: Erika Ennis Nichols Date of Degree: May, 2008

Institution: Oklahoma State University Location: Stillwater, Oklahoma

Title of Study: DYNAMIC FRICTIONAL SLIDING ALONG AN INTERFACE BETWEEN TWO HOMOGENEOUS BLOCKS

Pages in Study: 85 Candidate for the Degree of Master of Science

Major Field: Mechanical Engineering

The purpose of this research is to analyze the dynamic frictional sliding that is occurring between two Homalite blocks. The blocks are held together by a compressive load and the sliding is initiated by an impact velocity that is applied to the bottom block. Previously, the main types of sliding observed were crack-like sliding and stick-slip (pulses) sliding. Six different sliding modes were observed: crack-like, transitional trailing pulses, transitional crack-pulse, transitional pulse-train, train of pulses, and growing pulses. Each mode has distinct sliding characteristics that are dependent on the compressive load and impact velocity. Along with this interfacial sliding, there were opening waves observed due to a region of separation at adjacent points along the interface. These regions of separation occur independently of the sliding modes discussed. In addition, crack tip velocities of the leading sliding waves were found to not only be supersonic but also intersonic crack speeds were observed.

ADVISER’S APPROVAL: Dr. D. Coker